Reducing Recombination in Halide Perovskite Solar Cells via Interface Engineering

Yangwei Shi

A dissertation
submitted in partial fulfillment of the
requirements for the degree of

Doctor of Philosophy

University of Washington

2024

Reading Committee:

David S. Ginger, Chair

Lih Y. Lin

Cody W. Schlenker

J. Devin MacKenzie

Program Authorized to Offer Degree:
Molecular Engineering & Sciences Institute

University of Washington

Abstract

Reducing Recombination in Halide Perovskite Solar Cells via Interface Engineering

Yangwei Shi

Chair of the Supervisory Committee:
David S. Ginger
Department of Chemistry

Halide perovskite solar cells have attracted tremendous attention and have been extensively studied over the last decade. Though the power conversion efficiency of single junction of perovskite solar cells has reached 26.1%, it still lags behind the theoretical limit, which is largely due to the open-circuit voltage deficit that results from nonradiative recombination in the bulk of perovskite films and also at the interfaces between perovskite and transport layers. When transport layers contact with perovskite, it generally induces new nonradiative loss pathways at the interface, resulting in a decrease in device performance. In this dissertation, we engineer the interface of perovskite solar cells to minimize the nonradiative recombination loss via interlayer engineering, electronic decoupling, and surface field, to further enhance perovskite solar cells performance.

First, we investigate a photo-crosslinkable naphthalene diimide polymer as the electron-transport layer for *n*-*i*-*p* perovskite solar cells. Inorganic metal oxides such as titanium dioxide (TiO_2) and tin oxide (SnO_2) have been widely used as the electron-transport layer in *n*-*i*-*p* perovskite solar cell. Nevertheless, these inorganic materials require high annealing temperature and may incur instability of the perovskite layer due to photoactivity. Organic polymers as electron-transport layers offer a new pathway for perovskite solar cells because of their low processing cost, good chemical and thermal stability, and ability to tune the energy levels. Thus, we study the thermal stability, conductivity with and without doping and

solvent resistance of naphthalene diimide polymer. Furthermore, we incorporate the photo-crosslinkable naphthalene diimide polymer into perovskite solar cell as electron transport layer, studying the impact of this photo-crosslinkable polymer on device performance. We further explore the influence of this polymer on the structure and optoelectronic properties of perovskite film.

Next, we focus on studying the surface/interface passivation of perovskite layer in *p-i-n* perovskite solar cells. Halide perovskite is polycrystalline material which has many grain boundaries. These grain boundaries as well as perovskite top surface are most defective due to abruptly broken atomic lattice and unsatisfied dangling bonds at a surface/interface, which results in enhanced electron-hole nonradiative recombination. We demonstrate reduced surface recombination velocity (SRV) and enhanced power-conversion efficiency (PCE) in mixed-cation mixed-halide perovskite solar cells by using a surface passivator called (3-aminopropyl)trimethoxysilane (APTMS). We show the APTMS serves to passivate defects at the perovskite surface, while also decoupling the perovskite from detrimental interactions at the C_{60} interface.

Lastly, we design two ionic pair salts as interlayers and apply them in between wide-bandgap perovskite and C_{60} layer. Wide-bandgap perovskite can be integrated in the perovskite/silicon tandems to overcome the theoretical limit of single junction solar cells. However, the substantial nonradiative interfacial recombination at the perovskite/C_{60} interface, limiting open-circuit voltage V_{OC} and thus PCE. We show that benzylammonium tosylate (BzAOTs) and benzylammonium triflate (BzAOTf) interlayers reduced interfacial nonradiative recombination at the perovskite/C_{60} interface and enhanced V_{OC} in mixed-halide mixed-cation wide-bandgap (~1.7 eV) perovskite solar cells. We unveil that The BzAOTs interlayer improves the device performance through reducing the interfacial nonradiative recombination via surface field while BzAOTf decouples the perovskite film from the detrimental interactions at C_{60} interface.

Our research highlights that engineering interface in perovskite solar cell is an effective approach to reduce recombination in perovskite solar cell, which provides valuable insights for device optimization.

TABLE OF CONTENTS

Page

LIST OF FIGURES

ACKNOWLEDGMENTS

First of all, I am extremely grateful to my advisor Dr. David S. Ginger for his unwavering mentorship, guidance and support throughout my Ph.D. journey. David holds high standards for Ginger group, which also motivates me to improve myself. I really appreciate his dedication, encouragement, and countless hours that were invested in nurturing my academic development and personal growth. David has provided invaluable assistance with my career planning and facilitated introductions to his industry connections. I am truly privileged to have had the opportunity to learn from and work with such a distinguished mentor.

I would like to thank my dissertation committee, Prof. Lih Y. Lin, Prof. Shijing Sun, Prof. Cody W. Schlenker and Prof. J. Devin MacKenzie for their constructive feedback and critical evaluations of my research.

I extend my sincere appreciation to Dr. Jian Wang and Dr. Fangyuan Jiang for their generous guidance and mentorship. When I first joined Ginger lab, the first person I shadowed and worked with was Dr. Wang who is now a director at Ubiquitous Energy. I had no experience with synthesis or characterizations of halide perovskite films and solar cells. Dr. Wang is patient to explain the principles of halide perovskite materials to me, and show me the experimental skills. Dr. Jiang has also been helping me with my research. Whenever I have questions in research, she is always there to help me.

I would extend my gratitude to all my collaborators, especially Dr. Declan P. McCarthy, Dr. Stephen Barlow, and Prof. Seth R. Marder from Universtity of Colorado Boulder; Dr. Esteban Rojas-Gatjens and Prof. Carlos Silva-Acuña from Georgia Institute of Technology; Dr. Suer Zhou, Dr. Joel Smith and Prof. Henry Snaith from University of Oxford; Dr. Cheng Chang, Prof. Lih Y. Lin, Dr. Yunping Huang, Prof. Christine Luscombe from University of Washington. Thank all of them for the fruitful discussions and collaborations throughout these years.

I also would like to thank former and current group members in Ginger lab who I have overlap with, for creating such a collaborative and inclusive research environment, including Raj, Jian, Sarthak, Justin, Maddie, Fangyuan, kevin, Muammer, Shaun, Jessica, Hannah, James, Sungjoo, Margherita, Robert, Julisa, Aaron, Emerson, Jiajie, Ramsess, Khoa, Zixu, Yujing and Zhaoqing (undergraduate). Especially, Raj a great research scientist in our group and he has been helping me a lot with AFM related measurements.

I am truly grateful to Fangyuan, Jian, Xudong, Emerson, Junxi, Kevin, Muammer, Farhad, Margherita, Hannah, Jiajie, Gillian, Julisa, Zixu, and Khoa who are not only great lab mates but also wonderful friends after work. I also would like to extend gratitude to my dear friends Xiangyu Gao, Xiao Lin, Xiaofeng Xiang, Ricardo (Rick) Rivera, Jiawei He, Ayumi Pottenger and Brian Sun who made this journey full of joy. I am deeply thankful to Villette and Steve who are my hosts in the U.S. They invite me to their home and celebrate festivals, which provides me with an immersive cultural experience to learn about American customs, traditions and authentic cuisine.

Last but not least, I cannot use words to express my gratitude to my parents for their sacrifice, my sisters and grandparents who always support me and respect my decisions. Without them, this accomplishment would not have been possible.

DEDICATION

to my parents, Zhenmei Zhou and Guangqiang Shi

Chapter 1

INTRODUCTION

The emission of greenhouses gases (GHG) generated by burning fossil fuels results in climate change such as global warming, seal level rising and so forth, which has posed a threat to the environment and human health [1, 2]. To mitigate the detrimental influence of climate change, we need to shift towards a clean-energy-based society instead of heavily relying on fossil fuels. The sun provides inexhaustible renewable solar energy for the Earth. Technologies such as photovoltaic (or solar cell) have been developed to generate electricity through harvesting solar energy [3, 4]. Silicon solar cells have been dominating photovoltaic technology that accounts for over 90% of the deployed photovoltaic technologies [5]. However, halide perovskite solar cell has been one of the emerging photovoltaic technologies that exhibits a great potential for commercialization [6]. The power-conversion efficiency of single-junction perovskite solar cells has surged to 26% over a decade, as shown in Figure 1.1 red line with yellow circles [7].

Metal halide perovskites are crystalline materials with a chemical formula of ABX_3 stoichiometry, where A is an organic monovalent cation (FA^+ = formamidinium, MA^+ = methylammonium) or inorganic alkali metal monovalent cation (Cs^+), B is a divalent metal cation (Pb^{2+}, Sn^{2+}, or Ge^{2+}), and X is a halide anion (I^-, Br^-, or Cl^-). The B site cation and X site anion form a corner-shared octahedron structure that determine the optoelectronic properties of halide perovskite [6, 8, 9]. A schematic of the perovskite crystal structure is shown in Figure 1. Metal halide perovskites have gained tremendous attention and extensive research because of its excellent optoelectronic properties for photovoltaic such high absorption coefficient [10], long carrier lifetime and diffusion length [11, 12, 13]. Moreover, the bandgaps of perovskite can be easily tuned by changing the composition of the precursor solutions [14, 15, 16, 17, 18]. More importantly, halide perovskites prepared with earth-abundant elements, are solution-processable and low-cost, which can significantly

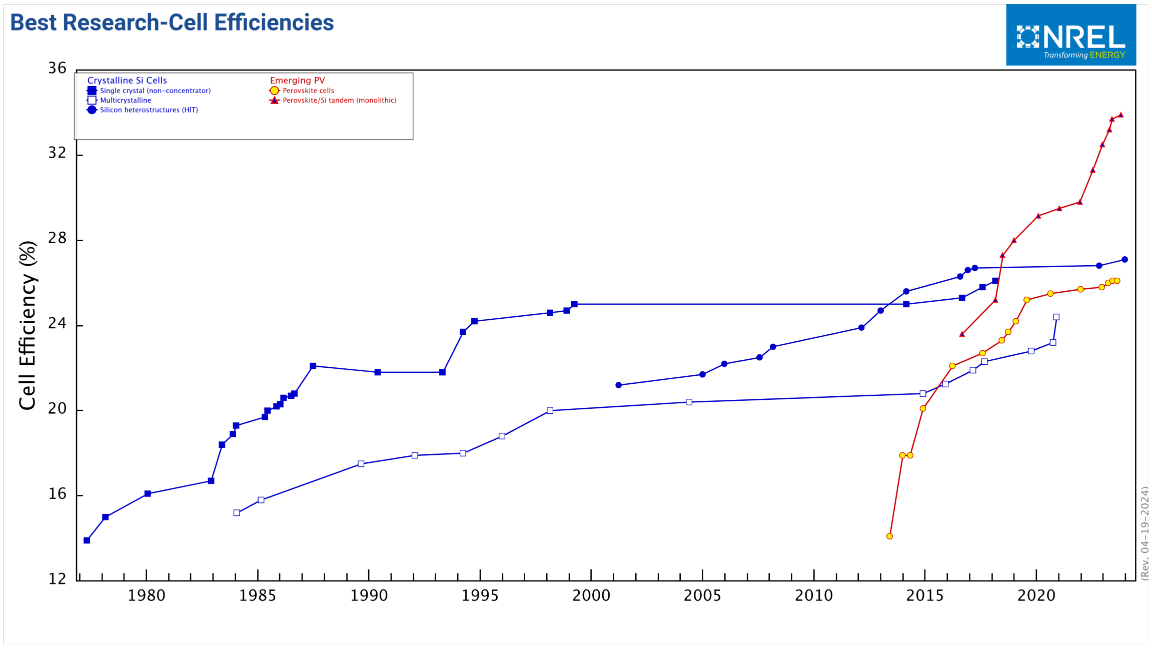

Figure 1.1: Best research-cell efficiency over time (accessed April 19, 2024)

reduce the manufacturing cost [19].

Halide perovskite is a direct bandgap semiconductor and is polycrystalline semiconductor materials, which means that perovskite films have lots of physical grain boundaries. These grain boundaries and top surface of perovskite are most defective due to abrupt termination of lattice and dangling bonds, which induces additional electronic energy level within the bandgaps and results in the nonradiative recombination. These nonradiative recombination will lead to the loss in the open-circuit voltage and thus the power conversion efficiency. In perovskite solar cells, the perovskite layer is sandwiched between electron transport layer and hole transport layer. When perovskite film is in contact with transport layer, it generally induces nonradiative pathways. To approach the theoretical limit of power-conversion efficiency, it requires eliminating all nonradiative channels [20].

This dissertation aims to address nonradiative recombination at the interface of perovskite solar cells that limits the device performance.

In Chapter 2, we explore the utilization of photo-crosslinkable naphthalene diimide poly-

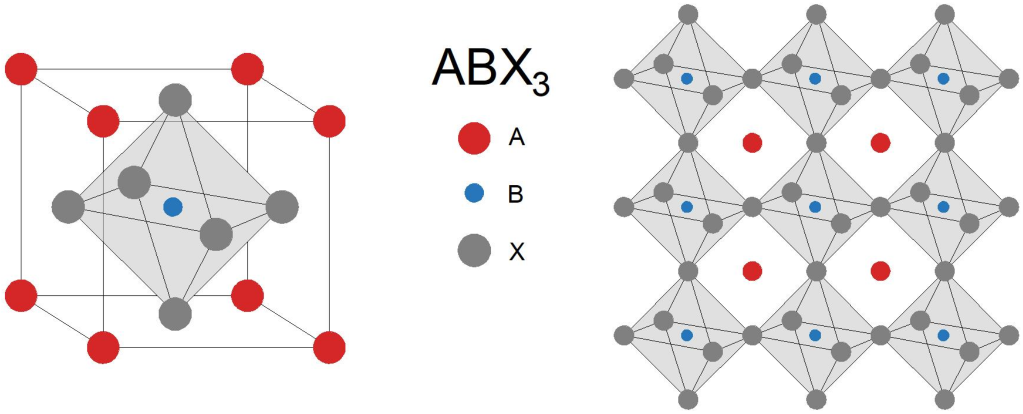

Figure 1.2: Schematic of perovskite crystal structure

mer as the electron transport layer in n-i-p perovskite solar cells. First, we investigate the properties of the polymers, followed by incorporating the polymer into the perovskite solar cell. Through material and device characteristics, we unveil that the photo-crosslinkable naphthalene diimide polymer lowers the work function of indium tin oxide (ITO), reduces nonradiative recombination at the bottom interface, and results in higher shunt resistance compared to its non-crosslinking counterpart.

In Chapter 3, we investigate (3-aminopropyl)trimethoxysilane (APTMS) as the surface passivator in a p-i-n perovskite solar cells. We show the APTMS serves to passivate defects at the perovskite surface, while also decoupling the perovskite from detrimental interactions at the C_{60} interface. Subsequently, we elucidate that APTMS polymerizes heterogeneously at the perovskite surface but still ensures efficient extraction of carriers with scanning probe microscopies.

Chapter 4 is dedicated to mitigating the nonradiative interfacial recombination in wide-bandgap mixed-cation mixed-halide perovskite (~1.7 eV) for integration in perovskite/silicon tandems. We study two ionic pair salts and use them as interlayers at perovskite/C_{60} interface. We study the relationship between device performance, structural properties, surface/interface energy, and charge-carrier recombination at the interface with and without the sulfonate salts to elucidate their effects.

Overall, this dissertation showcases that interface engineering is effective in reducing recombination at the interfaces of perovskite solar cells. The approaches used in this dissertation provide valuable insights into the design of interlayers for reducing recombination at the interfaces and further enhance the device performance of perovskite solar cells.

Chapter 2

PHOTO-CROSSLINKABLE NAPHTHALENE DIIMIDE POLYMER FOR SOLUTION PROCESSED N-I-P PEROVSKITE SOLAR CELLS

Adapted with permission from Yangwei Shi, Declan P. McCarthy, Dominique Lungwitz, Fangyuan Jiang, Margherita Taddei, Hannah Contreras, Yujing Lin, Aiswarya Abhisek Mohapatra, Kan Tang, Yadong Zhang, Stephen Barlow, Antoine Kahn, Seth R. Marder, and David S. Ginger. "Photo-Crosslinkable Naphthalene Diimide Polymer for Solution Processed n-i-p Perovskite Solar cells" Chemistry of Materials 2024 36 (2) 795–802 DOI: 10.1021/acs.chemmater.3c02295 Copyright 2023 American Chemical Society.

2.1 Overview

We copolymerize a norbornene monomer bearing a pendant naphthalene diimide with a norbornene bearing a cinnamate pendant moiety to synthesize a crosslinkable electron-transporting polymer and study its use in solution-processed *n–i–p* perovskite solar cells. The crosslinked material exhibits over 90% transparency in the visible region and higher thermal stability (>300 °C) and lower surface energy than the corresponding homopolymer of the naphthalene diimide functionalized norbornene. Coating an ITO surface with the photo-crosslinked copolymer yields a slightly lower work function than homopolymer-coated ITO. We show that the morphologies of the perovskite films deposited on both polymers are similar (around 300 nm features) based upon scanning electron microscopy. Our solar-cell device results show that the crosslinked naphthalene diimide polymer gives a higher open-circuit voltage (1.08 vs 1.05 V), fill factor (average 64.43 vs 58.77%), and stabilized power conversion efficiency (12.28 vs 10.33%) compared to its non-crosslinked homopolymer counterpart, as well as reduced hysteresis. We attribute the improved performance to decreased work function, reduced nonradiative recombination, and higher shunt resistance.

2.2 Introduction

Hybrid organic–inorganic lead halide perovskite solar cells are a rapidly emerging photovoltaic technology that has reached power conversion efficiencies (PCEs) exceeding 26% [21]. Typically perovskite solar cells incorporate transport layers between the perovskite absorber and the charge-collecting electrodes to improve carrier selectivity. Metal-oxide-based electrontransport layers (ETLs) have been widely used in *n–i–p* perovskite solar cells for a variety of reasons including their moderate to high electron mobilities, good energy alignment with the perovskite conduction band, and wide bandgaps that reduce parasitic absorption and offer hole-blocking capability [22, 23]. TiO_2 remains the most common ETL used in state-of-the-art n–i–p cells but requires high processing temperatures and exhibits photoinstability [24].

Organic electron transport materials represent a possible alternative to metal oxides. Organic semiconductors offer processing flexibility, tunable energy level alignment, and may offer decreased nonradiative recombination losses at the electron-extraction interface[25, 20]. Of the existing organic semiconductor ETLs, fullerenes have been widely adopted and have produced efficient devices in both normal (*n–i–p*) [26] and more commonly in inverted (*p–i–n*) architectures[27]. Fullerenes offer good charge-transport properties but have poor solubility and suboptimal transparency in the visible. Furthermore, fullerenes can be a substantial source of interfacial recombination losses [20, 28], and devices incorporating fullerenes as ETLs can suffer from issues of long-term stability [29, 30].

Alternative nonfullerene organic ETLs have been employed as small molecules and polymers including perylene diimides [31, 32], naphthalene diimides [33, 34, 35], and azaacenes [36, 37]. Herein, we pursue the strategy of crosslinkable naphthalene diimide-based electron transport layers. We chose naphthalene diimides because they possess high transparency throughout the visible region and electron affinities comparable with those of perovskites combined with high hole-blocking ionization energies, and, in some cases, good electron transport properties [38]. Furthermore, the synthesis of naphthalene diimides is straightforward and can be readily modified to tune both their solubility and electron affinity via substitution at the imide and naphthalene core positions [39]. Naphthalene diimide acceptors have been incorporated in a number of polymeric architectures for various applications in organic electronics [40] but less widely in perovskite photovoltaics.

Herein, we also focus on crosslinking the naphthalene diimide-based ETLs because crosslinking offers many possible processing and stability advantages. For example, crosslinked charge transport layers can be used to increase the robustness of derived organic electronic devices toward degradation [36, 41, 42]. Crosslinking also imparts solvent resistance, which can allow for the deposition of subsequent layers from solution in nonorthogonal solvents. Numerous crosslinking approaches have been used for transport layers in the literature [43]. Here, we chose a copolymerization strategy incorporating a cinnamate containing comonomer. The cinnamate functional group is relatively easily incorporated into monomers bearing a polymerizable group and is compatible with a wide range of polymerization methods [44]. Cinnamates are particularly attractive crosslinking groups because they undergo selective dimerization, avoiding the need for an added photoinitiator and preventing unwanted functionalization of electroactive portions of the polymer [45]. Additionally, they are tolerant of molecular redox dopants, allowing for doping before or after insolubilization. Crosslinking can be achieved via mild photoirradiation with a hand-held UV lamp [46, 47, 48]. Photo-crosslinking offers advantages compared to thermal crosslinking as the process does not require high temperature annealing and thus can be used on plastic substrates or in top (rear) charge selective contacts without degrading the underlying perovskite layer.

Developing new nonfullerene organic ETLs for perovskite solar cells remains a considerable challenge. The Marder and Bach groups previously reported the use of a naphthalene diimide side chain homopolymer that achieved stabilized PCEs of >13.5% in *n–i–p* perovskite solar cells [49]. Here, we report the synthesis, characterization, and material properties of a related new copolymer (NDI-CL) which incorporates cinnamate crosslinking groups. We demonstrate this polymer's high transparency, thermal stability, photo-crosslinking, and n-doping via solution and sequential processing. We demonstrate its applicability in perovskite solar cells through characterization of solar cell device performance relative to its uncrosslinked homopolymeric counterpart (NDI-1) in *n–i–p* devices with an MA-free perovskite absorber (MA = methylammonium).

2.3 *Results and discussion*

Figure 2.1 shows the polymer structures and their syntheses. The naphthalene diimide monomer (1) and the corresponding homopolymer (NDI-1, see Figure A.1 for its molecular structure) were synthesized for this work (Mn = 54.5 kDa, = 1.50) following methods previously reported [49]. The cinnamate norbornene monomer was synthesized over two steps (Figure A.2): the commercially available methyl 4-hydroxycinnmate (2) was etherified to methyl 4-(3-hydroxypropoxy)cinnamate (3) by deprotonation with anhydrous potassium carbonate and alkylation with 3-bromo-1-propanol in N,N-dimethylformamide (DMF). The norbornene cinnamate monomer (4) was then synthesized by a Steglich esterification with exo-5-norbornenecarboxylic acid using dicyclohexylcarbodiimide (DCC) and catalytic 4-dimethylaminopyridine (DMAP). The polymer (NDI-CL) was synthesized by ring-opening metathesis polymerization (ROMP) of the naphthalene diimide monomer and cinnamate monomer in a 7:3 ratio (Figure A.5), respectively, with a Grubbs first generation catalyst in dichloromethane (DCM) (Mn = 45.4 kDa, = 1.17). The SEC (GPC) traces of both polymers in chloroform are shown in Figure A.7. The polymer exhibited good solubility in low polarity solvents commonly used in device processing such as chloroform, chlorobenzene, and dichlorobenzene.

We characterized the optical properties and crosslinking of thin films of NDI-CL cast from chlorobenzene. The UV–vis absorption spectrum of NDI-CL prior to crosslinking shows a vibronically structured feature similar to that of small-molecule unsubstituted NDIs (Figure 2.2a) [39], with a broad unstructured absorption peaking at ca. 310 nm attributable to the absorption of the para-alkoxy-substituted cinnamate moiety [47]. We then photoirradiated the films at 365 nm with a hand-held UV lamp for 25 min; the observed changes in the absorption spectrum over time - the absorbance of the cinnamate feature decreases to reach a near minimum after ca. 20 min irradiation (Figure 2.2a) - which we attribute to the [2 + 2] cycloaddition reaction of the cinnamate. Subsequently, in Figure A.9, we demonstrate the solvent resistance of the films toward both the casting solvent and the perovskite ink solvent mixture, chlorobenzene, and 4:1 DMF:DMSO (DMSO = dimethyl sulfoxide), respectively, by spin coating each solvent atop the crosslinked films and showing

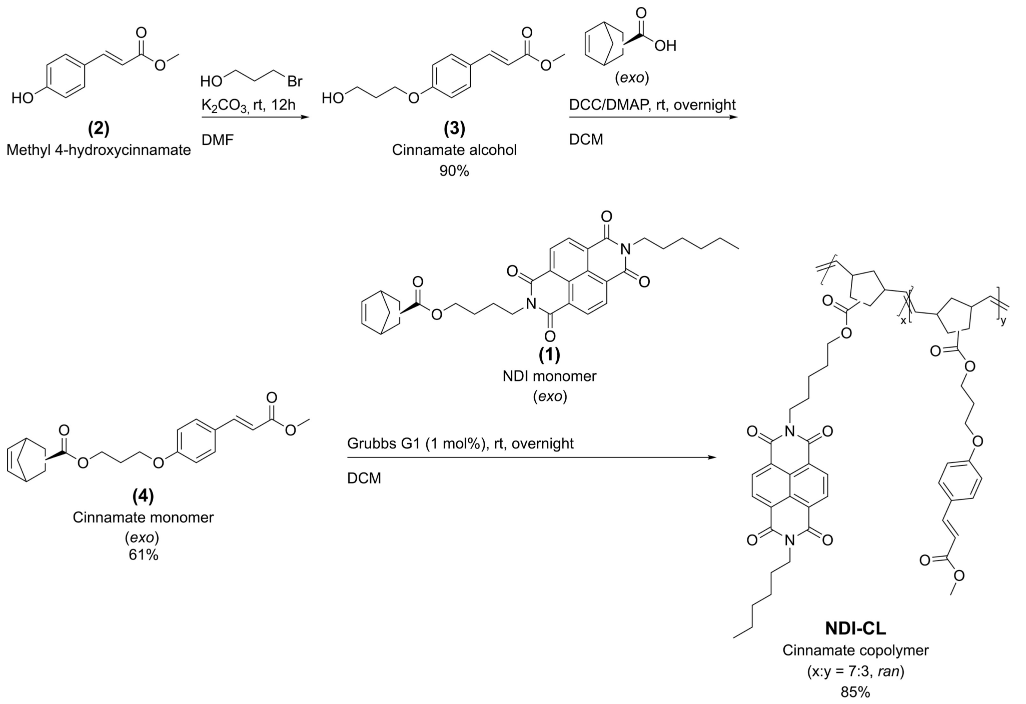

Figure 2.1: Synthesis and molecular structure of NDI-1 and the cinnamate copolymer (NDI-CL).

negligible changes in the absorption spectrum.

Once we had established an effective crosslinking protocol, we sought to investigate the charge-transport properties of these materials. In the absence of doping, the conductivities were below the limit of detection (<10^{-10} S/cm) of our apparatus. We used the highly reducing but moderately air-stable dimeric benzimidazole dopant, (N-DMBI)$_2$, as a reducing agent [50]. Solution doping was carried out on NDI-1 (9 mol % dimeric dopant) without the addition of a crosslinker. Solution doping of the copolymer (9 mol % dimeric dopant) was followed by crosslinking. We also investigated a sequential doping protocol where a dopant solution (6 mg/mL) was applied to the crosslinked film followed by chlorobenzene washing step. For sequential doping, NDI-1 was cross-linked by 5% weight addition of an oligomeric azide crosslinker, 4Bx, shown in Figure A.1, followed by photoirradiation at 254 nm for 5 min [51]. Figure 2.2b shows that all polymer dopant systems exhibit modest conductivities (10^{-9}–10^{-6} S/cm). Additionally, solution-doped NDI-1 exhibited better con-

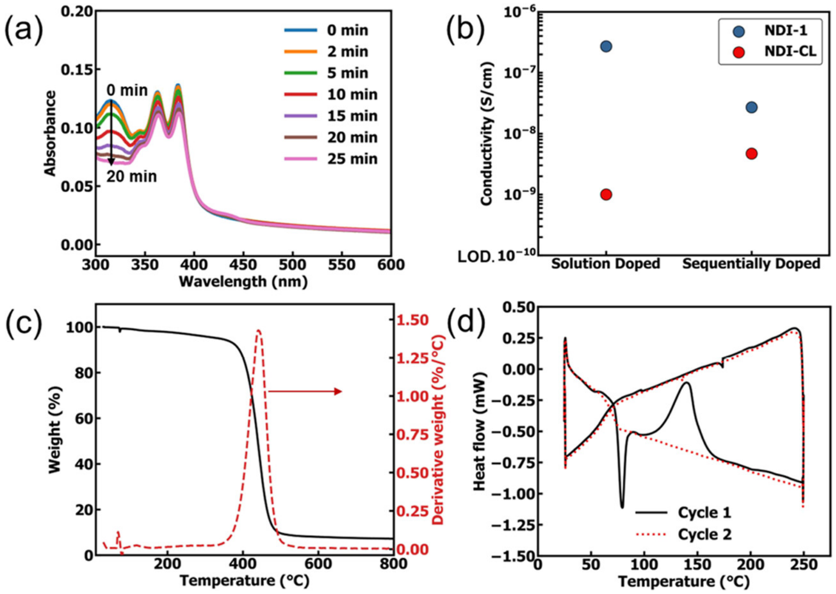

Figure 2.2: (a) UV–vis absorption spectrum of NDI-CL film on glass with increasing irradiation time with 365 nm hand-held UV lamp. (b) Conductivity of solution and sequentially doped NDI-1 and NDI-CL films; LOD represents limit of detection. (c) Thermogravimetric analysis (TGA) of NDI-CL polymer and derivative weight. (d) Differential scanning calorimetry of NDI-CL polymer.

ductivity by several orders of magnitude compared to the solution-doped and crosslinked NDI-CL. Sequentially-doped and crosslinked NDI-CL had slightly better conductivity than its solution-doped and crosslinked counterpart, perhaps because the polymer morphology was less interrupted by the doping process. In summary, doping of these side chain naphthalene diimide polymers improves their conductivity, but only achieving values of 10^{-9}–10^{-6} S/cm, which is less than other state-of-the-art n-doped electron-transporting polymers, which can reach conductivities of 1.1×10^{-3} S/cm [52].

We also characterized the thermal properties of NDI-CL (without photo-crosslinking) by thermogravimetric analysis (TGA) and differential scanning calorimetry (DSC), shown in Figure 2.2c,d, respectively. The TGA indicates the decomposition temperature of the polymer, Td, defined as temperature at which 5% of mass is lost, is ca. 335 °C. The first DSC cycle shows a small endotherm around 80 °C which likely reflects loss of the trapped solvent (note in Figure A.6 trace of DCM present according to ^{1}H NMR spectroscopy).

Additionally, a melting peak is observed around 135 °C in the first cycle. However, after the thermal history of the polymer has been cleared, we observe no transitions up to 200 °C in the second cycle. The excellent thermal stability of the polymer implies compatibility with high temperature annealing steps for the deposition of other layers in perovskite solar cell devices.

We dissolved NDI-1 and NDI-CL in anhydrous chlorobenzene to form solutions with a concentration of 1 mg/mL prior to spin coating onto the ITO substrates. The thickness of the NDI polymer films was estimated to be around 4 nm using atomic force microscopy (AFM) measurements (Figure A.10). In addition, the naphthalene diimide polymers cover the ITO substrate conformally (Figure A.10b). We further measured the work function of NDI-1 and crosslinked NDI-CL modified ITO using scanning Kevin probe microscopy (SKPM) with highly oriented pyrolytic graphite (HOPG) as the reference. We obtain uniform and homogeneous surface potential distributions with both NDI-1 and NDI-CL layers, which is beneficial for the charge collection at the interface (Figure A.11) [53]. We measured the work function of NDI-CL/ITO to be around 4.36 eV, which is lower than that of NDI-1/ITO (4.55 eV), and similar to NDI-modified ITO in a previous report [**furer2023naphthalene**]. We performed drift-diffusion simulations with Solar Cell Capacitance Simulator (SCAPS) [55, 56] to understand the impact of the reduced work function of the electron-collecting electrode on the perovskite solar cell's performance. We varied the work function of the electron-collecting electrode and found that the reduced work function will, in theory, increase the device V_{OC} (Figure A.12).

To compare device performance, we focused our analysis on the mixed-cation mixed-halide perovskite $\mathrm{FA_{0.83}Cs_{0.17}Pb(I_{0.85}Br_{0.15})_3}$ (we denote as Cs17Br15, $\mathrm{FA^+}$ = formamidinium), which has a bandgap of 1.63 eV [57]. Figure 2.3a shows the n–i–p device architecture used in this study. As in the previous study of NDI-1, we utilized a sparse dispersion of $\mathrm{Al_2O_3}$ nanoparticles on top of the naphthalene diimide polymers to improve wettability and obtain continuous perovskite films as the neat films of both polymers were hydrophobic (Figure A.13) [58]. The $\mathrm{Al_2O_3}$ nanoparticles should only cover partial of the surface area of the polymers and help improve wetting [59].

We used Spiro-OMeTAD as the hole transport layer (HTL) and gold (Au) as the top

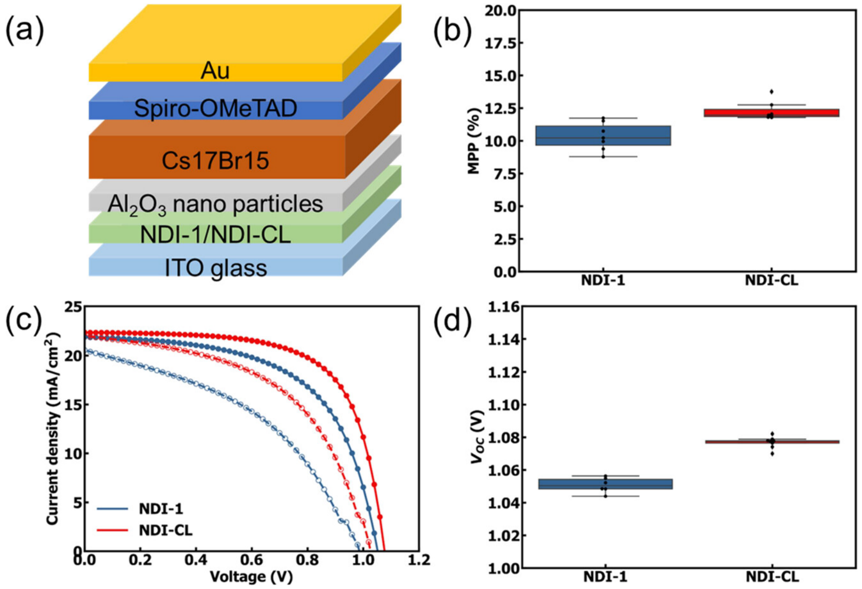

Figure 2.3: (a) Device structure used in this study (*n*–*i*–*p*). (b) Statistical distribution of the stabilized maximum power point (MPP). (c) Characteristic J–V curves (solid dots indicate reverse scan and hollow dots indicate forward scan) of perovskite solar cells based on NDI-1 and NDI-CL ETLs. (d) Statistical distribution of V_{OC} values obtained from reverse scans.

electrode. Figure 2.3c shows the characteristic J–V curves for NDI-1 and NDI-CL devices under 1 sun illumination and clearly indicates that the device using NDI-CL gives a higher V_{OC} than using NDI-1, as expected based on the work-function measurement. In addition, NDI-CL also reduces device hysteresis. We fabricated devices with $\mathrm{SnO_2}$ as the ETL (Figure A.14a) and without an ETL (Figure A.14b). The two devices also showed hysteresis, indicating that the hysteresis might be associated with the perovskite layer or perovskite/Spiro-OMeTAD interface. We measure a maximum V_{OC} of 1.08 V for the NDI-CL solar cell. Figure 2.3b,d shows the statistical distribution of maximum power point (MPP) and V_{OC} with all other photovoltaic parameters summarized in Table A.1 and Figure A.15. Overall, when using the crosslinked polymer, we see a consistent increase of V_{OC} (30 mV on average) and FF and thus PCE based on the reverse scan. The enhanced V_{OC} in NDI-CL-based solar cell devices is qualitatively consistent with the predictions from our SCAPS drift-diffusion simulations. We speculate that the enhanced FF might also be due to crosslinked NDI-CL blocking the shunting path between the perovskite and the ITO electrode or reduced nonradiative recombination at the polymer/perovskite interface (see below). We measured the dark J–V curve of NDI-1 and NDI-CL devices as shown in Figure A.16. The NDI-CL solar cell device exhibits a better diode characteristic with reduced leakage current density and a higher rectification ratio compared to the NDI-1 device [60]. This indicates that the NDI-CL solar cell device has higher shunt resistance [61] and a suppression of charge carrier recombination in the device compared to the NDI-1 solar cell device [62]. Based on the lumped equivalent circuit model [63], we estimate the shunt resistance of the NDI-CL-based perovskite solar cell to be 5270 ± 350 $\Omega \cdot \mathrm{cm}^2$, which is double that of the NDI-1-based device (2210 ± 210 Ω·cm2, Figure A.17). We further fitted the dark J–V curve to obtain the series resistances for NDI-CL and NDI-1 devices, which are 8.5 ± 1.8 and 9.9 ± 0.8 $\Omega \cdot \mathrm{cm}^2$, respectively. In addition, we obtain stabilized power output (SPO) efficiencies of 12.28 and 10.33% for solar cells using NDI-CL and NDI-1, respectively (Figure 2.3b and Table A.1).

To understand the differences in performance between NDI-1 and NDI-CL devices, we examined the influence of NDI-1 and NDI-CL on the quality of perovskite film formation. Figure 2.4a shows the X-ray diffraction (XRD) patterns of perovskite Cs17Br15 on top of the NDI-1- and NDI-CL-modified ITO substrates. The peak positions, full width at half maximum (FWHM), and peak intensities are indistinguishable, and we conclude therefore that the crystallinity of perovskite Cs17Br15 remains the same. In addition, the UV–vis absorption spectra show nearly identical absorption for Cs17Br15 films deposited on the two different substrates (Figure 2.4b). Figure 2.4c,d shows the photoluminescence (PL) lifetime and PL emission of Cs17Br15 on NDI-1- and NDI-CL-modified ITO substrates. We measure a longer lifetime (∼74 ns) with stretched exponential fitting for perovskite on NDI-CL-modified ITO in comparison to that on NDI-1 (∼25 ns) when excited from the ITO side with a 640 nm wavelength. Accordingly, the PL emission of Cs17Br15 on NDI-CL is 6.5 times higher than that of Cs17Br15 on NDI-1, which is consistent with an enhanced PL lifetime, suggesting a potential reduction of defect density at the bottom interface. The suppressed nonradiative recombination may be due to a chemical passivation effect of NDI-CL, or simply reduced coupling between the NDI and perovskite due to the cinnamate, which may be partially responsible for the improved device performance observed with NDI-CL, especially improvements in the V_{OC}.

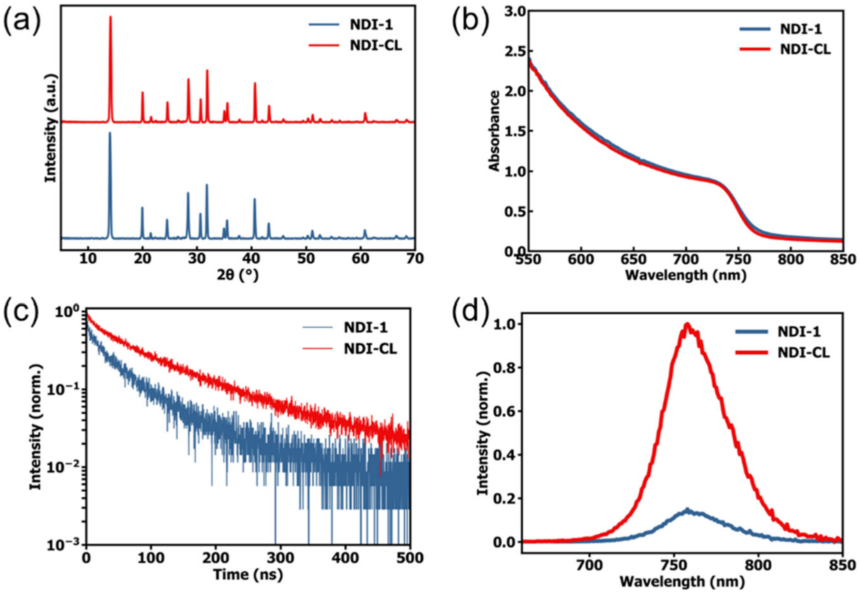

Figure 2.4: (a) XRD patterns, (b) UV–vis absorption spectra, (c) time-resolved PL (excited from ITO side with 640 nm laser), and (d) steady-state PL emission (excited from ITO side with 640 nm wavelength) of Cs17Br15 coated on NDI-1 and NDI-CL.

The morphology and grain structure of perovskite films also play an important role in device performance.[64, 65] We used scanning electron microscopy (SEM) imaging to investigate the morphology of Cs17Br15 perovskite films deposited on NDI-1- and NDI-CL-modified ITO substrates. Figure 2.5a,b shows top view SEM images of Cs17Br15 perovskite films on NDI-1 and NDI-CL. The perovskite films are dense and pinhole-free on both NDI-1- and NDI-CL-modified ITO substrates with smooth and clean surfaces, indicating good film quality. Figure 2.5c,d shows the corresponding grain size distributions for the two cases (approximating that SEM morphology corresponds to the grain structure, while acknowledging that this approximation can be inaccurate.[65]). The average grain sizes obtained from the SEM images (324 ± 99 vs 289 ± 108 nm) are similar for Cs17Br15 perovskite on NDI-1- and NDI-CL-modified ITO substrates. The surface roughness of the perovskite film on NDI-CL-modified ITO is 13.6 nm, slightly lower than that of perovskite on NDI-1, which is 18.5 nm (Figure A.18). A slightly smoother perovskite film on NDI-CL should also be beneficial for device performance.

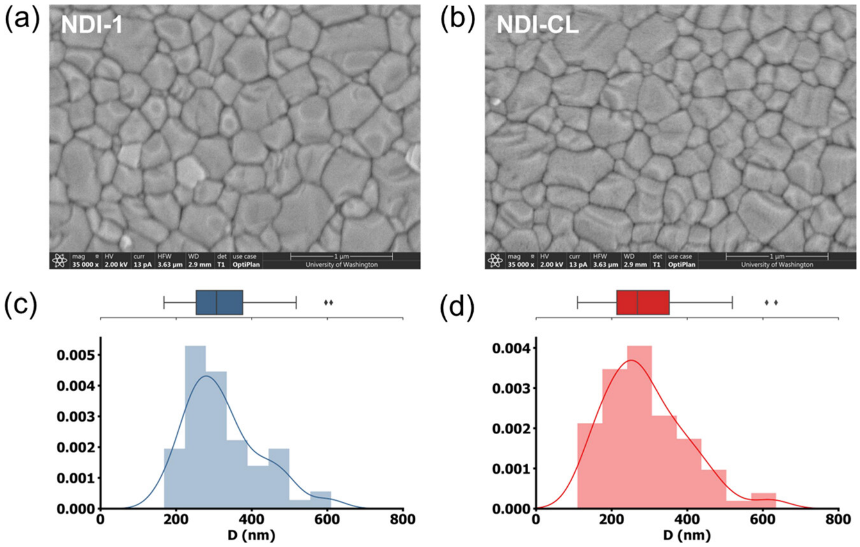

Figure 2.5: Top view SEM images of perovskite Cs17Br15 on (a) NDI-1- and (b) NDI-CL-modified ITO substrates. Corresponding grain size distributions of perovskite Cs17Br15 on (c) NDI-1- and (d) NDI-CL-modified ITO substrates.

2.4 Conclusions

In summary, we report a photo-crosslinkable naphthalene diimide copolymer as ETL for solution processed perovskite solar cells. The crosslinked ETL, NCI-CL, exhibits both high transparency of over 90% in the visible region and high thermal stability (∼300 °C). NDI-CL-modified ITO shows a slightly lower work function than ITO modified with the non-crosslinked NDI-1. Our solar cell device results show that the crosslinked NDI-CL polymer leads to slightly higher V_{OC}, FF, PCE, and less hysteresis than its non-crosslinkable NDI-1 counterpart. The average V_{OC} is enhanced to ∼1.08 V from ∼1.05 V with stabilized PCE increasing to 12.28% from 10.33% on average. We ascribe the improved performance to the decreased work function of the NDI-CL-modified ITO, and higher shunt resistance with crosslinked naphthalene diimide polymer-based perovskite solar cells. This work demonstrates that a crosslinked polymer ETL works for perovskite solar cells, which provides insights into the design of polymer electron-transport materials for perovskite solar cells.

2.5 Materials and methods

Materials. All chemicals were purchased from commercial sources and used as received unless stated otherwise. Column chromatography was carried out using silica gel (46–63 µm, Sorbent) as the stationary phase, and thin-layer chromatography (TLC) was performed on precoated silica-gel plates (0.25 mm thick, 60F254, EMD, Germany) and visualized under UV light. Nuclear magnetic spectroscopy measurements were carried out on Bruker Avance III 400 or Avance III HD 500 MHz instruments and calibrated using the solvent residual as an internal reference ($CHCl_3$, 7.26 ppm ^{1}H NMR, 77.16 ppm ^{13}C NMR). Polymers were analyzed using a Tosoh EcoSEC HLC 8320 GPC system equipped with a TSKgel SuperHZ-L column with a $CHCl_3$ eluant containing 0.25% NEt3 at a flow rate of 0.45 mL/min at 40 °C. All number-average molecular weights and dispersities were calculated from refractive index chromatograms using PStQuick Mp-M polystyrene standards. Elemental analyses were carried out by Atlantic Microlabs using a LECO 932 CHNS elemental analyzer.

Materials for Halide Perovskite and Perovskite Film preparation. All precursors were used without any further purification and were stored in a nitrogen-filled glovebox. Formamidinium iodide (FAI, Greatcell), cesium iodide (CsI, Sigma), lead iodide (PbI_2, Sigma), and lead bromide ($PbBr_2$, Sigma) were dissolved in a mixture of anhydrous N,N-dimethylformamide (DMF, Sigma) and anhydrous dimethyl sulfoxide (DMSO, Sigma) (volume ratio of 4:1) to prepare a 1.2 M solution of $FA_{0.83}Cs_{0.17}Pb(I_{0.85}Br_{0.15})_3$ according to the stoichiometry. Patterned indium tin oxide (ITO, from thin film devices) glass substrates and glass substrates were cleaned by sequentially sonicating in water containing 2% Micro-90 detergent, DI water, acetone, and 2-propanol (IPA) for 10 min, respectively, followed by plasma-cleaning for 5 min. The perovskite precursor solution was filtered with a PTFE filter before use, and 50 µL of the solution was deposited on top of the substrate and spin-coated at 4000 rpm for 60 s. When 35 s remained, 120 µL of anhydrous chlorobenzene (CB, Sigma) antisolvent was dropped from the top. The perovskite films were then annealed at 100 °C for 30 s and at 150 °C for 10 min. The preparation of perovskite films was carried out in a nitrogen-filled glovebox.

Fabrication of Perovskite Solar Cells. To fabricate the Cs17Br15 devices, NDI-1 and NDI-CL were dissolved in anhydrous chlorobenzene (CB) at a concentration of 1 mg/mL, and 60 µL of the solution was deposited onto the ITO substrate before spin coating at 3000 rpm for 30 s. The NDI-CL was then put under UV (UVGL-25 Compact UV Lamp) light at 365 nm (5 cm above the film) for 20 min to crosslink the polymer. The Al_2O_3 (Sigma) was diluted in isopropyl alcohol (IPA) with a volume ratio of 1:150, which was spin-coated at 3000 rpm for 30 s, followed by annealing at 100 °C for 1 min. The perovskite films were deposited in the same way as that mentioned above. Spiro-OMeTAD (Xi'an Polymer light technology Corp.) was used as the hole transport layer. The HTL solution was prepared by dissolving 60 mg of Spiro-OMeTAD in 700 µL CB, with addition of 22.5 µL 4-tert-butylpyridine (t-BP, Sigma-Aldrich) and 15.5 µL of Li-TFSI solution (520 mg/mL in acetonitrile, ACN, Sigma-Aldrich). The 60 µL HTL solution was spin-coated on top of perovskite at 3000 rpm for 30 s in a nitrogen-filled glovebox. Subsequently, the half-stacked solar cell devices were stored in a desiccator for 24 h. To complete the device fabrication, 80 nm of Au was thermally evaporated onto the devices.

Structural and Optical Characterization. A Bruker D8 Powder X-ray diffractometer (XRD) with a high-efficiency Cu anode microfocus X-ray source and sensitive Pilatus 100 K large-area 2D detector was used to study the crystal information on perovskite films. PL emission (excited at 640 nm) was measured using an Edinburgh FLS1000 spectrometer with a xenon lamp light source. A PMT-980 detector was used for the PL measurements. SEM images were acquired by using a FEI Sirion SEM instrument at a 2 kV accelerating voltage. The sample structure was ITO/NDI/Al_2O_3/perovskite.

2.6 Acknowledgements

This work was primarily supported by the U.S. Department of Energy's Office of Energy Efficiency and Renewable Energy (EERE) under the Solar Energy Technology Office (SETO), Award Number DE-EE0008747. The electrical characterization of the polymers was supported by the U.S. National Science Foundation (ECCS-2141949). Work at Princeton University was supported in part by a grant from the Department of Energy Office of Basic Energy Sciences, Division of Materials Sciences and Engineering, Award Number DE-

SC0012458. D.S.G. acknowledges salary and infrastructure support from the Washington Research Foundation, the Alvin L. and Verla R. Kwiram endowment, and the B. Seymour Rabinovitch Endowment. M.T. acknowledges funding from the Office of Naval Research (Award Number N00014-20-1-2587) for her role in time-resolved photoluminescence. H.C. was supported by the National Science Foundation Graduate Research Fellowship under Grant No. DGE-2140004 and the University of Washington Clean Energy Institute (CEI) fellowship. Part of this work was carried out at the Molecular Analysis Facility, a National Nanotechnology Coordinated Infrastructure site at the University of Washington which is supported in part by the National Science Foundation (Awards NNCI-2025489 and NNCI-1542101), the Molecular Engineering & Sciences Institute, and the Clean Energy Institute. Y.S. acknowledges the use of facilities and instrumentation supported by the U.S. National Science Foundation through the UW Molecular Engineering Materials Center (MEM-C), a Material Research Science and Engineering Center (DMR-1719797). The authors acknowledge the use of facilities and instruments at the Research Training Testbed (RTT), part of the Washington Clean Energy Testbeds system. Part of this work was conducted with instrumentation supported by the University of Washington Student Technology Fee at the RTT.

Chapter 3

(3-AMINOPROPYL) TRIMETHOXYSILANE SURFACE PASSIVATION IMPROVES PEROVSKITE SOLAR CELL PERFORMANCE BY REDUCING SURFACE RECOMBINATION VELOCITY

Adapted with permission from Yangwei Shi, Esteban Rojas-Gatjens, Jian Wang, Justin Pothoof, Rajiv Giridharagopal, Kevin Ho, Fangyuan Jiang, Margherita Taddei, Zhaoqing Yang, Erin M. Sanehira, Michael D. Irwin, Carlos Silva-Acuña, and David S. Ginger. "(3-Aminopropyl) trimethoxysilane Surface Passivation Improves Perovskite Solar Cell Performance by Reducing Surface Recombination Velocity" ACS Energy Letters 2022 7 (11), 4081-4088 DOI: 10.1021/acsenergylett.2c01766 Copyright 2022 American Chemical Society.

3.1 Overview

We demonstrate reduced surface recombination velocity and enhanced power-conversion efficiency (PCE) in mixed-cation mixed-halide perovskite solar cells by using (3-aminopropyl)-trimethoxysilane (APTMS) as a surface passivator. We show the APTMS serves to passivate defects at the perovskite surface, while also decoupling the perovskite from detrimental interactions at the C_{60} interface. We measure a SRV of $\sim$125 ± 14 cm/s, and a concomitant increase of $\sim$100 meV in quasi-Fermi level splitting in passivated devices compared to the controls. We use time-resolved photoluminescence and excitation-correlation photoluminescence spectroscopy to show that APTMS passivation effectively suppresses nonradiative recombination. We show that APTMS improves both the fill factor and open-circuit voltage (V_{OC}), increasing V_{OC} from 1.03 V for control devices to 1.09 V for APTMS-passivated devices, and leads to a PCE increase from 15.90% to 18.03%. We attribute the enhanced performance to reduced defect density resulting in suppressed nonradiative recombination and lower SRV at the perovskite/transport layer interface.

3.2 Introduction

Halide perovskites are promising semiconductors for use in applications ranging from solar photovoltaics [66, 67, 68] to conventional electroluminescence [69, 70], and even as non-linear optical elements or quantum light sources [71, 72]. In photovoltaic applications, the record power-conversion efficiency (PCE) has surged to 25.7% for a single junction perovskite solar cells [73]. Despite this rapid progress, the best efficiencies being obtained today still lag behind the theoretical detailed balance limit of 32.3% (for a ~1.48 eV bandgap absorber), which is largely due to a deficit in the open-circuit voltage (V_{OC}) that results from non-radiative recombination in the bulk of perovskite films and also at the interfaces between perovskite and transport layers [74, 75, 76, 77, 78].

Previous studies have shown that surface recombination at the surface/interface of the perovskite layer in solar cells plays an important role on the device performance [20, 79, 80]. A small surface recombination velocity (SRV) enables a higher value of V_{OC} and FF [20]. Many different schemes have been proposed for surface passivation. Of these, (3-aminopropyl)trimethoxysilane (APTMS) exhibits many characteristics of an ideal surface passivator: (i) it is effective at passivating a large number of perovskite compositions [57], (ii) it is commercially available at large scales, (iii) it can be deposited from solution or vapor phases, and (iv) it is polymerizable, which should result in more stable passivation layers. Jariwala et al. previously demonstrated an effective APTMS passivation strategy for perovskites on glass substrates that reduces the SRV down to 30 cm/s (average), through which a quasi-Fermi level splitting (QFLS) of 1.31 eV can be achieved for a 1.63 eV bandgap mixed-cation mixed-halide perovskite, approaching its theoretical limit of 1.35 eV [57]. Notably, however, they did not examine the effect of APTMS passivation on working solar cells, and because thicker APTMS layers can be insulating, it has remained unclear if these improvements in SRV via coating the exposed film surface could be translated into actual solar cell performance.

In this work, we show that, by optimizing the APTMS deposition conditions, the improvements in SRV can be translated into improvements in V_{OC}, fill factor (FF), and efficiency of working solar cells. We use a methylammonium (MA)-free mixed-cation mixed-halide perovskite $\mathrm{FA_{0.83}Cs_{0.17}Pb(I_{0.85}Br_{0.15})_3}$ [81], denoted hereafter as Cs17Br15, to investigate the APTMS passivation in perovskite solar cells. By using photoluminescence quantum yield (PLQY) measurements and QFLS analysis on partial device stacks and complete perovskite solar cells, we show that the QFLS in passivated devices increases to 1.23 eV, which enhances V_{OC} up to 1.11 V compared to values of 1.10 eV and 1.04 V respectively for the unpassivated control devices.

3.3 Results and discussion

Figure 3.1a shows the schematic of the p-i-n structure of the perovskite solar cells used in this study. We use $\mathrm{FA_{0.83}Cs_{0.17}Pb(I_{0.85}Br_{0.15})_3}$ (where FA = formamidinium), which has a bandgap of 1.63 eV. We choose this composition since it has a similar bandgap to the archetypal $\mathrm{MAPbI_3}$ but exhibits a higher thermal stability [82]. For the hole-transport layer (HTL), we choose a self-assembled monolayer (SAMs) of [2-(3,6-dimethoxy-9H-carbazol-9-yl)ethyl]phosphonic acid (MeO-2PACz) for its good compatibility and easy processability [83]. Details regarding the APTMS layer deposition and perovskite solar cell fabrication can be found in Supporting Information [57].

Figure 3.1c shows the PL lifetime of the control film and APTMS-passivated film on glass substrates. We obtain a longer PL lifetime (1.2 ± 0.2 ms) for passivated perovskite films in comparison to the control perovskite films (50 ± 8 ns). We extract the SRV from the time-resolved photoluminescence (TRPL) data using the approximations described previously [20, 57] (see also Appendix B). From this approach, we conservatively estimate the average SRV after APTMS treatment is reduced to 50 cm/s or lower, consistent with our previous report [57]. Labile surface passivators such as tri-n-octylphosphine oxide, and alkanethiols, are difficult to incorporate into devices because, while they have been shown to effectively coordinate dangling bonds on undercoordinated $\mathrm{Pb^{2+}}$ sites at the perovskite surface (e.g. halide vacancies) [11, 78], they are also easily washed away or pumped off under high vacuum. However, Figure 1d shows that, because APTMS hydrolyzes to form a robust film cross-linked by Si-O-Si bonds [84], APTMS-treated films are able to retain their long PL lifetimes and low SRV values even after washing with solvents such as chlorobenzene (CB) or annealing at 100 °C and under vacuum (Figure 3.1d and Figure B.5) (See also Appendix B). Furthermore, we measure the SRV in partial solar cell stacks without a silver top electrode (ITO/MeO-2PACz/Cs17Br15/APTMS/C_{60}) to be 125 ± 14 cm/s.

We mapped the optoelectronic properties of APTMS-passivated films by fluorescent lifetime imaging microscopy (FLIM) to assess the homogeneity of passivation over the sample surface [85]. Figure B.2a and B.2b show that the control film is much dimmer in comparison to the APTMS-passivated film, while the APTMS passivated film appears much brighter, and also somewhat more heterogeneous (Figure B.2b). Previous reports have shown that additives or processing agents may enhance the PL of perovskite film via the formation of low-dimensional wide-gap perovskites at the surface [86, 87, 88]. We performed XRD to examine this possibility but we do not observe any additional diffraction peaks at low angle that are associated with the formation of low-dimensional perovskites (Figure B.3a). UV-vis absorption and steady-state PL measurements also show no evidence of a low-dimensional phase emerging in APTMS passivated films (Figure B.1 and Figure B.3b). We thus conclude that APTMS passivation has a negligible influence on the bulk perovskite structure and no (detectable) low-dimensional perovskite formed after surface passivation.

Having shown that the passivation effect of APTMS can be sustained even after solvent washing, elevated temperature, and exposure to high vacuum, we next prepare a series of half-stack and full-stack devices (the structure of the full-stack solar cells is shown in Figure 3.1a). We compared the PL emission (Figure B.6) of these half-stack or full-stack devices with and without APTMS passivation. We found that the passivated devices display 2 orders of magnitude higher PL emission intensity than the control stacks (Figure B.6b).When in contact with a C_{60} ETL, the PL intensity of both passivated and control stacks is quenched due to fast interfacial recombination processes in contact with the fullerene, consistent with previous reports [89]. However, in the presence of APTMS, this fullerene-induced quenching is diminished (Figure B.6). We measured the photoluminescence quantum yield (PLQY) using an integrating sphere under 1 Sun equivalent excitation density conditions

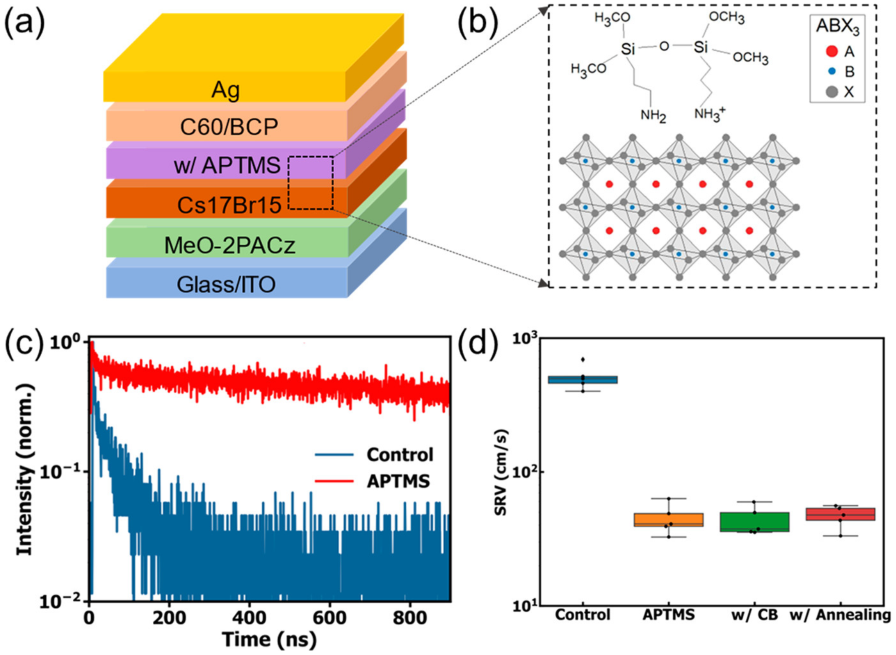

Figure 3.1: (a) Schematic of perovskite solar cell structure (p–i–n). (b) Schematic of passivation using APTMS molecule at the perovskite surface (A: FA^+, Cs^+; B: Pb^{2+}; X: I^-, Br^-). (c) PL lifetime of control and APTMS-passivated perovskite films. (d) SRV of the control, APTMS-treated films with CB treatment and annealing.

and calculate the QFLS of these stacks based on equation 1:[90, 91, 92]

$$\Delta E_F = \Delta E_{F,max} - kT|ln(PLQY_{ext})|$$

where the $\mathrm{E}_{\mathrm{F,max}}$ is the Shockley-Queisser theoretical QFLS limit, k is Boltzmann constant, T is the absolute temperature, and PLQY_{ext} is the measured external PLQY under 1 Sun conditions. Figure 3.2 shows the QFLS values for the partial device stacks at different stages of fabrication (see also Table B.1). The APTMS-passivated perovskite solar cells exhibited larger QFLS than the control perovskite solar cells, indicating that a higher V_{OC} could potentially be achieved for perovskite solar cells using APTMS surface passivation. Measuring QFLS provides understanding as to the losses at each interface as well as the effects of passivation. The Cs17Br15 perovskite, with a bandgap of 1.63 eV, possesses a theoretical maximum QFLS of 1.35 eV. However, the as-fabricated Cs17Br15 control perovskite films on glass showed a QFLS of 1.23 eV, and the control perovskite solar cell devices showed an even smaller QFLS of 1.10 eV. Depositing the perovskite onto the HTL adds some additional small losses, with a QFLS of 1.19 eV for the control, and 1.26 eV for the APTMS-passivated sample. Addition of the fullerene ETL adds significantly more loss, consistent with literature reports [77], with a QFLS of 1.15 eV for the unpassivated control. Notably, the APTMS provides a significant enhancement in performance at this stage, preserving a QFLS of 1.24 eV. Finally, the QFLS in the full device stack is 1.10 eV for the control and 1.23 eV for the APTMS device. The V_{OC} of both control and APTMS devices is lower than the measured QFLS, but benefits of the APTMS are still clear. The V_{OC} of the perovskite solar cells is smaller than the measured QFLS under the same AM1.5 illumination intensity by ∼130 mV. We attribute this remaining difference between measured V_{OC} and the calculated QFLS in the perovskite solar cells to energy misalignment between the charge transporting layers and perovskite layer, suggesting there is still room to optimize energy level alignment in this particular device stack [93]. In addition to the Cs17Br15 medium bandgap perovskite, we extended the APTMS passivation to a wide bandgap mixed-cation mixed-halide perovskite $\mathrm{FA_{0.83}Cs_{0.17}Pb(I_{0.75}Br_{0.25})_3}$ (denoted as Cs17Br25) with a bandgap of ∼1.69 eV, which can be used for building tandem solar cells. As shown in Figure B.7, the QFLS of Cs17Br25 can be increased to ∼1.25 eV (Figure B.7b). This increase in the QFLS of a wide bandgap perovskite is beneficial for the perovskite/silicon tandem photovoltaic devices.

Thus far we have interpreted the improvements in PL lifetime, SRV and PLQY as resulting from a reduction in the surface trap density. We next verify these interpretations using excitation-correlation photoluminescence (ECPL) spectroscopy on perovskite solar cells. ECPL spectroscopy is an optical method which reveals the nonlinear interactions among the photogenerated carriers and provides insights on nonradiative decay channels of semiconducting materials. ECPL uses two temporally delayed pump pulses with identical intensities and energy (2.638 eV) [94, 95]. Kanada et al. applied ECPL to study the recombination and trapping dynamics of carriers within metal halide perovskite materials and were able to quantitatively extract the trap density, the bimolecular recombination coefficient, and the Auger recombination rate [94]. Here, we apply ECPL spectroscopy to understand recombination and trapping dynamics of the photogenerated carriers in our

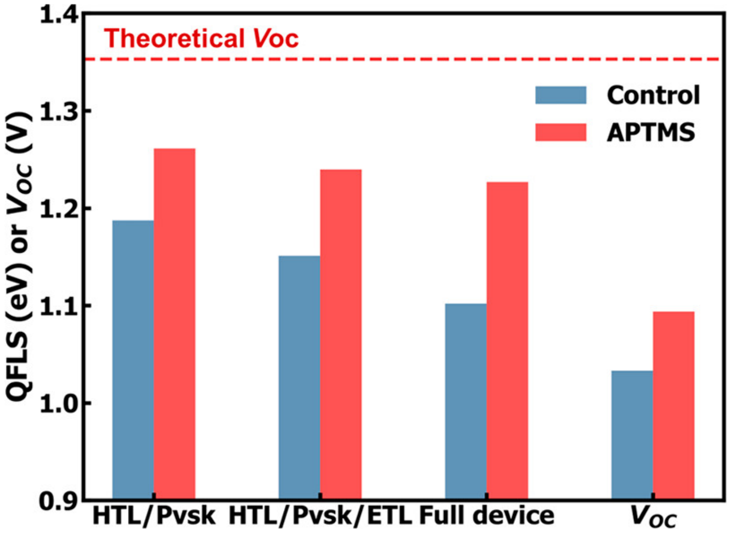

Figure 3.2: QFLS and measured V_{OC} of the perovskite stack at different levels of perovskite solar cell device completion and operation (Pvsk: perovskite).

control and APTMS-passivated perovskite solar cells. A schematic of the ECPL set-up can be found in the references [95]. Figure 3.3 shows the ECPL spectroscopy results on the control and APTMS-treated perovskite solar cells with different laser excitation fluences ranging from 4 to 36 μJ/cm^2 per pulse. Trap-assisted recombination results in a positive nonlinear response while Auger recombination results in a negative response. At the lowest fluence, both devices show positive ECPL values that matches with a dominating trap-limited behavior; further interpretation of ECPL signals can be found in reference [94]. With increasing fluence, responses of both control and APTMS-passivated perovskite solar cells decrease due to trap filling, resulting in Auger recombination becoming the dominant pathway. The APTMS-passivated perovskite solar cell shows lower initial signal compared to the control perovskite solar cell at a fluence of 4 μJ/cm^2, as shown in Figure 3.3a and b, which we ascribe to the lower defect density in the APTMS-passivated perovskite solar cell [94]. This interpretation is in good agreement with the enhanced PL emission from this stack at low fluence. As summarized in Figure 3.3b and d, the control solar cell requires a high fluence of $\sim$14.2 μJ/cm^2 to reach the Auger recombination regime, while the APTMS passivated solar cell device shows signs of Auger recombination at a lower fluence of only

~8.2 μJ/cm^2. The lower fluence required to observe Auger recombination in the passivated solar cell is consistent with an increase in carrier lifetimes and increase in carrier density at a given excitation fluence. As such, the ECPL measurement on the solar cell further confirms that APTMS can suppress the trap-assisted non-radiative recombination, which is consistent with our PL emission and QFLS results.

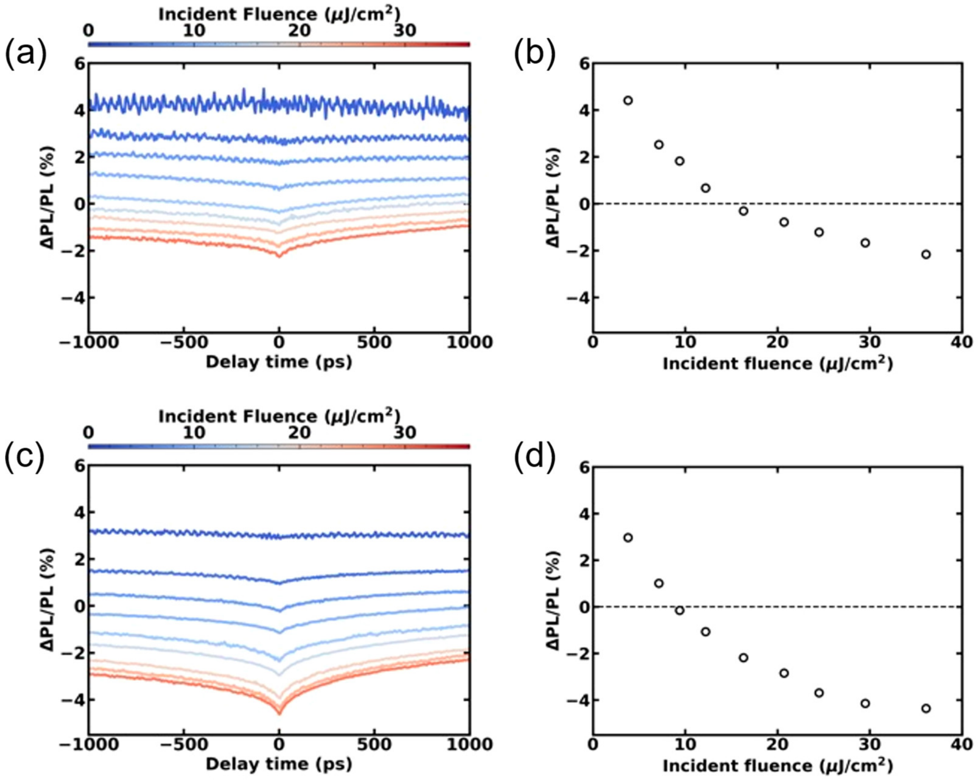

Figure 3.3: ECPL dynamics of (a) control and (c) APTMS-passivated perovskite solar cells. ECPL at t = 0 ps for (b) control and (d) APTMS-passivated perovskite solar cells under various laser fluences.

The reduced SRV and enhanced QFLS in perovskite solar cells with APTMS passivation are promising indicators that point to improved device performance relative to the controls. To corroborate the effect of APTMS passivation, we fabricated solar cells with a p-i-n structure with and without APTMS surface treatment (device structure shown in Figure 3.1a). As expected, the V_{OC} is clearly improved after the APTMS passivation as depicted in the current density-voltage (J–V) curves of the representative Cs17Br15 control device and APTMS-passivated perovskite solar cells (Figure 3.4a). Figure 3.4b shows the maximum power point tracked efficiency (η_{mpp}) for the control and APTMS-passivated perovskite solar cells. The control solar cells achieved a η_{mpp} of ∼16% while the APTMS-passivated solar cells achieved a higher η_{mpp} of ∼18%. Device performance is plotted in Figure 3.4c-f with statistics (based on the reverse scans) summarized in Table B.2. The control solar cells displayed an average PCE of 15.90% with an FF of 72.83% and a V_{OC} of 1.03 V (average), while the PCE of the APTMS-passivated solar cells increased to an average value of ∼18.03% with enhanced V_{OC} (1.09 V) and FF (∼77.78%). Overall, the APTMS-passivated solar cells displayed a consistent enhancement in V_{OC} and PCE. We attribute the improvement in the device V_{OC} with APTMS surface treatment to the reduced defect density, smaller SRV at the interfaces and a consequently higher QFLS. We note that in addition to the expected increase in V_{OC} due to the reduction in SRV. We also observe an enhancement of the FF following APTMS passivation. Simulations show that while FF is less sensitive to SRV than V_{OC}, it still can benefit from reducing SRV over the range we measure in these device stacks (∼125 cm/s) [20]. It is possible that APTMS also helps improve FF by suppressing physical shunting and pinholes, though this cannot be distinguished from reduction in effective recombination using the current data [96].

In some respects, the improved device performance is surprising: one might expect APTMS, an insulating molecule, to block photocurrent extraction, yet short-circuit current (J_{SC}) values are comparable in both types of perovskite solar cells. Therefore, we performed a combination of scanning probe microscopy (SPM) techniques to better understand both the uniformity in coverage of the APTMS coating as well as how charge carriers are extracted from the solar cell devices. First, we used atomic force microscopy (AFM) to determine the surface coverage of the APTMS treatment by mapping the elastic modulus E and adhesion Fa, along with the topography of the passivated films since perovskite films and APTMS surfaces have anticipated significantly different mechanical properties [97]. For example, the elastic modulus of a similar siloxane polymer is ∼0.1-10 MPa [98], while those for a metal-halide perovskites are in the range 1-20 GPa [99, 100, 101]. Figure B.8 shows topography and mechanical mapping of APTMS-treated perovskite films. The hazy part in the topography

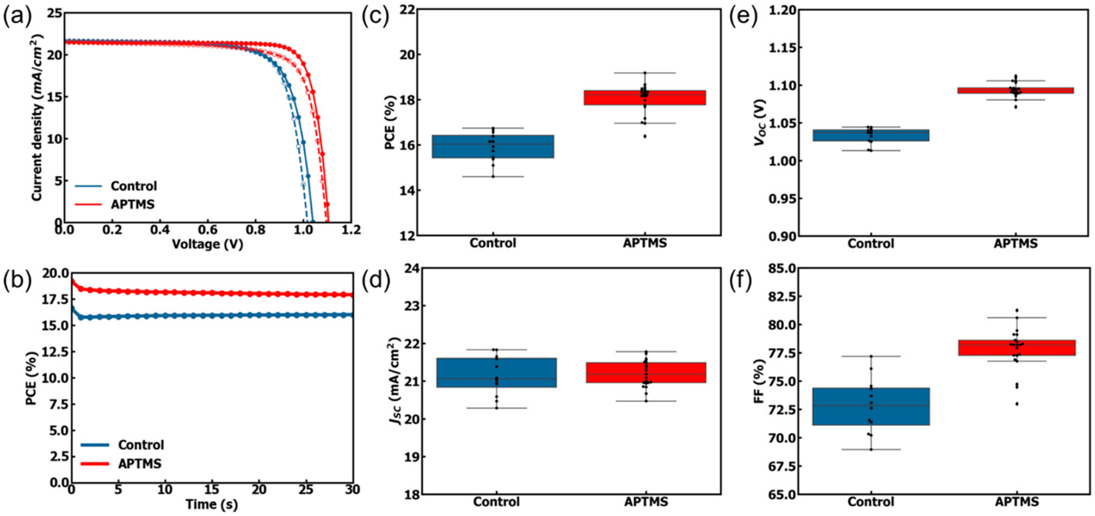

Figure 3.4: (a) J–V curve of representative control and APTMS-passivated solar cells (the solid and dotted lines are reverse and forward scans, respectively). (b) η_{mpp} of control and APTMS-passivated solar cells. Statistics of (c) PCE, (d) J_{SC}, (e) V_{OC}, and (f) FF of device performance without and with APTMS passivation based on reverse scans.

has a modulus of ∼10 MPa, similar to the value expected for a siloxane polymer. Therefore, we assign these regions to the thicker areas of polymerized APTMS. The remaining area displays a much higher modulus, however, since the tip used is only sensitive to the softer polymerized APTMS, these areas are therefore indicative of the lack of APTMS, or exposed perovskites. In addition to modulus, adhesion is also obtained which is more sensitive to the surface properties than modulus measurement. While Figure B.8c is well correlated with the topography results, the regions of higher adhesion are well-correlated with regions of APTMS. These results provide insight into the reason charges are still able to be extracted in a solar cell device with APTMS passivation. With non-uniform surface coverage, some regions of APTMS are thinner allowing for charge carrier transport (presumably, improved deposition methods could be used to further optimize the coating thickness and uniformity as desired).

We also performed conductive AFM on half-stack devices (ITO/MeO-2PACz/Cs17Br15) to confirm how charge carriers are extracted in APTMS solar cells. Figure 3.5 shows the cAFM results on the control and APTMS-passivated half stacks under dark. Notably, while the APTMS-passivated half stack device shows that the current is blocked in thicker APTMS areas, we also see that there is a sufficient area of the thinner APTMS coating to allow current to be extracted. As shown in Figure 3.5b, a 2 min APTMS layer deposition reduces the number of conducting pixels by roughly 50% while a control device is completely conductive, showing the insulating nature of APTMS. However, after deposition of the C_{60} ETL, cAFM reveals uniform conductivity and photoconductivity, indicating that the smaller percentage of contact points in the APTMS-passivated device is sufficient to achieve spatially uniform current extraction (as homogenized by the fullerene layer, Figure 3.5d and Figure B.11b). When we use an APTMS deposition time of 5 min, as we used for the best performing perovskite solar cell, the cAFM data shows only ~5% of the pixel areas are conducting (Figure 3.5c). Nevertheless, the device data indicate that these devices still achieve a J_{SC} value of $\sim$21 mA/cm^2. While initially such an observation might seem surprising, these data are consistent with previous results in our group using laser beam-induced current (LBIC) [102], where we showed that the cAFM heterogeneity in perovskites is drastically reduced upon evaporation of the top contact. In this sense, it is possible for APTMS-treatment both to passivate the surface, and to reduce the interaction of the perovskite with the PL-quenching fullerene layer while still allowing sufficient contact to extract almost all the photocurrent. We speculate that similar mechanisms underpin the widespread use of insulating interlayers or dispersants such as PMMA in the literature: their primary role may be to reduce contact with PL-quenching extracting contacts, much like a passivated-emitter rear collector (PERC) silicon cell reduces surface recombination with an insulating passivating layer that has a sufficient density of windows for current extraction [103, 104].

3.4 Conclusions

In summary, we have demonstrated a V_{OC} enhancement for a mixed-cation mixed-halide perovskite solar cells by using APTMS as a surface passivator. We ascribe the increased V_{OC} to the decrease in the defect density as verified by the enhanced PL emission, smaller SRV, and increased QFLS after APTMS passivation. In addition, we demonstrate that APTMS passivation can survive the solvent treatment, high temperature annealing and

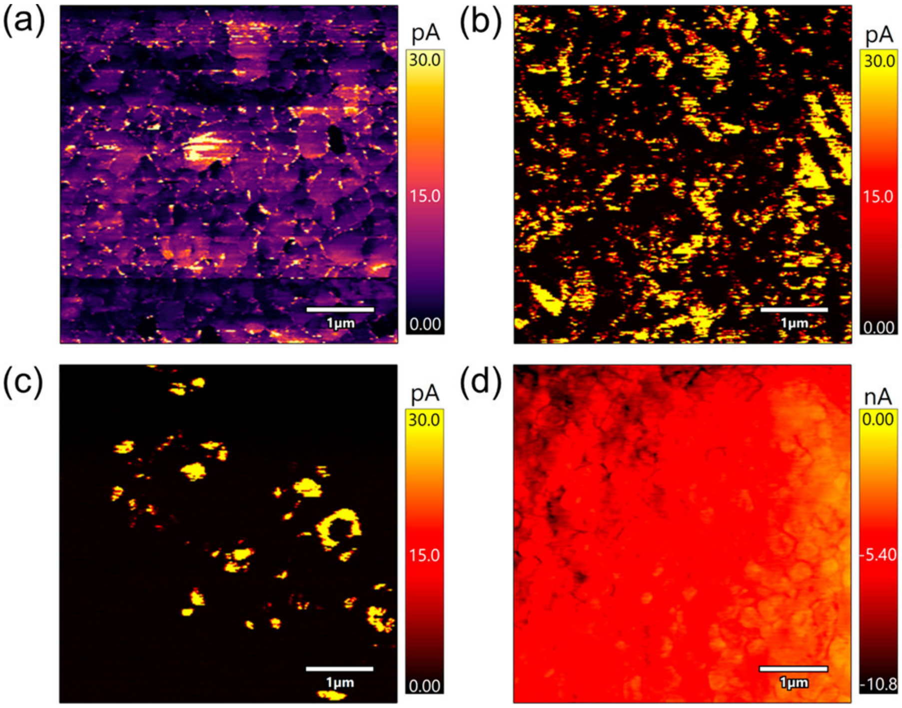

Figure 3.5: cAFM of (a) ITO/MeO-2PACz/Cs17Br15, 1.5 V bias, (b) ITO/MeO-2PACz/Cs17Br15/APTMS (2 min), and (c) ITO/MeO-2PACz/Cs17Br15/APTMS (5 min), in the dark with a sample bias of 1.5 V. (d) ITO/MeO-2PACz/Cs17Br15/APTMS (5 min)/C_{60}, under light (488 nm) with a sample bias of -1.5 V. These data show that while the APTMS layer reduces the number of conducting pixels in panels b and c, the number of contact points is sufficient to achieve uniform optoelectronic functionality once in contact with an ETL (d).

high vacuum conditions which makes it a suitable passivator for many different device fabrication or manufacturing strategies. ECPL studies further confirm that the nonradiative recombination is suppressed via APTMS passivation. Finally, SPM techniques reveal that the APTMS polymerizes heterogeneously at the perovskite surface but still ensures efficient extraction of carriers. This work demonstrates the importance of surface passivation in reducing defect density and improving the device performance in mixed-cation mixed-halide perovskite solar cells, while providing a potential route forward for large-scale manufacturing of improved perovskite semiconductor interfaces.

3.5 Materials and methods

3.6 Acknowledgements

This paper is based on work supported primarily by the U.S. Department of Energy's Office of Energy Efficiency and Renewable Energy (EERE) under the Solar Energy Technology Office (SETO), Award Number DE-EE0008747. The atomic force microscopy imaging work (K.H.) was supported by the U.S. Department of Energy, Office of Basic Energy Sciences, Division of Materials Sciences and Engineering under Award DOE-SC0013957. Part of this work was carried out at the Molecular Analysis Facility, a National Nanotechnology Coordinated Infrastructure site at the University of Washington which is supported in part by the National Science Foundation (NNCI-1542101), the Molecular Engineering & Sciences Institute, and the Clean Energy Institute. Y.S. thanks Prof. Seth R. Marder and Stephen Barlow for their suggestions and review of this work and acknowledges the use of facilities and instrumentation (fluorometer) supported by the U.S. National Science Foundation through the UW Molecular Engineering Materials Center (MEM-C), a Material Research Science and Engineering Center (DMR-1719797). Y.S. acknowledges the financial support from the State of Washington through the University of Washington Clean Energy Institute (CEI fellowship). D.S.G. acknowledges salary and infrastructure support from the Washington Research Foundation, the Alvin L. and Verla R. Kwiram endowment, and the B. Seymour Rabinovitch Endowment.

Chapter 4

SULFONATE ANIONS SUPPRESS INTERFACIAL RECOMBINATION IN PEROVSKITE SOLAR CELLS VIA SURFACE FIELD AND ELECTRONIC DECOUPLING

This chapter is from the manuscript in preparatoin: Yangwei Shi, Declan P. McCarthy, Kevin Ho, Fangyuan Jiang, Zhaoqing Yang, Xiaofeng Xiang, Robert J. E. Westbrook, Margherita Taddei, Hannah Contreras, Stephen Barlow, Scott T. Dunham, Neal R. Armstrong, Seth R. Marder and David S. Ginger. "Sulfonate Anions Suppressing Interfacial Recombination in Perovskite Solar Cells via Surface Field and Electronic Decoupling".

4.1 Overview

We demonstrate that benzylammonium tosylate (BzAOTs) and benzylammonium triflate (BzAOTf) interlayers reduce interfacial nonradiative recombination at the perovskite/C_{60} interface and enhance open-circuit voltage (V_{OC}) in mixed-halide mixed-cation wide-bandgap (~1.7 eV) metal-halide perovskite solar cells. The integrated photoluminescence (PL) intensities in the presence of BzAOTs and BzAOTf interlayers and C_{60} were respectively 7.6 times and 4.8 times higher than that of the control perovskite film in contact with only a C_{60} , respectively. Correspondingly, the V_{OC} of the solar cell devices was improved to ~1.18 V for BzAOTs- and BzAOTf-treated devices compared to 1.14 V for the control devices. The champion efficiency for the BzAOTf- and BzAOTs-treated devices was 19.6% in comparison to the control device with 17.50%. Using scanning electron microscopy (SEM), we show that the surface treatment reconstructed the top surface of perovskite films with negligible change in bulk properties. Using Kelvin probe microscopy (SKPM), we measure the work function of the perovskite film with BzAOTs treatment to be ~0.7 eV lower than in the control, which we assign to the large dipole moment of the OTs anion. On the other hand, BzAOTf treatment results in a negligible change in the work function of the perovskite film. We propose the resulting surface field induced by the OTs anion reduces recombination at the perovskite/C_{60} interface by repelling carriers, consistent with the longer carrier lifetime than the BzAOTf-treated and control perovskite films. The BzAOTs interlayer improves the device performance by reducing interfacial nonradiative recombination via surface field while BzAOTf decouples the perovskite film from contact-induced traps at C_{60} interface.

4.2 Introduction

Halide perovskites are emerging semiconductor materials with applications in photovoltaics [66, 67, 68], light-emitting diodes (LED) [105, 106, 107, 106], and X-ray detectors [108, 109] due to their excellent optoelectronic properties such as high absorption coefficient [6, 8] and long carrier diffusion length [13, 11, 110]. The power-conversion efficiency (PCE) of the single-junction halide perovskite solar cells (*n*-*i*-*p* type) has reached over 26% while that of perovskite/silicon monolithic tandem solar cells has reached 33.9% [111]. Nevertheless, the wide-bandgap perovskites that are of interest for integration into perovskite/silicon tandems still suffers from large open-circuit voltage (V_{OC}) loss, primarily due to nonradiative recombination in the bulk of the perovskite or at the perovskite/electron transport layer (ETL) [112, 113, 114, 115]. Fullerene (C_{60}) has been widely used as the ETL in inverted perovskite (p-i-n) solar cells, despite substantial nonradiative interfacial recombination at the perovskite/C_{60} interface, limiting V_{OC} and thus PCE [116, 117, 28, 118]. Engineering the perovskite surfaces and interfaces is an effective approach to reduce the nonradiative interfacial recombination at the perovskite/C_{60} interface and is crucial to the further development of tandem device performance [77, 119].

In this work, we study two organic salts - benzylammonium tosylate (BzAOTs) and benzylammonium triflate (BzAOTf) organic salts (Appendix C.1, C.4 and C.6) as interface modifiers between the perovskite and C_{60} layer that can reduce the nonradiative interfacial recombination in mixed-cation mixed-halide widegap perovskite solar cells (bandgap ~1.7 eV). The organic salts interlayers improve the V_{OC} and fill factor (FF) of perovskite solar cells. Notably, these organic salts with non-halide anions do not alter the bandgap of perovskite or significantly change the halide distribution throughout the surface to the bulk. We use density functional theory (DFT) to calculate the dipole moments for the OTs and OTf anions, which are 11.6 D and 4.4 D, respectively. We show that the two salts with different dipole moments modulate interfacial recombination differently. The BzAOTs interlayer improves the device performance through reducing the interfacial nonradiative recombination via control over surface field while BzAOTf decouples the perovskite film from C_{60} to reduce contact-induced recombination at the interface. We study the relationship between device performance, structural properties, surface/interface energy, and charge-carrier recombination at the interface with and without the benzylammonium sulfonate salts to elucidate their effects.

4.3 Results and discussion

Figure 4.1a shows the p-i-n device configuration with Me-4PACz as the hole transport layer (HTL), C_{60} as ETL and silver (Ag) as the top electrode. We choose a mixed-cation mixed-halide perovskite $FA_{0.83}Cs_{0.17}Pb(I_{0.75}Br_{0.25})_3$ (denoted as Cs17Br25) with a bandgap of $\sim$1.70 eV as the absorber, which is a potential top cell for perovskite/silicon tandems [112, 58, 120]. Figure 4.1b, c and d show the representative current density – voltage (J-V) scans of control, BzAOTs-treated and BzAOTf-treated devices under forward and reverse scans with device performance summarized in the insets. The control device has a PCE of 17.5%, V_{OC} of 1.15 V, short-circuit current density (J_{SC}) of 20.5 mA/cm^2 and fill factor (FF) of 74% based on reverse scan with the device exhibiting a mild hysteresis. With BzAOTs and BzAOTf-treated devices, the V_{OC} increases to 1.20 V and FF enhances to 79.9%. The PCE for both BzAOTs and BzAOTf-treated devices increases to 19.6% with similar J_{SC} to the control device based on reverse scan. The BzAOTf-treated device shows negligible hysteresis while the BzAOTs-treated device shows larger hysteresis than the control device (Figure C.7). Figure C.8 shows the statistical distribution of the device performance based on reverse scan with details summarized in Table C.1. The control device has an average V_{OC} of 1.14 V and PCE of 15.78%. Devices incorporating the BzAOTs had an average PCE of 17.61% and V_{OC} of 1.180 V, an increase of $\sim$40 meV compared to the control. The BzAOTf-treated devices had an average PCE of 17.58% and V_{OC} of 1.175 V, an increase of $\sim$35 meV relative to the control.

Figure 4.2a and b show the X-ray diffraction (XRD) patterns of the control perovskite film (with and without IPA washing) and BzAOTf- and BzAOTs-treated perovskite films.

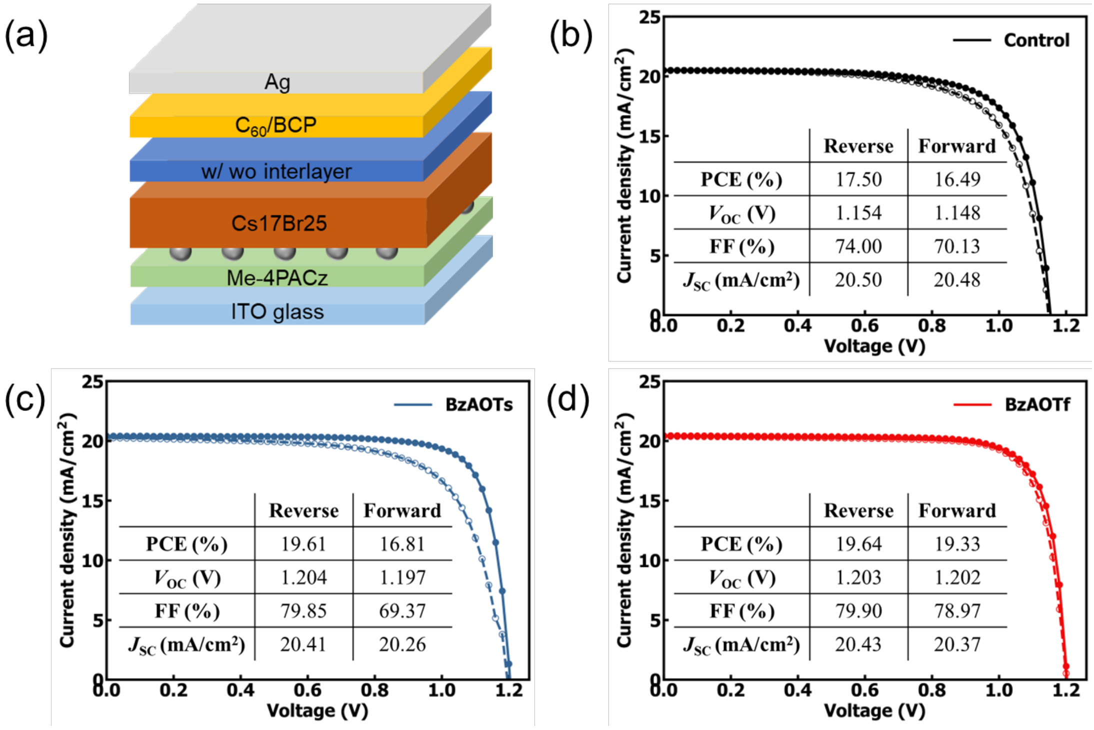

(b)

	Reverse	Forward
PCE (%)	17.50	16.49
V_{OC} (V)	1.154	1.148
FF (%)	74.00	70.13
J_{SC} (mA/cm^2)	20.50	20.48

(c)

	Reverse	Forward
PCE (%)	19.61	16.81
V_{OC} (V)	1.204	1.197
FF (%)	79.85	69.37
J_{SC} (mA/cm^2)	20.41	20.26

(d)

	Reverse	Forward
PCE (%)	19.64	19.33
V_{OC} (V)	1.203	1.202
FF (%)	79.90	78.97
J_{SC} (mA/cm^2)	20.43	20.37

Figure 4.1: (a) Device configuration. Spheres represent a dilute layer of aluminum oxide nanoparticles which improve the wettability of perovskite solution on Me-4PACz. BCP is short for bathocuproine. J-V scans of representative (b) control devices with IPA treatment, (c) BzAOTs-treated device and (d) BzAOTf-treated device. The insets in (b), (c) and (d) are corresponding deviceperformance parameters extracted from J-Vscans. The solid lines with filled symbols are the reverse scans and dashed lines with open symbols represent the forward scans.

With BzAOTs and BzAOTf surface treatment, there are two additional diffraction peaks at low angles, which are consistent with the diffraction peaks of BzAOTs, BzAOTf powders (Figure 4.2b). We further fabricated two-dimensional (2D) perovskite with benzyl ammonium iodide and lead iodide (denoted as BzA_2PbI_4). The diffraction peak of BzA_2PbI_4 at low angles falls in between of the two new peaks, excluding the formation of a detectable quantities of a 2D perovskite phase as result of benzylammonium cation in the two salts [86]. In addition, the surface treatment does not change the bulk properties of perovskite films becasue UV-Vis absorption spectra show negligible difference between the treated and untreated perovskite films (Figure C.10). As both BzAOTs and BzAOTf salts are deposited from anhydrous isopropanol (IPA), we use anhydrous IPA solvent as a treatment exclude the impact of IPA on perovskite morphology. As shown in Figure 4.2d, the perovskite film shows no change unpon IPA solvent washing, which indicates that the solvent has no influence on the morphology of the perovskite. However, with the addition of BzAOTs and BzAOTf, the grain boundaries of the perovskite films showed different features (Figure 4.2e and f), with the grain boundaries 'open-up', indicating that both molecules may infiltrate both grain boundaries, as well as be present at top perovskite surfaces.

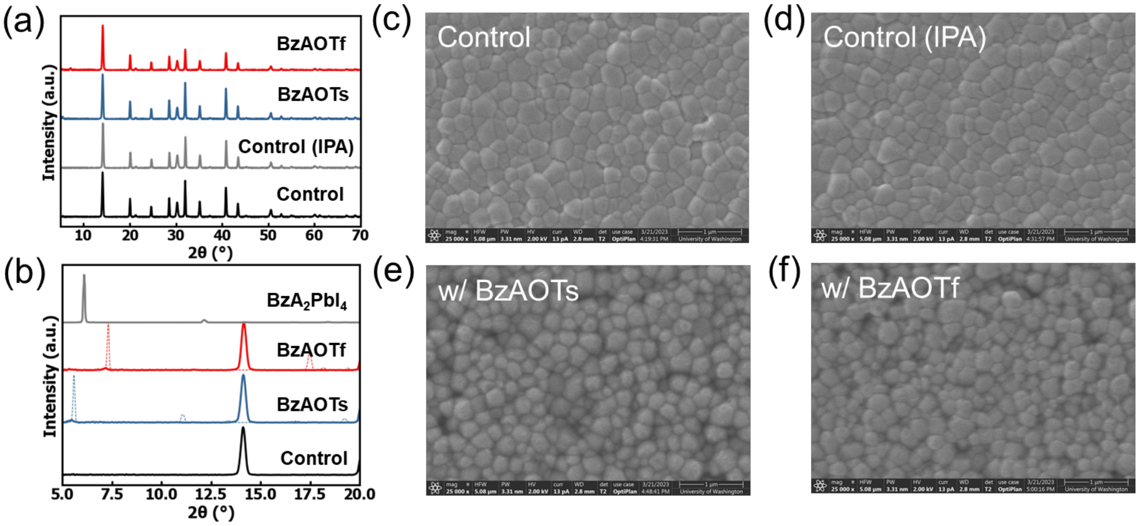

Figure 4.2: (a) XRD patterns of perovskite films on ITO/Me-4PACz with and without surface treatment. (b) zoomed-in XRD patterns with 2θ in the range of 5° to 20°. The dashed lines in (b) represent the patterns of BzAOTs and BzAOTf molecules measured in Si substrates. Top-view SEM images of (c) bare perovskite films, (d) IPA solvent-treated perovskite film, (e) BzAOTs-treated perovskite film and (f) BzAOTf-treated perovskite film.

Figure 4.3 compares the X-ray photoelectron spectroscopy (XPS) spectra of the control perovskite film, and BzAOTs- and BzAOTf-treated perovskite films. Figure 4.3a shows the carbon 1s spectra, where we observe that the C-C spectra integrated area percentage at 285.0 eV increased to 89.23% and 64.24% after BzAOTs and BzAOTf treatment as compared to that of 49.23% for the control perovskite film. The more pronounced peak intensity indicates both BzAOTs and BzAOTf molecules were deposited on perovskite surface. The peak at ~292.7 eV can be ascribed to the signal of C-F of BzAOTf molecule [121] and the sulfur signals from BzAOTs and BzAOTf treated perovskite films, further confirming that both organic salts have been successfully deposited on the perovskite (Figure C.8c). The weak peak at ∼291.6 eV in the C 1s spectra of the BzAOTs and BzAOTf-treated perovskite films likely results from the phenyl group in the BzAOTs and BzAOTf cation part [122]. Figure 5c and d show the depth-dependent time of flight secondary ion mass spectrometry (ToF-SIMS) for iodide and sulfonate ions while data showing cation distribution are shown in Figure C.11. We find that both cation and anion are mostly present at the top surface of perovskite film with some extending into the bulk of perovskite film, likely through grain boundaries (Figure C.11), consistent with a surface-limited treatment.

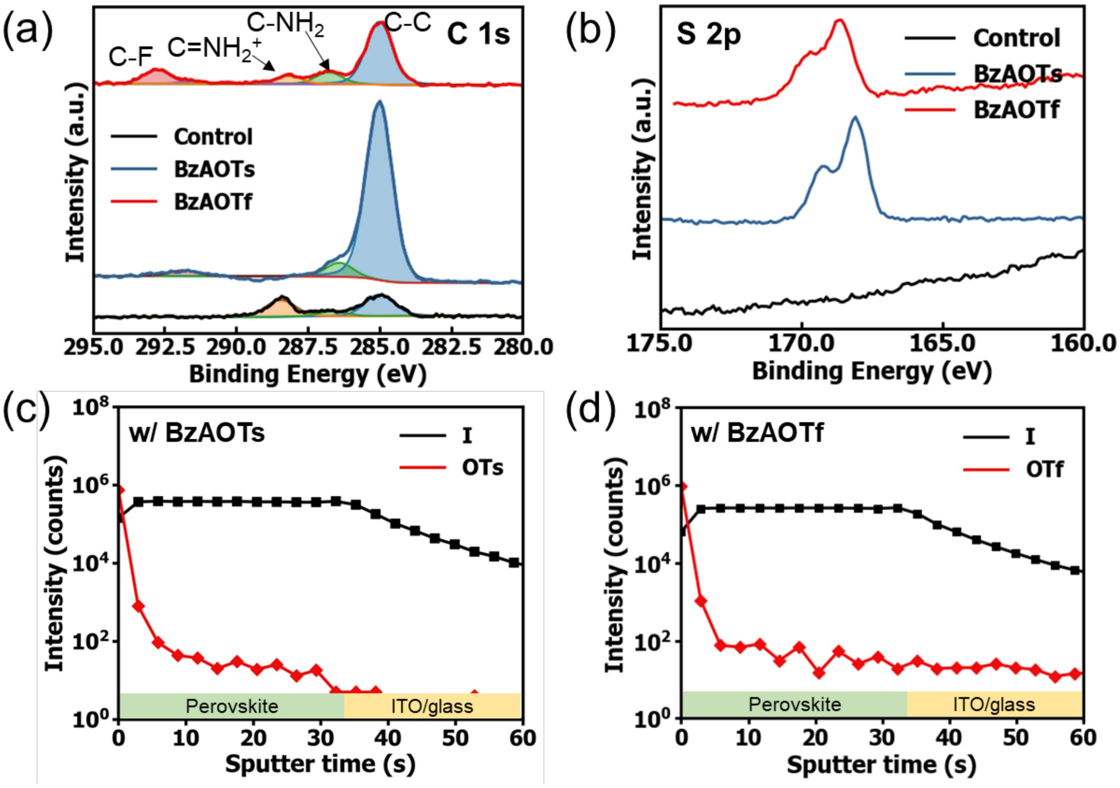

Figure 4.3: XPS spectra of (a) C 1s peak and (b) S 2p core level obtained from pristine perovskite films and BzAOTs-, BzAOTf-treated perovskite films. Depth-dependent ToF-SIMS showing (c) OTs and (d) OTf anions profiles.

Figure C.12 shows the surface potential of perovskite film with BzAOTs and BzAOTf surface treatment measured by scanning Kelvin probe microscopy (SKPM). With BzAOTs treatment, the surface potential of the perovskite changed by ~700 meV on average (Figure C.12b). However, the BzAOTf molecule does not change the surface potential (Figure C.10c) compared to the control perovskite film (Figure C.12a). We further calculated the work function of the perovskite film to be ~4.92 eV for control perovskite, ~4.20 eV for BzAOTs-treated perovskite film and ~4.87 eV for BzAOTf-treated perovskite (Figure C.12d) by referencing to the work function of highly ordered pyrolytic graphite (HOPG). The decreased work function of the perovskite film with BzAOTs treatment is likely due to dipolar layer of BzAOTs anion interacting with Pb^{2+} at the perovskite top surface.

Figure 4.4a and b shows TRPL decays of perovskite films on glass substrates without and with C_{60} layers in the presence of BzAOTf and BzAOTs molecules excited from the film side at 640 nm. We measured a similar PL lifetime for the control perovskite and BzAOTs-, BzAOTf-treated perovskite films. Stretched-exponential fits to the PL data reveal PL lifetime of ~250 ns for the control and ~310 ns for the treated perovskite films, indicating that BzAOTs and BzAOTf salts are limited in their capability to passivate the perovskite surface. However, after deposition of C_{60}, the control film has a much faster lifetime (~26 ns) than the BzAOTs- (132 ns) and BzAOTf-treated (45 ns) perovskite films, indicating that the BzAOTs and BzAOTf treatments reduces the nonradiative recombination at the perovskite/C_{60} interface [123]. Notably, BzAOTs has a much slower PL decay (~132 ns) in the presence of C_{60} layer, which we speculate could be due to a change in band bending and energy alignement from the high-dipole surface layer. The resulting surface field induced by OTs anion would repel carriers from the interface and would spatially separate the photogenerated electrons and holes, leading to slower recombination [12]. In Figure C.13, we illustrate the electronic band structure at the perovskite/C_{60} interface in the case of perovskite/C_{60}, perovskite/BzAOTf/C_{60}, and perovskite/BzAOTs/C_{60} based on our SKPM measurements. In Table C.2, we include a survey of interfacial energetics reported in the literature for various perovskite/C_{60} systems. The band-bending at the perovskite/C_{60} interface has magnitude, $\Delta E_F = E_{F,pvk}$- $E_{F,C_{60}}$, where $E_{F,pvk}$ and $E_{F,C_{60}}$ are the isolated Fermi energies in the perovskite and C_{60} layers respectively. For the control perovskite, $E_{F,pvk} < E_{F,C_{60}}$, resulting in downward band-bending as reported elsewhere

[116]. After applying BzAOTf as an interlayer, the $E_{F,pvk}$ is slightly increased by ∼0.03 eV, which serves to reduce the magnitude of the band-bending at the perovskite/C$_{60}$ interface (Figure C.13). When we apply BzAOTs as an interlayer, $E_{F,pvk}$ increases by ∼0.7 eV such that $E_{F,pvk} > E_{F,C_{60}}$, which most likely results in a reversal of the band-bending (Scheme 1c). Therefore, in the absence of an external bias, there is a significant change in band bending at the perovskite and C$_{60}$ interface, which leads to slower recombination. Figure 4.4b and d show the steady-state PL spectra of perovskite films excited with a wavelength of 640 nm from the perovskite film side. We measure similar PL emission intensity for control, BzAOTs- and BzAOTf- treated perovskite films, which was found to be similar in all cases, consistent with the TRPL measurements (Figure 4.4a). We then deposit a 30 nm C$_{60}$ film/layer on top of the perovskite films. After deposition of a 30 nm C$_{60}$ layer on top of the control perovskite films, the PL emission intensity of the control film with C$_{60}$ was quenched more than 10-fold. With the presence of BzAOTs and BzAOTf interlayers between perovskite and C$_{60}$, the PL emission intensities are less quenched (Figure 4.4d). The integrated intensities of PL emission for BzAOTs- and BzAOTf-treated perovskite films in contact with C$_{60}$ are 7.6-times and 4.8-times higher than that of the control perovskite film directly in contact with C$_{60}$. The suppressed PL quenching with the presence of BzAOTs and BzAOTf interlayers is consistent with both the TRPL measurement and V_{OC} from device measurement, indicating that BzAOTs and BzAOTf interlayers can effectively suppress nonradiative interfacial recombination. The BzAOTs-treated perovskite with C$_{60}$ shows slightly higher PL emission than BzAOTf-treated perovskite films, consistent with the statistically higher V_{OC} in the BzAOTf-treated devices.

4.4 Conclusions

We use BzAOTf and BzAOTs organic salts as interlayers in the perovskite/C$_{60}$ interface and show that both BzAOTf and BzAOTs molecules can improve the device performance by suppressing the nonradiative recombination at the perovskite/C$_{60}$ interface. The BzAOTs interlayer does this by altering the surface feild at the perovskite/C$_{60}$ interface, thus reducing the extent of nonradiative recombination. BzAOTf, on the other hand, improves device performance by decoupling the perovskite film from the detrimental interactions at the C$_{60}$

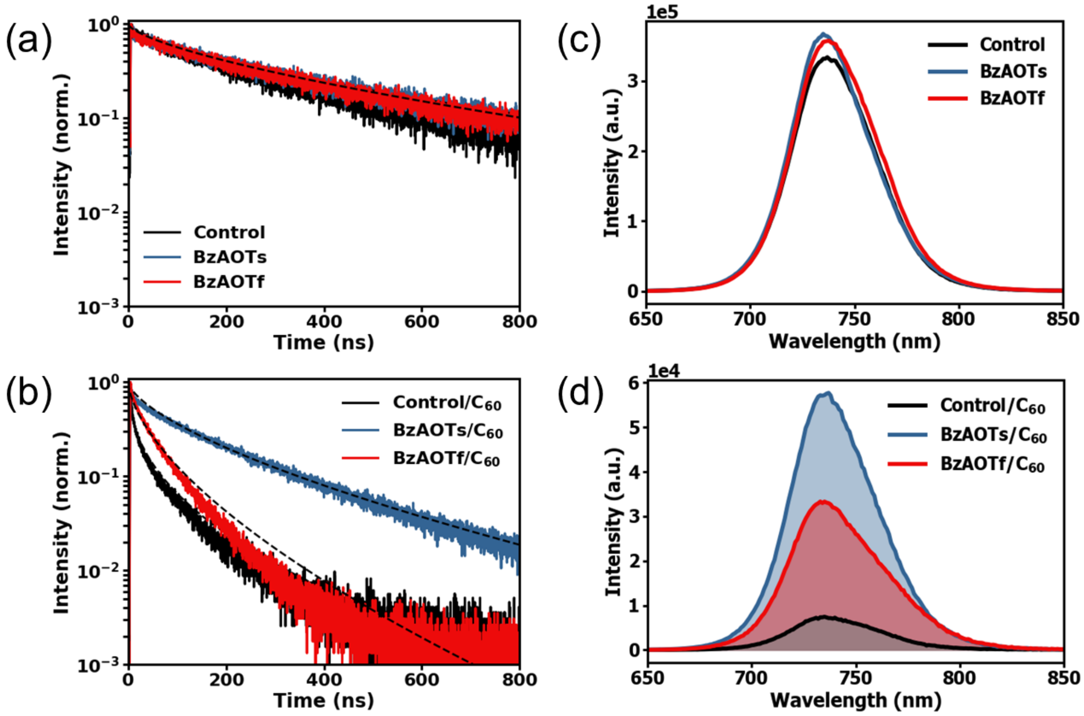

Figure 4.4: Time-resolved photoluminescence (TRPL) decays of perovskite films on glass (a) without and (b) with C_{60} on the perovskite films, excited with a 640 nm laser from the film side. Steady-state photoluminescence of perovskite films on glass (c) without and (d) with C_{60} layers, excited at 640 nm from the film side.

interface. ToF-SIMS and SEM revealed that both BzAOTs and BzAOTf predominantly are present at the top surface of the perovskite, with some penetration into the bulk along the grain boundaries. SKPM measurements showed that the OTs lowers the work function of the perovskite from 4.90 eV to 4.20 eV, while BzAOTf barely changes the work function of the perovskite film. The BzAOTs-treated device exhibited more hysteresis than the control device, while the BzAOTf-treated device showed negligible hysteresis. We believe the surface field can effectively suppress interfacial nonradiative recombination and improve device performance. Overall, we have shown that surface engineering can reduce the interfacial nonradiative recombination through surface field or decoupling the perovskite from the C_{60} layer. This work provides insights for designing strategies of interlayers for perovskite solar cells.

4.5 Acknowledgements

This work was primarily supported by the Office of Naval Research, Award number: N00014-20-1-2587. XRD, SEM , ToF-SIMS and XPS measurements were carried out at the Molecular Analysis Facility, a National Nanotechnology Coordinated Infrastructure site at the University of Washington which is supported in part by the National Science Foundation (awards NNCI-2025489, NNCI-1542101), the Molecular Engineering & Sciences Institute, and the Clean Energy Institute. PL measurements were performed in Molecular Engineering Materials Center, an NSF MRSEC (DMR-1719797). Part of this work was conducted with instrumentation supported by the University of Washington Student Technology Fee at the RTT. X. X. and S.D. acknowledge support from the U.S. Department of Energy's Office of Energy Efficiency and Renewable Energy (EERE) under the Solar Energy Technology Office Award Number DE-EE0008556 and by the NSF under MRSEC DMR-1719797 and MRSEC DMR-2308979. We would like to acknowledge the utilization of the Hyak supercomputer system at the University of Washington, supported through CEI, MEM-C, and the Student Technology Fund. Y.S acknowledges Dr. Samantha L. Young and Dr. Dan Graham for the measurements of XPS and ToF-SIMS. H.C. was supported by the National Science Foundation Graduate Research Fellowship under Grant No. DGE-2140004. D.S.G acknowledges salary and infrastructure support from the Washington Research Foundation, and the B. Seymour Rabinovitch Endowment.

Appendix A

SUPPLEMENTARY INFORMATION FOR CHAPTER 2

A.1 Experimental Section

Films for Crosslinking and Contact Angle Measurements. To prepare films of NDI-CL, NDI-CL was dissolved in anhydrous chlorobenzene (10 mg/mL). 100 µL of the resultant solution was deposited statically and spin coated at 1000 rpm for 60 s atop 1 in x 1 in O_3 cleaned glass substrates (ITO substrates in the case of CA measurements). The films were annealed for 10 min at 100 °C. The films were crosslinked using an Analytik-Jena compact UV lamp (UVGL-25) at 365 nm for 20 min.

Solar Cell Characterization. Current-voltage (J-V) characteristics under 1 Sun equivalent illumination were measured using an ORIEL LSH-7320 ABA LED solar simulator in a nitrogen-filled glovebox, which is calibrated with a filtered KG3 Silicon reference solar cell certified by NREL. The effective area of the solar cell is 0.0453 cm^2. J-V scans were carried out with a Keithley 2400 controlled by a program written in LabView. The voltage values are scanned at a 0.02 V step in the range of -0.1 V to 1.2 V. The steady-state power output was carried out by measuring the solar cells at maximum power point (MMP) and 1 Sun intensity. The shunt resistances of perovskite solar cells were estimated by following the Lee et al work [63], using the lumped equivalent circuit model and differentiating the J-V curve to obtain the shunt resistance at short-circuit current.

Drift Diffusion Simulations by SCAPS. The effect of cathode work function on device performance was studied by simulations with a device structure of ITO/Perovskite/Spiro-OMeTAD/Au shown in Figure A.12. We varied the work function of cathode from 4.01 eV to 4.51 eV with a step size of 0.1 eV. The surface recombination velocity at both electrodes was fixed at 1000 cm/s. The simulation parameters for perovskite were adopted from Jariwala et al. [57] except that the thickness of perovskite layer was set at 500 nm.[28] The parameters of Spiro-OMeTAD were adopted from Bouazizi et al [124].

UV-vis Absorption Spectroscopy. UV-vis absorbance spectra of the perovskite films were measured on an Agilent 8453 UV-Vis Spectrometer with wavelength in the range of 200-1100 nm. UV-vis absorbance spectra of the polymers were measured on a Cary 5000 UV-Vis-NIR Spectrophotometer.

Atomic Force Microscopy (AFM). The AFM images were collected using an Asylum Research MFP3D mounted on an inverted optical microscope with a 75 kHz tip.

Scanning Kelvin probe microscopy (SKPM). The SKPM images of NDI polymer-modified ITO substrates were measured with an Asylum Research MFP3D mounted on an inverted optical microscope by using 325 kHz tip under dark.

Time-resolved photoluminescence (TRPL). TRPL was measured by using a PicoQuant Picoharp 300 TCSPC system equipped with a 640 nm pulsed diode laser. The laser was pulsed at repetition rates of 1 MHz, excited from ITO side. The PL emission was filtered using a 700 nm long-pass filter before being directed to the detector. The PL lifetime was fitted by using a stretched exponential decay function as shown in previous work [58].

Cyclic Voltammetry. Electrochemical measurements were carried out in dry deoxygenated dichloromethane solutions of 0.1 M in tetra-n-butylammonium hexafluorophosphate using a BAS 100 B/W Potentiostat, a glassy carbon working electrode, a platinum auxiliary electrode, and, as a pseudo-reference electrode, a silver wire anodized in 1 M aqueous potassium chloride. Potentials were referenced to ferrocenium / ferrocene by using ferrocene as an internal reference. Cyclic voltammograms were recorded at a scan rate of 100 mVs^{-1}.

Contact Angle Goniometry. Measurements were conducted on a ramé-hart goniometer, using water and diiodomethane as probe liquids (0.2 µL). A drop (typically two repetitions at different spots on the substrate) was quickly placed on the surface, the needle was pulled back, and the drop shape was captured immediately with the camera. Measurements were collected in triplicate for each drop at an interval of 20 s. Images were analyzed with drop shape analysis software to determine the contact angle by the method most suitable for each given drop, usually height-width, and the results were averaged. The error bars displayed are the calculated uncertainty based on the standard deviation. The displayed images in Figure S13 are at t0.

Thermogravimetric Analysis (TGA). Measurement was performed on a Mettler Toledo TGA 2 over 30-800 °C, at 20.00 °C/min, and with a N_2 flow rate of 20.0 mL/min.

Differential Scanning Calorimetry (DSC). Measurement was performed on TA Instruments Q200 Differential Scanning Calorimeter (DSC) with a ramp rate of 10.00 °C/min.

A.2 Materials

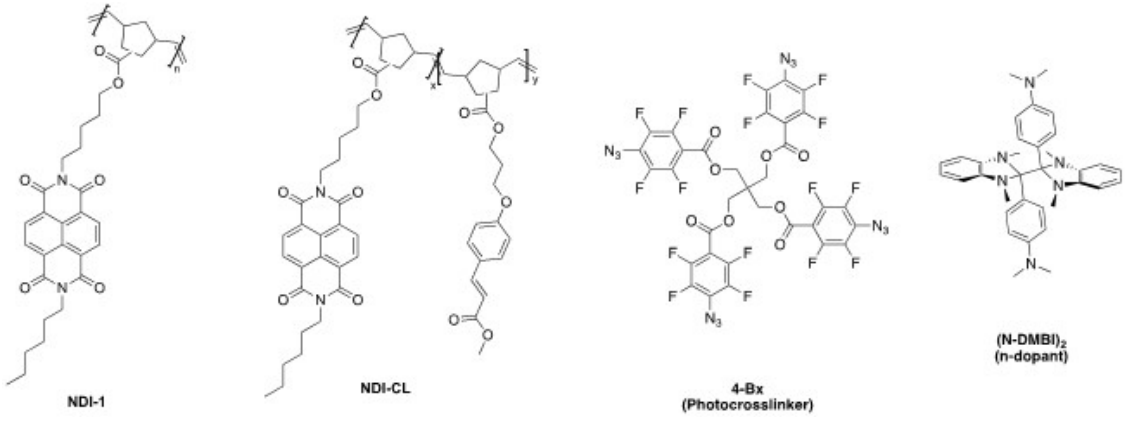

Figure A.1: Structures of organic materials used in this study

Synthesis

The NDI monomer, the polymer NDI-1, and cinnamate alcohol were synthesized according to previously reported literature procedures.[49, 125] $(N\text{-DMBI})_2$ and 4-Bx were also synthesized according to previously reported procedures.[50, 51]

Cinnamate Monomer

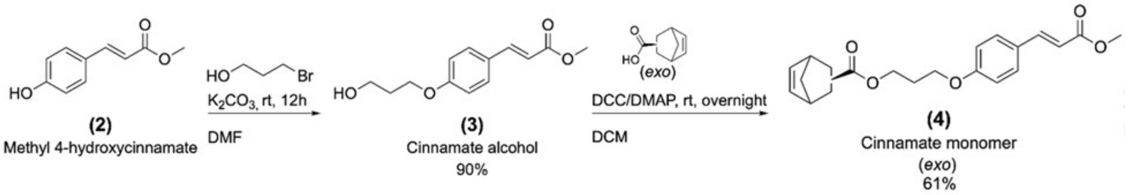

Figure A.2: Synthesis of cinnamate monomer.

3-(4-((E)-3-methoxy-3-oxoprop-1-en-1-yl)phenoxy)propyl-bicyclo[2.2.1]hept-5-ene-2- carboxylate, Cinnamate monomer, was synthesized via a Steglich esterification at room temperature. 1.00 g (4.23 mmol) of cinnamate alcohol and 0.76 g (5.50 mmol) exo-5-norbornene2-carboxylic acid were added to an oven dried 50 mL two neck round-bottomed flask with a stirring bar. The flask was then fitted with a septum, then pumped and refilled with nitrogen 3 times. Then 15 mL of anhydrous dichloromethane (DCM) was added, and the mixture was stirred until dissolution. Then 1.75 g (8.46 mmol) of N,N'-Dicyclohexylcarbodiimide (DCC) and 0.036 g (0.296 mmol) of 4-dimethylaminopyridine (DMAP) were dissolved in 5 mL of anhydrous DCM. The resulting solution was added dropwise via syringe to the reaction mixture. The reaction was stirred overnight. The solvent was removed under reduced pressure and the resulting mixture was triturated with MeOH. The resulting solid was purified by flash chromatography (80:20 DCM:EA). The collected fractions were concentrated under reduced pressure. The resulting solid was re-crystallized from a mixture of DCM and methanol, filtered, and dried under high vacuum to collect a white solid product (0.917g, 61%). ^{1}H NMR (400 MHz, $CDCl_3$) δ 7.64 (d, J = 16.0 Hz, 1H), 7.51 – 7.42 (m, 2H), 6.94 – 6.85 (m, 2H), 6.31 (d, J = 16.0 Hz, 1H), 6.17 – 6.06 (m, 2H), 4.29 (t, J = 6.2 Hz, 2H), 4.09 (t, J = 6.2 Hz, 2H), 3.79 (s, 3H), 3.02 (ddd, J = 3.2, 1.6, 0.8 Hz, 1H), 2.91 (s, 1H), 2.27 – 2.18 (m, 1H), 2.14 (quintet, J = 6.2 Hz, 2H), 1.91 (dt, J = 11.9, 4.0 Hz, 1H), 1.50 (dt, J = 8.3, 1.6 Hz, 1H), 1.42 – 1.31 (m, 2H). ^{1}3C^{1}H NMR (101 MHz, $CDCl_3$) δ 176.35, 167.90, 160.71, 144.61, 138.23, 135.81, 129.87, 127.34, 115.46, 114.93, 64.68, 61.24, 51.73, 46.75, 46.48, 43.26, 41.75, 30.48, 28.75. HRMS (ESI) m/z calculated for $C_{21}H_{25}O_5$ $[(M+H)^+]$ 357.1697, found 357.1689. Anal. Calcd for $C_{21}H_{25}O_5$: C, 70.77; H, 6.79; N, 0. Found: C, 70.74; H, 6.65; N, 0.

poly-[(5-(7-hexyl-1,3,6,8-tetraoxo-3,6,7,8-tetrahydrobenzo[lmn][3,8]phenanthrolin-2(1H)- yl)pentyl norbornene-2-carboxylate)-ran-((E)-3-(4-(3-methoxy-3-oxoprop-1-en-1- yl)phenoxy)propyl norbornene-2-carboxylate)], Cinnamate copolymer, was synthesized via a ring opening polymerization (ROMP) with the so-called Grubbs I initiator. 0.50 g (0.90 mmol) of NDI monomer and 0.137 g (0.385 mmol) of cinnamate monomer were added to an oven dried round-bottomed flask equipped with a stirring bar. The flask was purged and refilled with nitrogen three times. The solids were dissolved in anhydrous

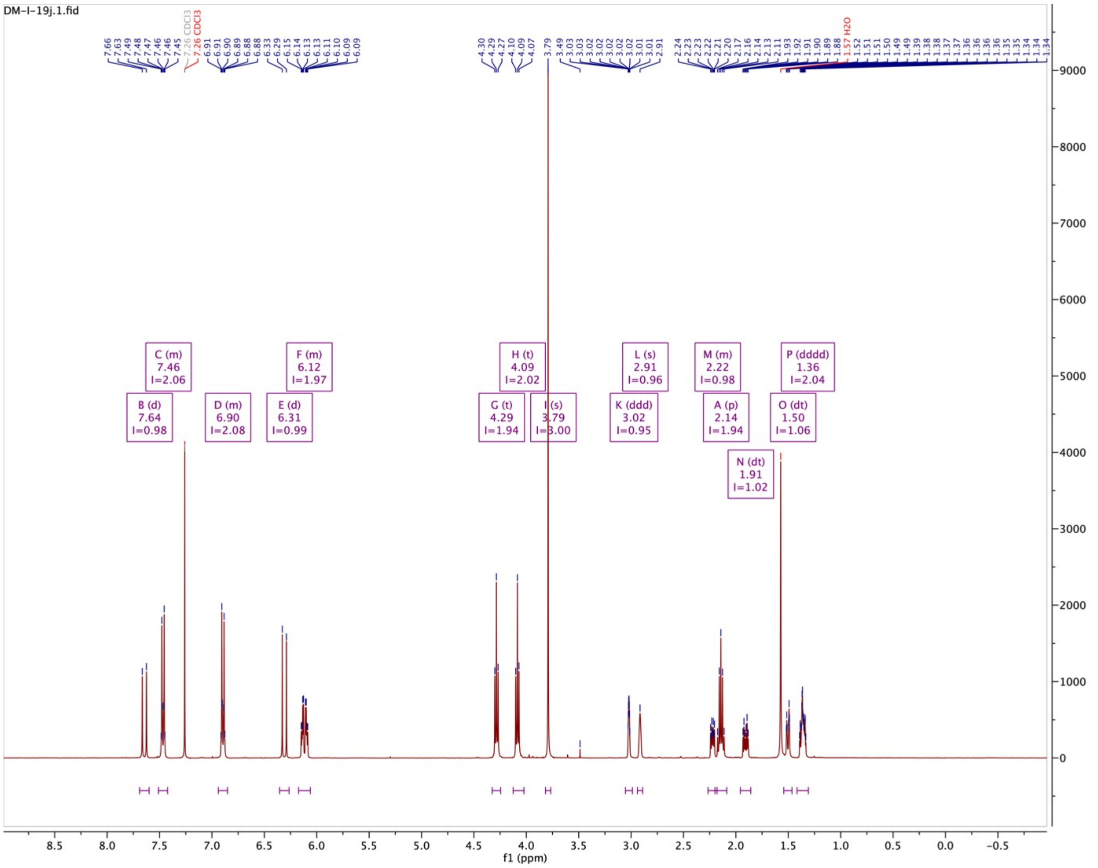

Figure A.3: ^{1}H-NMR spectrum of cinnamate monomer in $CDCl_3$.

DCM (7 mL) under nitrogen. "First generation" Grubbs initiator (10.5 mg, 0.0128 mmol) was added to a separate vial, purged and refilled with nitrogen three times, then dissolved in dichloromethane (1.0 mL). The resulting solution was added to the reaction mixture via syringe. The reaction mixture was stirred overnight. The reaction was quenched by the addition of excess ethyl vinyl ether. The resulting solid was dissolved in dichloromethane and precipitated in MeOH three times and subsequently was isolated by vacuum filtration as a yellow solid (0.542 g, 85%). 1H NMR (400 MHz, $CDCl_3$) δ 8.67 (s, 4H), 7.52 (s, 0H), 7.36 (s, 1H), 6.81 (s, 1H), 6.20 (s, 1H), 5.35 (s, 2H), 5.17 (s, 1H), 4.23 (s, 1H), 4.14 (s, 5H), 4.04 (s, 3H), 3.75 (d, J = 4.6 Hz, 1H), 3.06 (s, 0H), 2.94 (s, 0H), 2.67 (s, 2H), 2.50 (s, 3H), 2.11 – 2.04 (m, 2H), 1.92 (s, 2H), 1.75 – 1.67 (m, 8H), 1.58 (s, 3H), 1.49 – 1.37 (m, 5H),

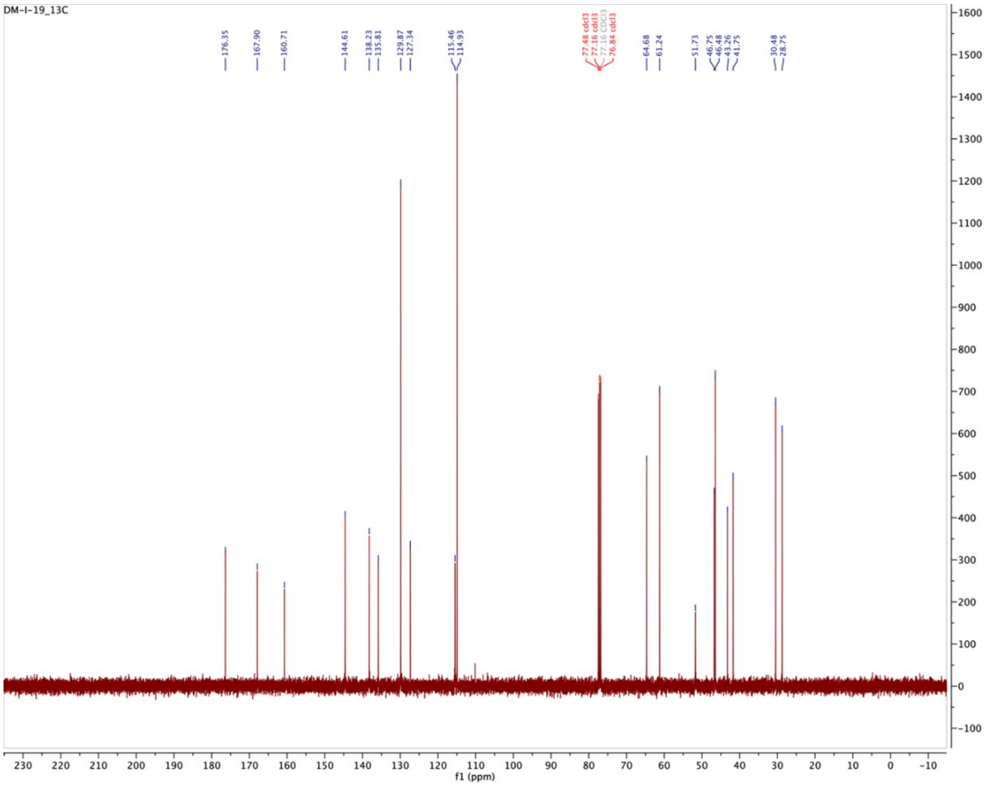

Figure A.4: $^{13}C^{1}$HNMR spectrum of cinnamate monomer in $CDCl_3$.

1.33 (d, J = 14.3 Hz, 1H), 1.33 (s, 3H), 1.16 (s, 1H), 0.92 – 0.84 (m, 3H). Anal. Calcd for $[C_{33}H_{36}N_2O_6]_{0.7}[C_{21}H_{25}O_5]_{0.3}$: C, 71.07; H, 6.60; N, 3.52. Found: C, 70.53; H, 6.72; N, 3.75. GPC analysis in $CHCl_3$: Mn = 45.4 kDa, $M_w/M_n = 1.17$.

Sample	PCE (%)	V_{OC} (V)	FF (%)	J_{SC} (mA/cm^2)	MPP (%)
NDI-1	13.31 ± 0.45	1.051 ± 0.005	58.77 ± 1.66	21.55 ± 0.19	10.33 ± 1.08
NDI-CL	15.10 ± 0.62	1.077 ± 0.003	64.43 ± 2.38	21.76 ± 0.28	12.28 ± 0.73

Table A.1: Photovoltaic figures of merit.

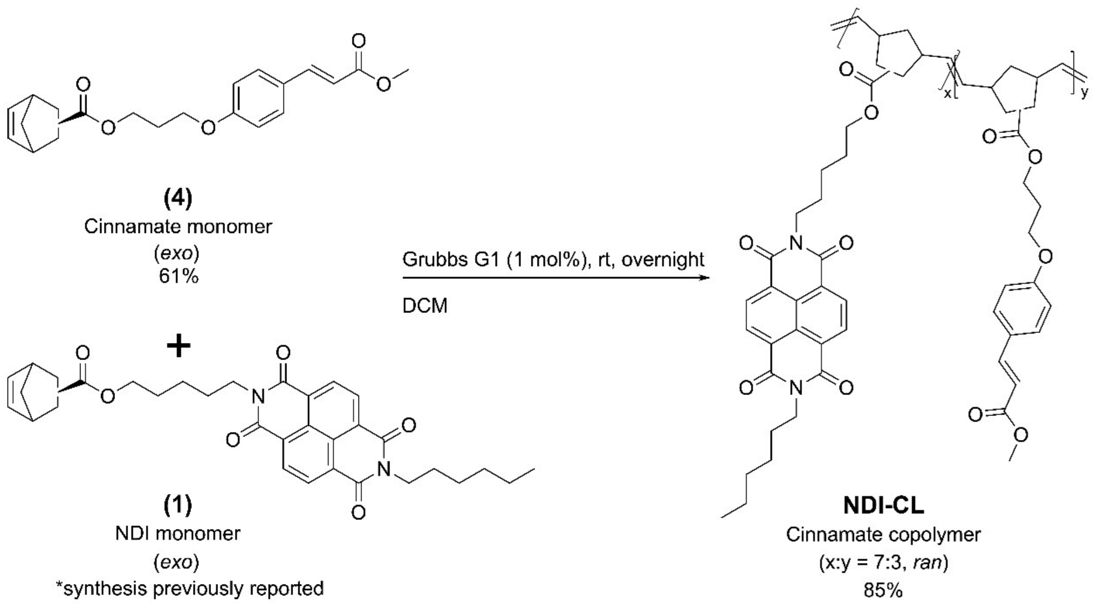

Figure A.5: Synthesis of cinnamate copolymer.

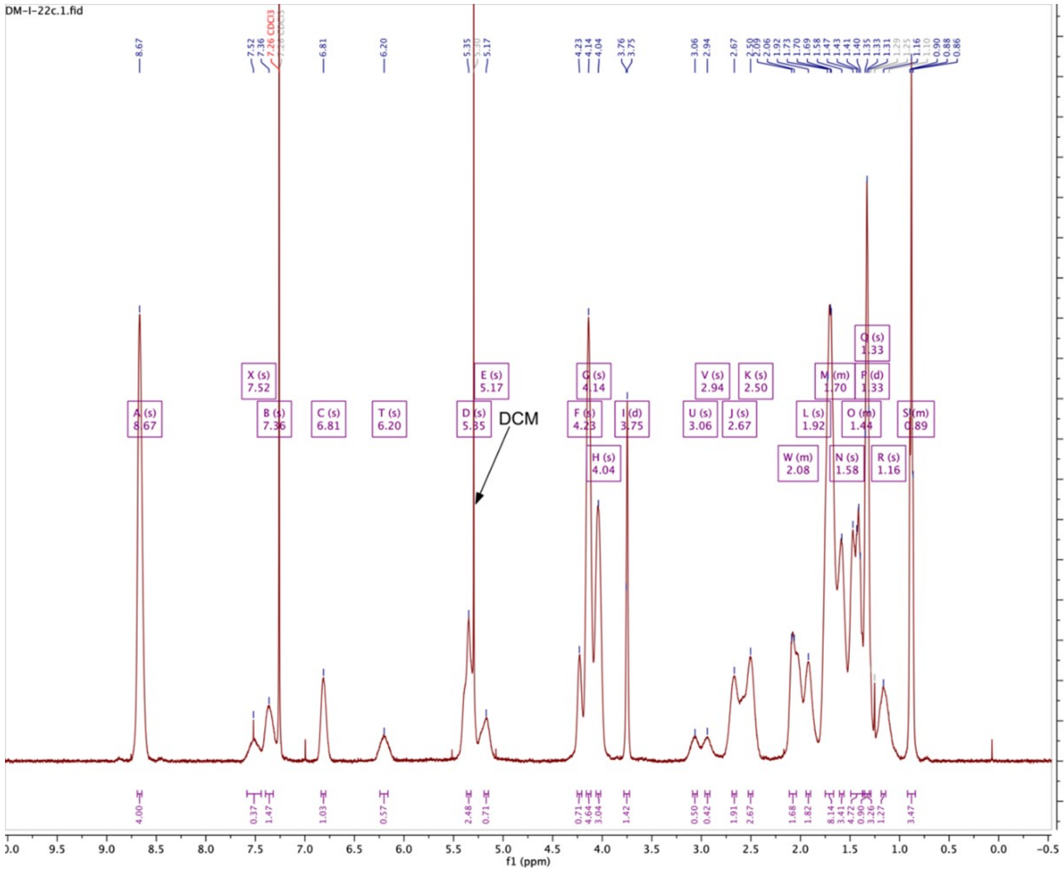

Figure A.6: ^{1}H-NMR spectrum of cinnamate copolymer in $CDCl_3$.

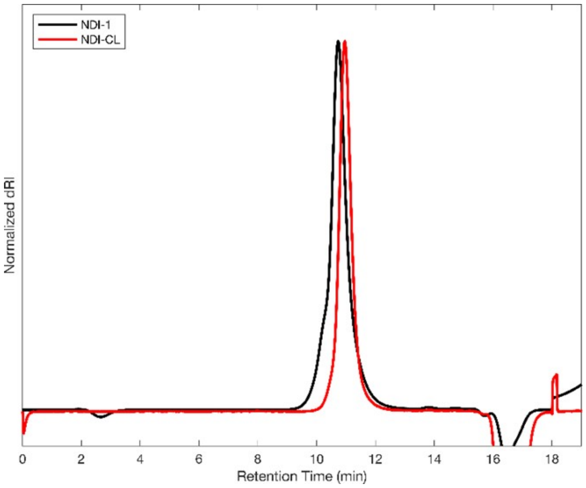

Figure A.7: SEC trace in chloroform of NDI-1 and NDI-CL. Homopolymer, NDI-1, is shown in black and copolymer, NDI-CL, is shown in red.

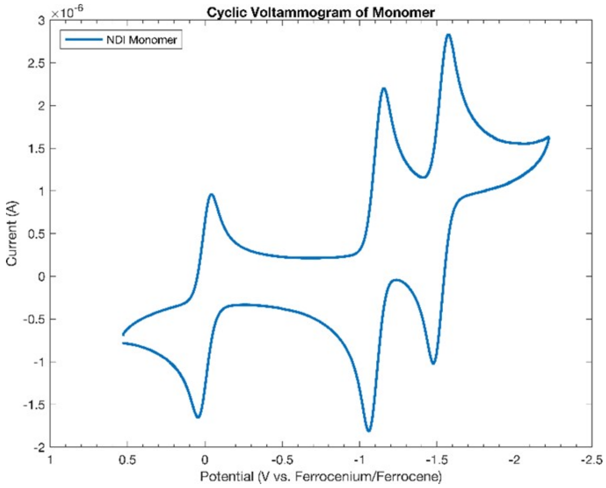

Figure A.8: Cyclic voltammogram of NDI monomer 0.1 M NBu4PF6 in DCM. Referenced to ferrocenium / ferrocene by using ferrocene as an internal reference. $E_{1/2}{}^{0/-} = 1.10$ V and $E_{1/2}{}^{-/2-} = 1.50$ V vs. $FeCp_2{}^{0/+}$.

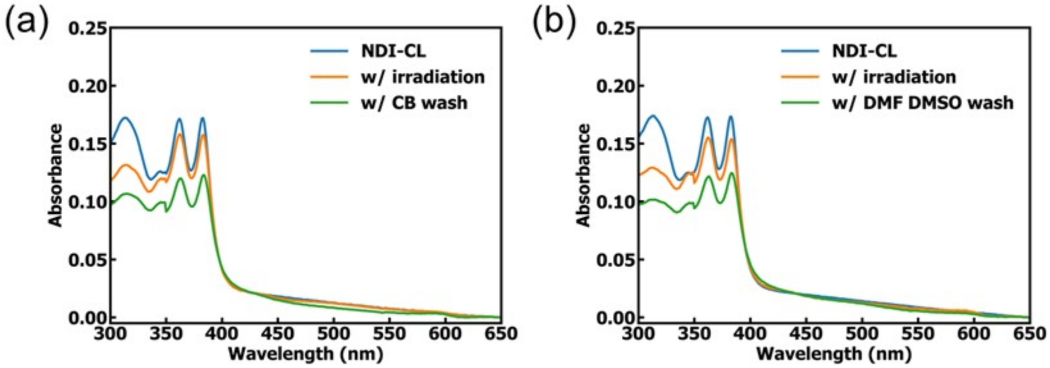

Figure A.9: (a) Solvent resistance of photo-crosslinked film towards polymer casting solvent, chlorobenzene (CB). (b) Solvent resistance of photo-crosslinked film towards perovskite casting solvent, volume ratio 4:1 of DMF:DMSO.

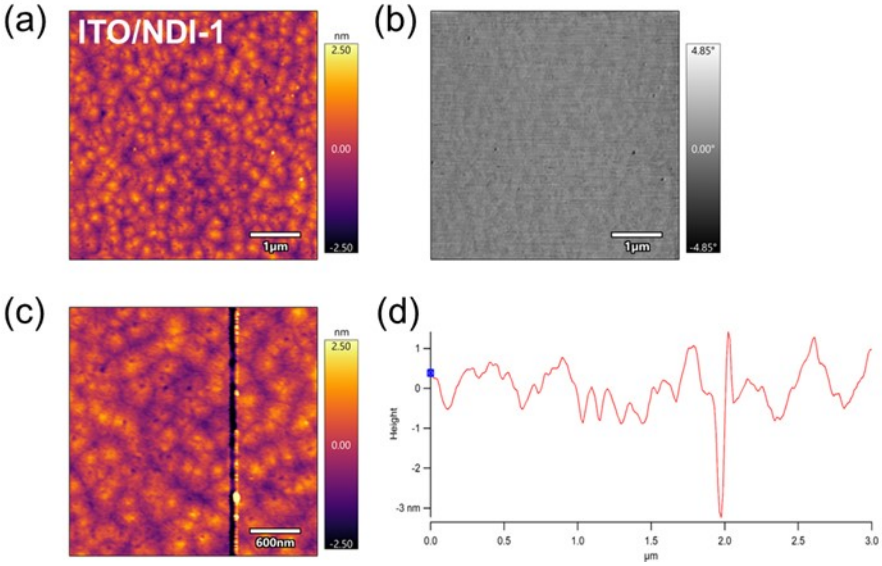

Figure A.10: AFM (a) topography and (b) phase images of NDI-1 film on ITO substate. (c) thickness of NDI-1. (d) the corresponding line profile.

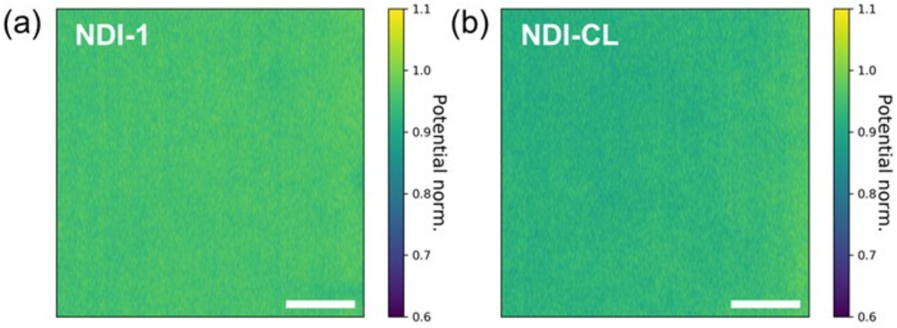

Figure A.11: SKPM surface potential images of (a) ITO, (b) NDI-1 and (c) NDI-CL modified ITOs. Scale bar in both images is 1 μm.

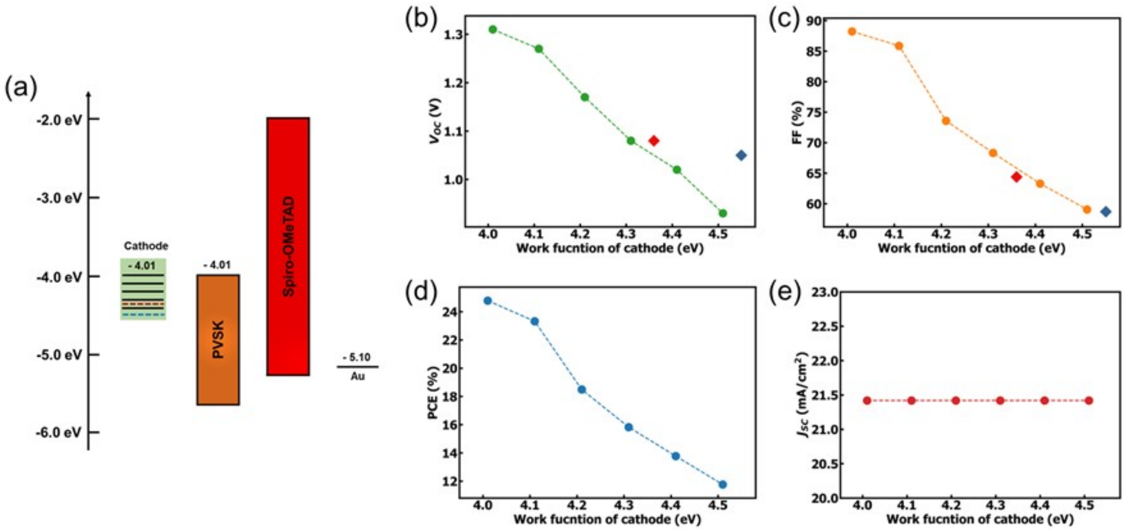

Figure A.12: Drift-diffusion simulation results performed by SCAPS. (a) Schematics of energy diagram used for simulations. The influence of the work function of cathode on the device performance: (b) V_{OC}, (c) PCE, (d) FF and (e) J_{SC}. The simulation parameters for the perovskite were adopted from previous work, and parameters of Spiro-OMeTAD are adopted from the literature.4 The blue and red dashed lines in (a) represent the measured work functions of NDI1/ITO and NDI-CL/ITO. The blue and red diamonds in (b) and (c) stand for average data points of solar cell devices made using the NDI-1 and NDI-CL.

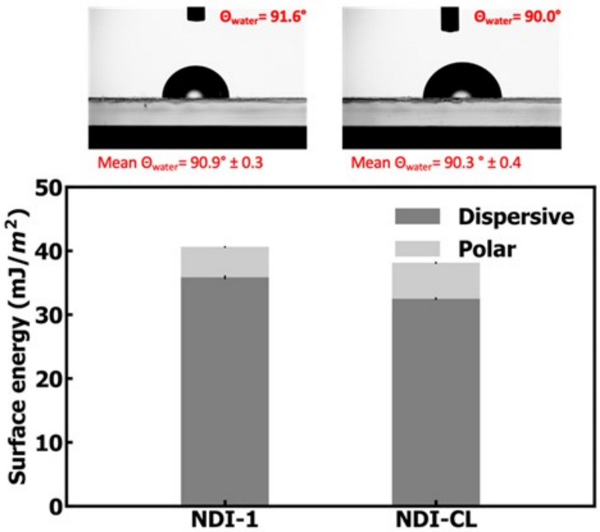

Figure A.13: Water contact angles of NDI polymers on O_3 cleaned ITO. Harmonic meandetermined surface energies (γ_s) broken into their polar $(\gamma s_s{}^{p})$ and dispersion $(\gamma_s{}^{d})$ components after O_3 cleaning of ITO and deposition of NDI polymers.

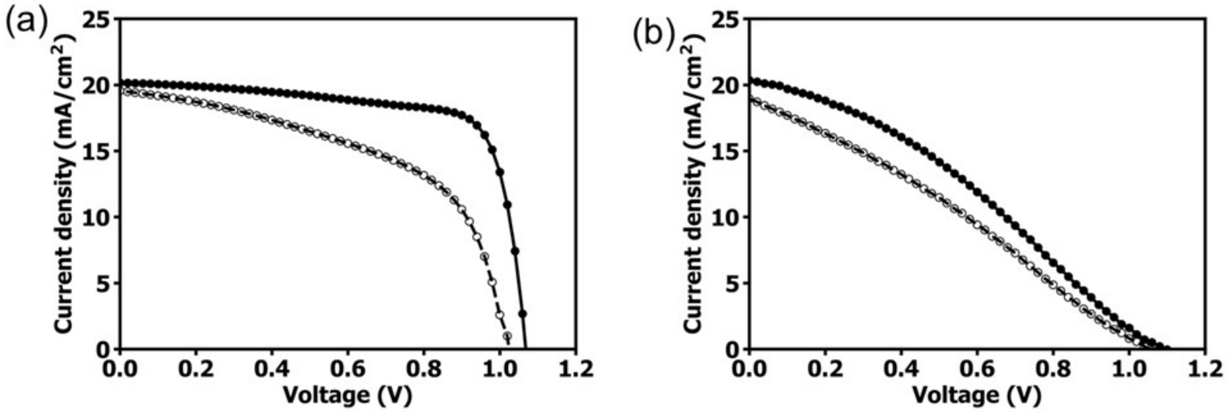

Figure A.14: *J*-*V* curves of device with (a) SnO_2 as ETL: ITO/SnO_2/Cs17Br15/Spiro-OMeTAD/Au and (b) without any ETLs: ITO/Cs17Br15/Spiro-OMeTAD/Au.

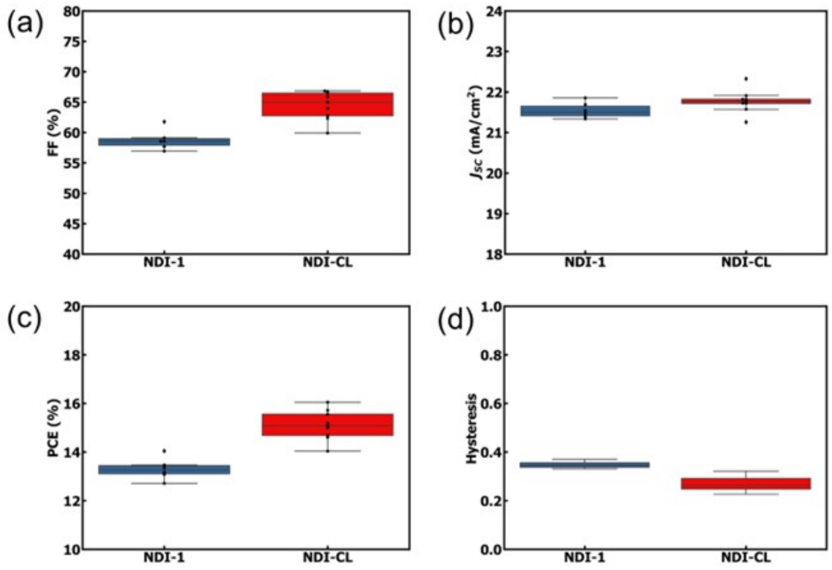

Figure A.15: Additional photovoltaic parameters. (a) Comparison of (a) FF, (b) J_{SC}, (c) PCE, and (d) hysteresis of NDI-1 and NDI-CL devices based on reverse scan.

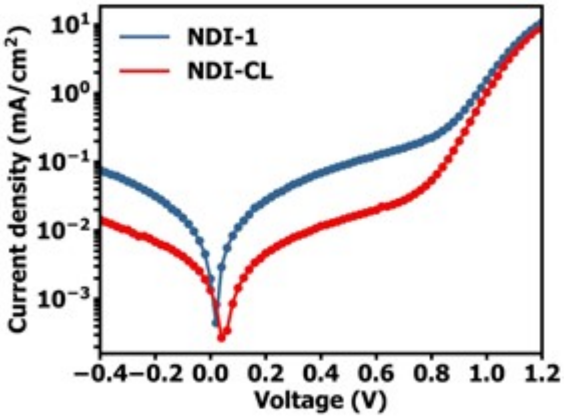

Figure A.16: Dark J-V curve of NDI-1 and NDI-Cl devices.

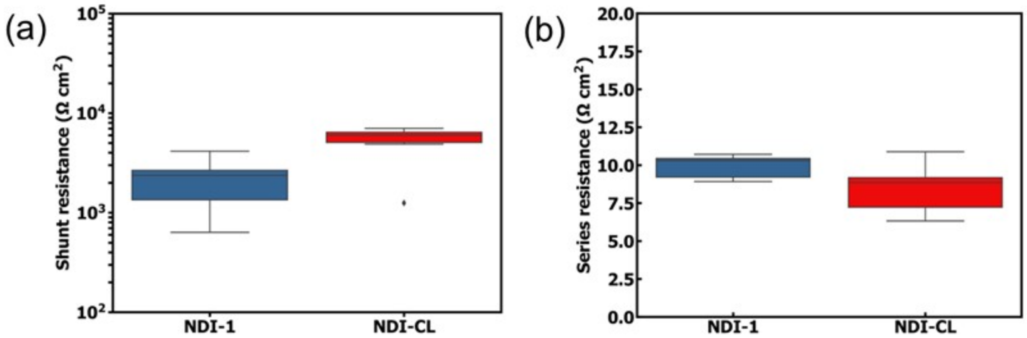

Figure A.17: The (a) shunt resistance and (b) series resistance of perovskite solar cell devices with NDI-1 and NDI-CL (based on reverse scan). The NDI-CL devices have higher shunt resistance than that of NDI-1 devices. In addition, we fit J-V curves to obtain a series resistance of 9.9 ± 0.8 $\Omega \cdot \mathrm{cm}^2$ for control device and 8.5 ± 1.8 $\Omega \cdot \mathrm{cm}^2$ for NDI-CL devise. Which shows that NDI-CL devices have slightly lower or similar series resistance in comparison to the NDI-1 devices.

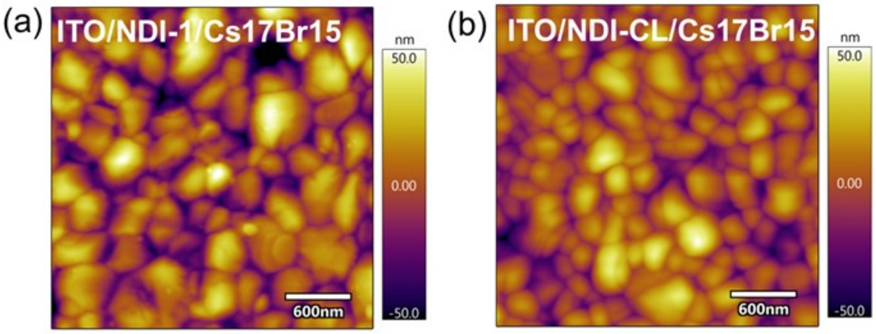

Figure A.18: AFM images of perovskite films on (a) NDI-1 and (b) NDI-CL.

Appendix B

SUPPLEMENTARY INFORMATION FOR CHAPTER 3

B.1 Materials and characterizations

All precursors were used without further purification and stored and mixed in a nitrogen-filled glovebox. Formamidinium iodide (FAI, Greatcell), Cesium iodide (CsI, Sigma), lead iodide (PbI_2, Sigma) and lead bromide ($PbBr_2$, Sigma) were dissolved in a mixture of anhydrous N,N-Dimethylformamide (DMF) and dimethyl sulfoxide (DMSO) (ratio of 4:1 v/v) to prepare a 1.2 M solution of $FA_{0.83}Cs_{0.17}Pb(I_{0.85}Br_{0.15})_3$ according to the stoichiometric. MeO-2PACzis from TCI. Patterned indium tin oxide (ITO, thin films) glass substrates and glass substrates were cleaned by sequentially sonicating in water containing ∼2% Micro-90 detergent, DI water, acetone, and isopropanol (IPA) for 10 mins, respectively, followed by plasma-cleaning for 5 minutes. The perovskite precursor solution was filtered with a PTFE filter before use and 50 µL of the solution was deposited on top of the substrate and spin-coated at 4000 rpm for 60 s. When ∼35 s remaining, 120 µL anhydrous chlorobenzene (CB) antisolvent was dropped from above. The perovskite films were then annealed at 100 °C for 30 s and 150 °C for 10 mins. The preparation of perovskite films was carried out in a nitrogen-filled glovebox.

Solar cell fabrication. To fabricate the Cs17Br15 devices described in the main text, a HTL solution (MeO-2PACz) was prepared with a concentration of 1 mmol/L in anhydrous ethanol.[83] 100 μL of the solution was put onto the ITO substate before spin-coating with 3000 rpm for 30 s. The substrates were then annealed at 100 °C for 10 mins. The perovskite films were deposited in the same as mentioned above [57]. APTMS surface passivation (5 min) was adopted from the reference [57]. After perovskite deposition and APTMS surface passivation, 30 nm C_{60} and 5 nm Bathocuproine (BCP) were thermally deposited onto the perovskite layer. For C_{60}, the deposition rate was from 0.2 Å/s for 5nm to 0.5 Å/s for the rest of the total 25 nm. The deposition rate for BCP was 0.2 Å/s. For completing the whole perovskite solar cell device, 100 nm Ag was thermally evaporated with an evaporation rate of 0.5 Å/s for the first 10 nm to 1 Å/s for the rest of the 90 nm.

Solar cell characterization. Current-voltage (J-V) characteristics under 1 Sun equivalent illumination were measured using a ORIEL LSH-7320 ABA LED solar simulator in a nitrogen-filled glovebox, which is calibrated with a filtered KG3 Silicon reference solar cell certified by NREL. The effective area of the solar cell is 0.0453 cm^2. J-V scans were carried out with a Keithley 2400 controlled by a program written in LabView. The voltage values are scanned at a 0.02 V step in the range of -0.1 V to 1.2 V. The steady-state power output was carried out by measuring the solar cells under the bias of the maximum power point (MMP) and 1 Sun intensity.

Surface passivation with APTMS. APTMS surface passivation of Cs17Br15 films and devices was carried out at room temperature in a vacuum oven (Precision Vacuum Oven Model 19) for 5 mins (or other times as indicated). 1 mL APTMS was put into a 4 mL vial with perovskite films around the vial (see Reference 2 for schematics). The films and vial were covered with a 500 mL glass jar inside of the chamber. The chamber was placed under vacuum by pumping down the chamber [57].

Photoluminescence (PL) and time-resolved photoluminescence (TRPL). PL and PL lifetime measurements are carried out by using Edinburgh FLS1000 spectrometer . PL is measured with a Xenon lamp light source with an excitation wavelength of 405 nm and the TRPL was acquired with EPL-405, a 405 nm picosecond pulsed diode laser. The repetition rate for the TRPL is 500 kHz that is controlled by an internal trigger input. The slits are the same for all the measurements. A PMT-980 detector is used for both PL and TRPL measurements. The TRPL fitting is referring to the references and surface recombination velocity (SRV) calculations are based on the following equations [57, 20]:

$$1/\tau_e = 1/\tau_b + 1/\tau_s$$

$$\tau_s = W/SRV + (4/D)(W/\pi)^2$$

The film thickness is determined to be ∼500 nm (W) as a concentration of 1.2 M perovskite precursor solution was used.

Photoluminescence quantum yield (PLQY) PLQY results were determined using a 532 nm continuous wave laser (CrystaLaser LC) as the excitation source to illuminate the samples in an integrating sphere (Hamamatsu photonics K.K). The beam intensity was fixed equal to 1 Sun intensity for Quasi-Fermi level slitting calculations. For the dimmer stacks, the PLQY was measured by using the PL emission under equivalent 1 Sun intensity, comparing with known PLQY, and then convert to its PLQY.

X-Ray Diffraction The Bruker D8 powder x-ray diffractometer with a high-efficiency Cu anode microfocus x-ray source and an extremely sensitive Pilatus 100K large-area 2D detector is used to investigate the crystal information of perovskite films before and after passivation.

UV-visible (UV-vis) absorption spectroscopy UV-vis absorbance spectra of the perovskite films are measured on an Agilent 8453 UV-Vis Spectrometer in a range of 200-1100 nm.

Passivation resistance to solvent, annealing and vacuum We conducted the experiment to investigate if the AMPTS passivation layer can survive the solvent treatment, annealing, and high vacuum because all those are all involved in the device fabrication processes. Figure 1(c) and Figure 1(d) show the results of PL lifetime and SRVs of the passivated films together with the chlorobenzene (CB), annealed at 100 °C for 3 mins and high vacuum treatment in the vacuum chamber of the evaporator (Figure S5). CB is a commonly used solvent for the deposition of electron transport layers such as PCBM for solution-processed perovskite solar cell devices. The 100 °C thermal treatment is designed to simulate the thermal annealing of ETL after solution deposition. Our results show that both CB and annealing treatments had a negligible effect on APTMS passivated perovskites with perovskite films still maintaining PL lifetime >1000 ns and a corresponding SRV ~50 cm/s (Figure 1(d)). To simulate the fabrication of thermally evaporated perovskite solar cells, requiring high-vacuum thermal evaporation of ETL or a top metal electrode onto APTMS, we examined the behavior of passivated solar cells exposed to high-vacuum thermal evaporation of ETL, or top metal electrode on APTMS passivation under high vacuum (10^{-7} Torr) for 20 minutes. Figure S5(a) shows the boxplot of PL lifetime of APTMS passivated films, and Figure S5(b) displays the corresponding SRV of APTMS-passivated

Cs17Br15 perovskite films under high vacuum. We found that high vacuum exposure at room temperature did not affect the APTMS passivation effect, with PL lifetime being ~1000 ns for APTMS and ~1100 ns for vacuum samples, and SRV being ~50 cm/s for APTMS and ~40 cm/s for vacuum samples. These results consistently corroborate the fact that APTMS passivation is suitable for both solution-processed and thermally evaporated perovskite solar cells.

Excitation Correlated Photoluminescence Spectroscopy (ECPL) For the ECPL measurement, 1030 nm, 220 fs pulses are generated in an ultrafast laser system at a 100 kHz repetition rate (PHAROS Model PH1-20-0200-02-10, Light Conversion). The laser beam is directed into a commercial optical parametric amplifier (ORPHEUS, Light Conversion) with a 2.64 eV pump excitation pulse selected. The excitation intensity is changed by moving a motorized filter wheel (FW212CNEB, Thorlabs). The pulse trains are then split 50/50 by a beam splitter cube, where one of the beams is directed to a motorized linear stage (LTS300, Thorlabs), so that the delay between the two pulses can be controlled. Each pulse is modulated with a chopper at the frequencies of 373 and 199 Hz, respectively. The pulses are then focused onto the perovskite sample with a 150 mm focal length lens. The emitted PL is filtered with a 550 nm long-pass filter to get rid of the pump, before focusing into a photoreceiver. The photoreceiver is connected to a lock-in amplifier (HF2LI, Zurich Instruments) where the total integrated PL and the nonlinear component ΔPL are obtained simultaneously by demodulating both at the fundamental and the sum frequency. For all measurements, data are acquired from the lowest to highest excitation fluence in the same spot.

Scanning probe microscopy (SPM)

AFM nanomechanical mapping The elastic modulus, and adhesion was collected using Bruker Dimension Icon in PeakForce quantitative nanomechanical mapping (QNM) mode with a SCANASYST-AIR tip ($k = 0.4$ N/m). The elastic modulus image was obtained by fitting with the Derjagin, Muller, Toropov (DMT) model. The modulus mapping was calibrated using the relative method where modulus maps was first obtained on a PDMS-SOFT calibration sample (2.5 MPa, Bruker) then the same parameters were used to determine the modulus of the perovskite/APTMS sample. Conductive AFM (cAFM) The conductive AFM maps were collected using an Asylum Research MFP3D mounted on an inverted optical microscope. All cAFM images were acquired with a gold-coated tip (Budget Sensors CONTGB-G, k $\approx$ 0.2 N/m, resonance frequency = $\sim$13 kHz) on a 2nA/V tip holder. The force setpoint was kept approximately constant in all images at approximately $\sim$4-5 nN. The sample was illuminated with a 488 nm laser (CrystaLaser) from the glass/ITO side, with the laser co-aligned with the cantilever and focused via a 40X 0.6 NA objective lens. The bias in all cAFM images is applied to the sample. All samples were loaded in a nitrogen glovebox and all cAFM images were acquired under active flowing nitrogen.

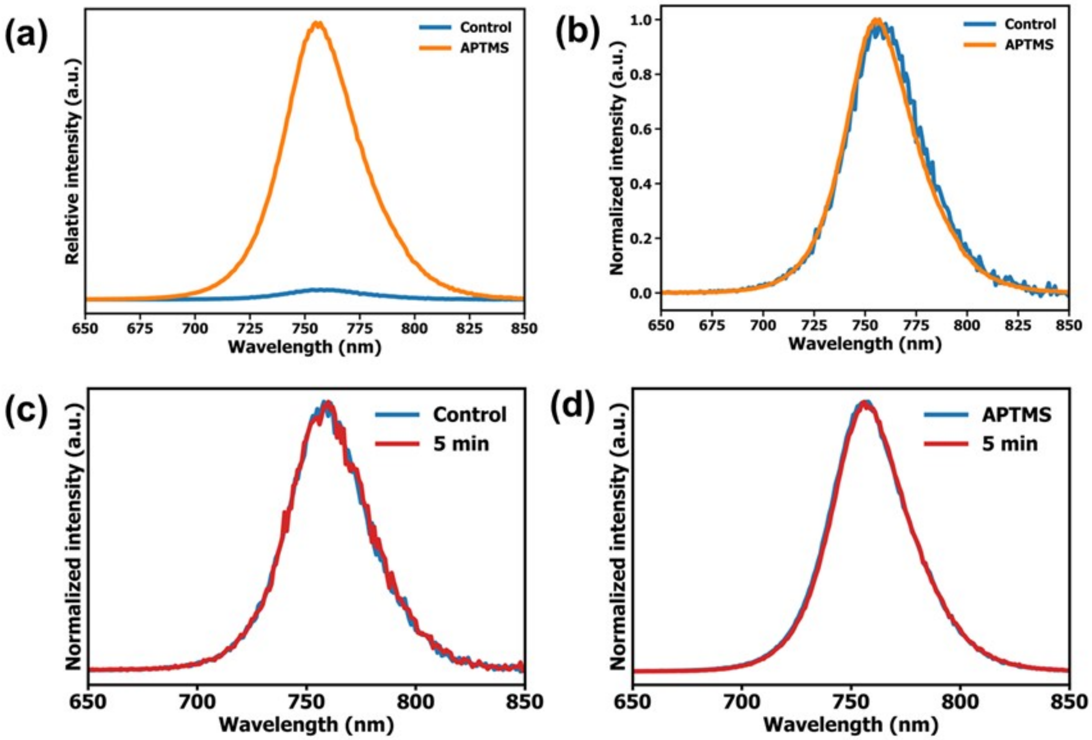

Figure B.1: (a) Relative and (b) normalized PL emission spectra of control and APTMSpassivated films at the excitation wavelength of 405 nm. Normalized PL emission of (c) control and (d) APTMS-treated perovskite films before and after 5 min light exposure to solar simulator at 1 Sun. We do not observe evidence for halide phase segregation under illumination.

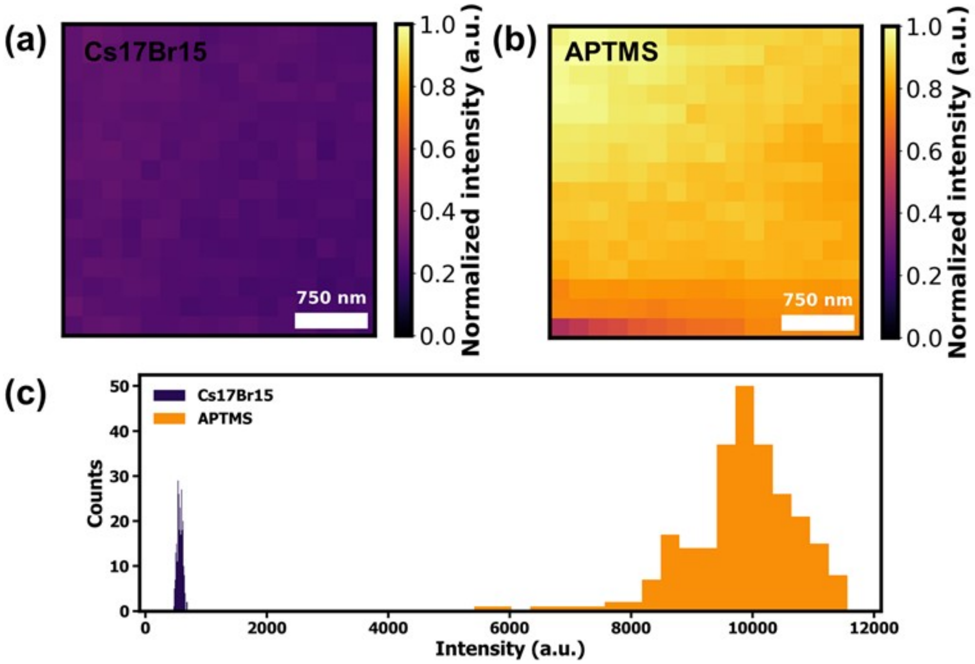

Figure B.2: Fluorescent lifetime microscopy (FLIM) results of (a) Cs17Br15 and (b) APTMSpassivated films under same excitation condition (470 nm laser).

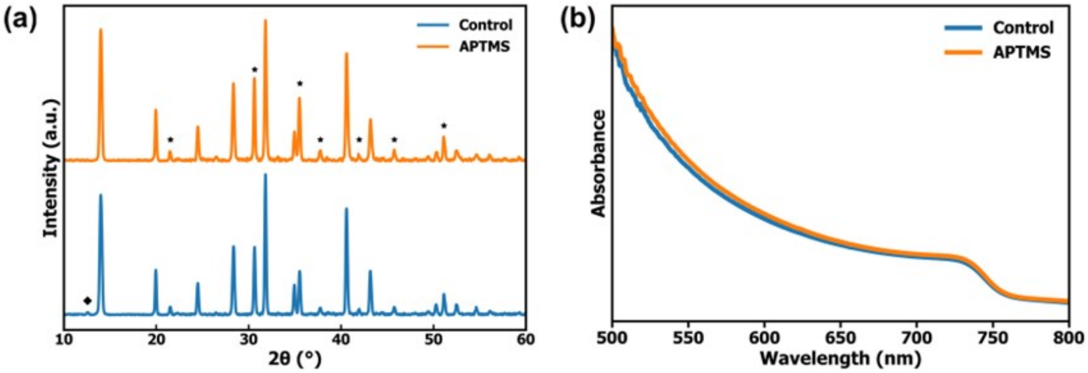

Figure B.3: (a) X-ray diffraction of control and APTMS passivated films, (b) UV-vis absorption spectra of control and APTMS passivated films. The diffraction peaks marked with asterisk in the spectra belongs to ITO substrate (both films were prepared on ITO glass substrates with HTL. The diffraction peak at ∼12.64° observed in the control film can be attributed to excess PbI_2.[126, 127]

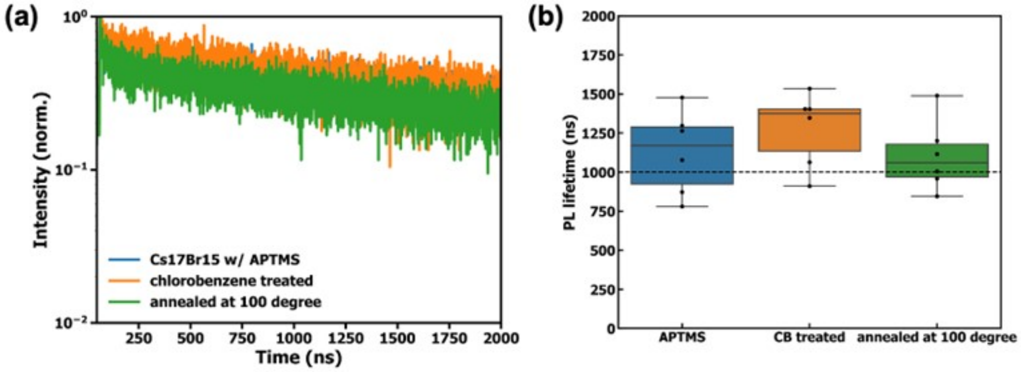

Figure B.4: (a) TRPL and (b) boxplot of PL lifetime of APMTS-passivated perovskite film, with chlorobenzene solvent treatment and heating at 100 °C.

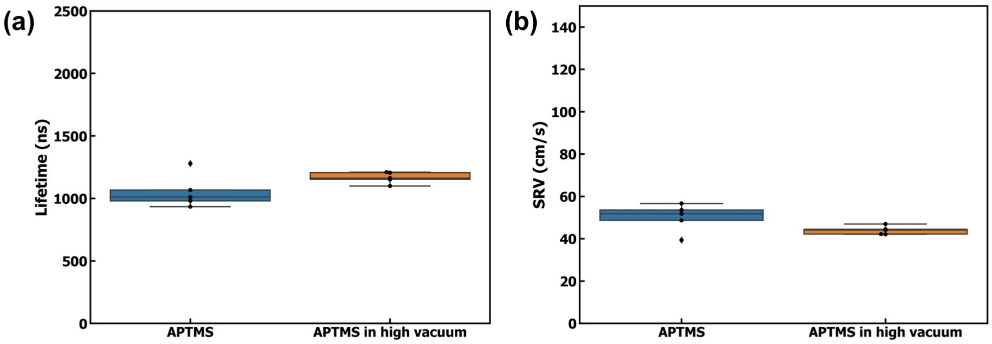

Figure B.5: Boxplot of (a) PL lifetime decay and (b) SRV of APMTS-passivated perovskite film before and after treatment in high vacuum.

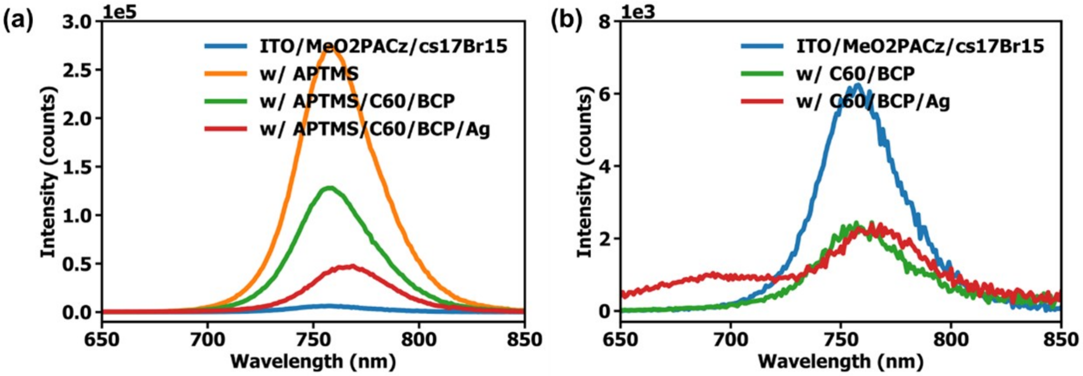

Figure B.6: Photoluminescence (PL) emission of half stack and full stack devices with (a) and (b) without APTMS passivation at the excitation wavelength of 405 nm.

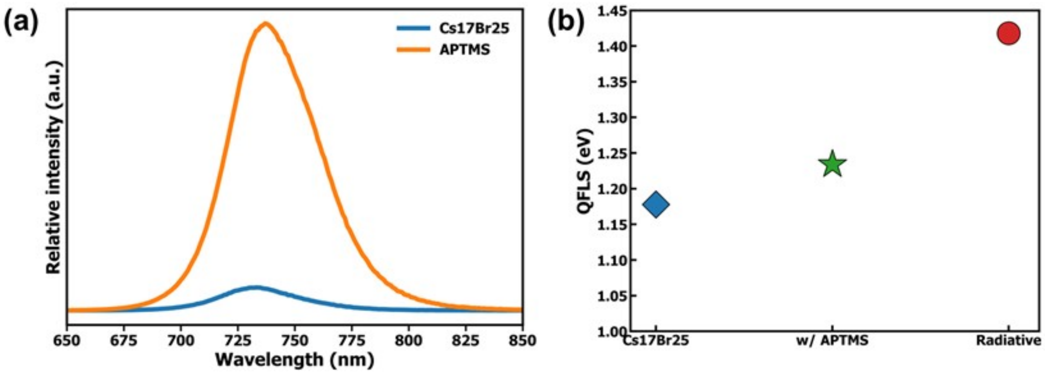

Figure B.7: PL emission and quasi-Fermi level splitting (QFLS) of Cs17Br25 with or without APTMS passivation (device structure is the same as the Cs17Br15 device). The red circle indicates the radiative limit for the Cs17Br15 bandgap.

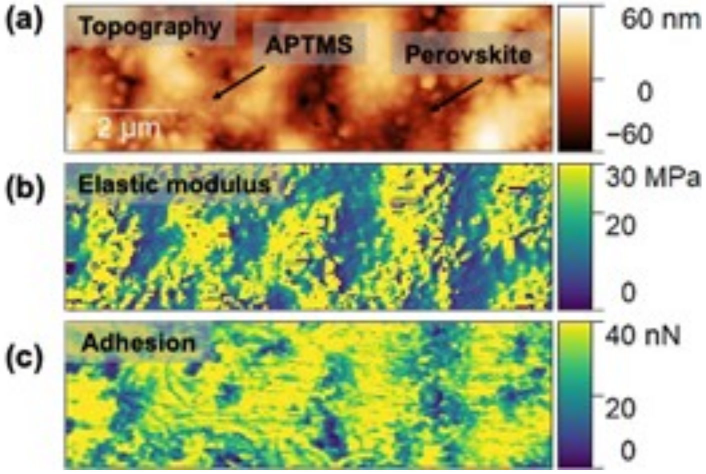

Figure B.8: AFM (a) topography, (b) elastic modulus, and (c) adhesion force maps of APTMS-treated perovskite films.

Samples	ITO/MeO-2PACz	w/ APTMS	w/ C_{60}/BCP	w/ Ag
Control	1.187 ± 0.005		1.151 ± 0.003	1.102 ± 0.007
APTMS		1.261 ± 0.008	1.240 ± 0.007	1.227 ± 0.013

Table B.1: Summary of QFLS (eV) for perovskite device stacks.

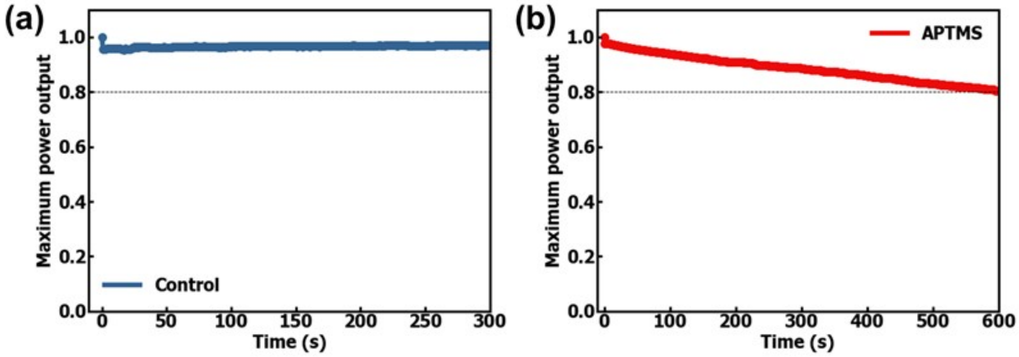

Figure B.9: Stability of (a) control and (b) APTMS-treated devices at maximum power point under 1 Sun illumination.

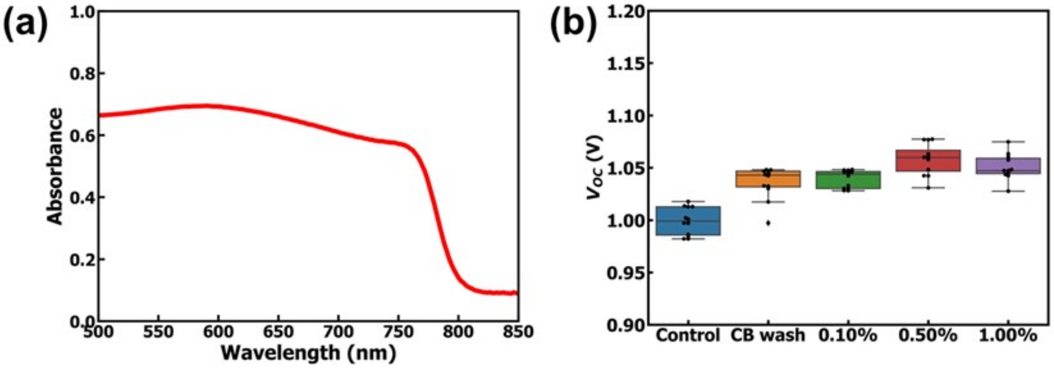

Figure B.10: (a) UV-vis absorption of mixed-cation Cs:FAPbI$_3$ perovskite with a bandgap of 1.57 eV and (b) corresponding device performance (V_{OC}) with APTMS treatment. (0.1%, 0.5% and 1% represent the volume ratio of APTMS in chlorobenzene (CB)). Data added to demonstrate observed performance improvements on an alternative perovskite chemistry with a different bandgap than in the main text. At the bandgap of 1.57 eV, we also observe a steady increase in V_{OC} with APTMS treatment. These are initial (unoptimized) results from an on-going APTMS perovskite-surface modification study on larger area perovskite devices and mini-modules.

Samples	V_{OC}	J_{SC} (mA/cm^2)	FF (%)	PCE (%)
Control	1.033 ± 0.011	21.14 ± 0.53	72.83 ± 2.48	15.90 ± 0.67
APTMS	1.094 ± 0.010	21.19 ± 0.35	77.78 ± 1.93	18.03 ± 0.66

Table B.2: Summary of the photovoltaic data for Cs17Br15 devices.

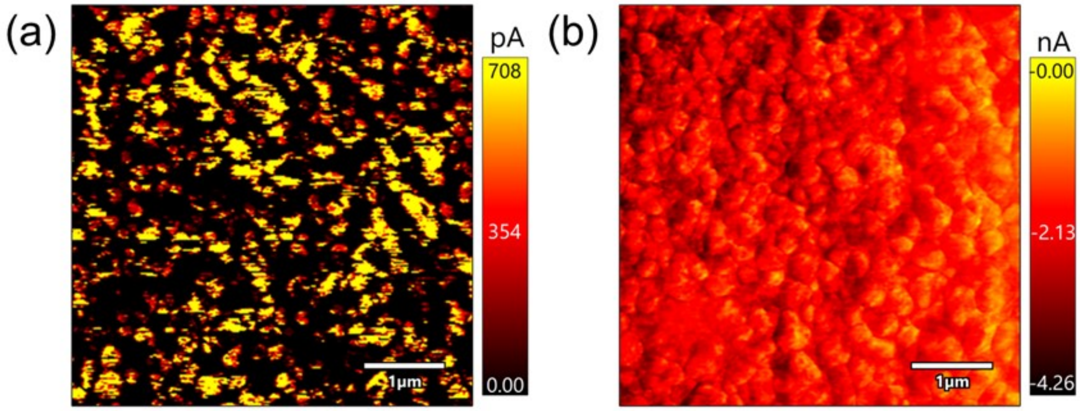

Figure B.11: cAFM images of APTMS-passivated film (a) under light (488 nm laser) with a positive bias of 1.5 V and (b) a half stack with C_{60} under light under short-circuit condition.

Appendix C

SUPPLEMENTARY INFORMATION FOR CHAPTER 4

C.1 Materials and methods

All precursors were used without further purification and stored and mixed in a nitrogen-filled glovebox. Formamidinium iodide (FAI, Greatcell), Cesium iodide (CsI, 99.999% metal basis, Alfa Aesar), lead iodide (PbI_2, perovskite grade, Tokyo Chemical Industries ltd (TCI)) and lead bromide ($PbBr_2$, 99.998% metals basis, Alfa Aesar) were dissolved in a mixture of anhydrous N,N-dimethylformamide (DMF, Sigma) and anhydrous dimethyl sulfoxide (DMSO, Sigma) with a volume ratio of 4:1 to prepare a 1.2 M solution of $FA_{0.83}Cs_{0.17}Pb(I_{0.75}Br_{0.25})_3$ (denoted as Cs17Br25) according to the stoichiometry. Me-4PACz was purchased from TCI. Patterned indium tin oxide (ITO, from Xin Yan Technology ltd) glass substrates and glass substrates (purchased from VWR) were cleaned by sequentially sonicating in water containing ~2% CH_2O multipurpose detergent, DI water, acetone, and isopropanol (IPA) for 10 mins each followed by UV-Ozone cleaning for 23 minutes. The perovskite precursor solution was dissolved and stored in the glovebox before Spincoating, which was filtered with a 0.2 μm PTFE filter before use and 40 μL of the solution was deposited on top of the substrate and spin-coated at for 10 s at 1000 rpm (200 rpm/s) and 35 s at 5000 rpm (800 rpm/s). 330 μL anhydrous anisole (Sigma) anti-solvent, filtered with 0.45 μm PTFE filter, was dropped from above when 5s spin-cating remained. The perovskite films were then annealed at 100 °C for 40 mins. The preparation of perovskite films was performed in a nitrogen-filled glovebox.

C.2 Synthesis of BzAOTs and BzAOTf organic salts

All chemicals were purchased from commercial sources and used as received, unless stated otherwise. Nuclear magnetic spectroscopy measurements were carried out on a Bruker Avance III HD 500 MHz instrument and calibrated using tetramethylsilane (TMS) as an internal reference ($Si(CH_3)4$, 0.0 ppm 1H NMR). Elemental analyses were carried out by Atlantic Microlabs using a LECO 932 CHNS elemental analyzer. Safety Note: Triflic acid is extremely corrosive and should be handled with caution.

Benzylammonium triflate (BzAOTf) was prepared according to a modified literature procedure [128]. A solution of triflic acid in diethyl ether was prepared in 250 mL round-bottomed flask equipped with a stir bar by adding approximately 0.874 mL (9.87 mmol) of triflic acid to 90 mL of cold diethyl ether, dropwise. Subsequently, (1.06 g, 9.87 mmol) of benzylamine was added dropwise. A white precipitate formed immediately. The product was isolated by vacuum filtration using a Büchner funnel and washed with excess cold diethyl ether. The isolated white solid was dried under high vacuum overnight (2.33g, 91.8%). 1H NMR (500 MHz, DMSO-d6) δ 8.06 (s, 3H), 7.48 – 7.35 (m, 5H), 4.04 (s, 2H). 19F NMR (471 MHz, DMSO-d6) δ -77.75. Anal. Calcd for C8H10F3NO3S: C, 37.36; H, 3.92; N, 5.45. Found: C, 37.46; H, 3.91; N, 5.34.

Benzylammonium Tosylate (BzAOTs) was prepared according to a modified literature procedure [128]. A solution of p-toluenesulfonic acid in methanol was prepared by dissolving 1.79 g (9.43 mmol) of p-toluenesulfonic acid monohydrate in portions to 25mL of 0°C methanol in a 250 mL round-bottomed flask equipped with a stir bar. Then 1.00 g (9.33 mmol) of benzylamine was added dropwise to the stirring p-toluenesulfonic acid solution. The product was precipitated by addition of cold diethyl ether (~60mL). A white precipitate formed immediately. The product was isolated by vacuum filtration over a Büchner funnel and washed with excess cold diethyl ether. The isolated white solid was dried under high vacuum overnight (2.18 g, 83.6%). 1H NMR (500 MHz, DMSO-d6) δ 8.06 (s, 3H), 7.50 – 7.43 (m, 5H), 7.44 – 7.34 (m, 2H), 7.11 (dt, J = 7.7, 0.7 Hz, 2H), 4.03 (s, 2H), 2.29 (s, 3H). Anal. Calcd for C14H17NO3S: C, 60.19; H, 6.13; N, 5.01. Found: C, 59.98; H, 6.18; N, 5.00.

C.3 Solar cell device fabrication and testing

For the device structure used in this study, Me-4PACz (TCI) was used as the hole transport layer and was prepared with a concentration of 0.5 mg/mL in anhydrous ethanol (Sigma). 100 µL of the HTL solution was put onto the ITO substate before spin-coating with 3000 rpm for 30 s, followed annealing at 100 °C for 10 mins inside of the glovebox. To obtain continuous perovskite film, Al_2O_3 (Sigma, diluted in IPA with 1:150 volume raito) nanoparticle was dynamically spun onto the substrates and then annealed for 2 mins. The perovskite films were deposited in the same as mentioned above. The BzAOTs and BzAOTf molecules were dissolved in anhydrous isopropanol (IPA) with a concentration of 10 mM. The interlayer solutions were dynamically spin-coated onto the perovskite films at 3000 rpm for 30 s without further annealing. The control devices were dynamically spin-coated with IPA solution to exclude the impact of IPA solvent. After that, 30 nm C_{60} and 5 nm Bathocuproine (BCP) were thermally evaporated onto the perovskite layer. For C_{60}, the deposition rate was from 0.2 Å/s for 5 nm to 0.5 Å/s for the rest of the total 25 nm. The deposition rate for BCP was 0.2 Å/s. 100 nm Ag was then thermally evaporated with an evaporation rate of 0.5 Å/s for the first 10 nm to 1 Å/s for the rest of the 90 nm. For solar cell performance measurement, current-voltage (J-V) scans under 1 Sun equivalent illumination were measured using an ORIEL LSH-7320 ABA LED solar simulator in a nitrogen-filled glovebox, which is calibrated with Silicon reference solar cell certified by NREL. The effective area of the solar cell is 0.0453 cm^2. J-V scans were performed with a Keithley 2400 controlled by a LabView program. The voltage values are scanned at a 0.02 V step in the range of -0.1 V to 1.24 V. The steady-state power output was carried out by measuring the solar cells under the bias of the maximum power point (MMP) and 1 sun.

C.4 Dipole moment calculations

Density Functional Theory (DFT) [129] calculations were conducted using the Generalized Gradient Approximation (GGA) [130] as realized in the Vienna Ab initio Simulation Package (VASP) [131]. The core-electron densities were described by a plane-wave basis set employing Projector Augmented Wave (PAW) potentials [132, 133]. We set the plane wave energy cutoff at 400 eV. For all structures examined, the Brillouin zones were sampled with Γ-centered 2x2x2 k-point meshes. To prevent periodic image interactions, each organic molecule was placed in a cubic simulation cell measuring 25Å per side. Subsequent structural optimizations were carried out (ISIF=2, IBRION=1), with convergence criteria set such that all forces were below 0.02 eV/Å. Upon obtaining fully relaxed structures, we proceeded to calculate the total dipole moments, incorporating monopole, dipole, and quadrupole corrections (IDIPOL=4) as well as dipole-dipole interaction corrections (LDIPOL=TRUE) to ensure accurate dipole moment estimations. Employing the above settings, the calculated dipole moment for OTs was found to be -11.63D, whereas for OTf, it was -4.4D.

C.5 Characterizations

Steady-state photoluminescence (PL) and time-resolved photoluminescence (TRPL) PL emission spectra were measured by using Edinburgh FLS1000 spectrometer. PL is measured with a Xenon lamp light source with an excitation wavelength of 640 nm with the same slits for all samples. TRPL spectra were acquired with PicoQuant Picoharp 300 TC-SPC system, a 640 nm picosecond pulsed diode laser. The repetition rate for the TRPL measurement was set to be 500 kHz for the perovskite samples without transport layer and to be 1 MHz for samples with transport layers, which was controlled by an external trigger input. A 700 nm long-pass filter was used in the TRPL measurement. Stretched exponential decay function was applied to fit the TRPL spectra to obtain the PL lifetime of each sample.

X-ray diffraction (XRD) XRD patterns of the samples were measured by the Bruker D8 powder X-ray diffractometer with a high-efficiency Cu anode microfocus x-ray source and an extremely sensitive Pilatus 100K large-area 2D detector. For the XRD patterns of the two organic molecules, they were finely grinded and then put onto the silicon wafer for the measurement.

UV-vis UV-vis absorbance spectra of the perovskite films with or without interlayers were measured on an Agilent 8453 UV-Vis Spectrometer in a range of 200-1100 nm.

X-ray photoelectron spectroscopy (XPS) The XPS spectra and high-resolution spectra of the samples were measured with the SARC-Kratos instrument equipped with a monochromatic Al Kα x-ray source as well as non-monochromatic Al and Mg sources. The spot size is around 700 μm $\times$300 μm.

Scanning Kelvin probe microscopy (SKPM) SKPM is a technique used to detect the contact potential difference (CPD) between the atomic force microscopy (AFM) tip and

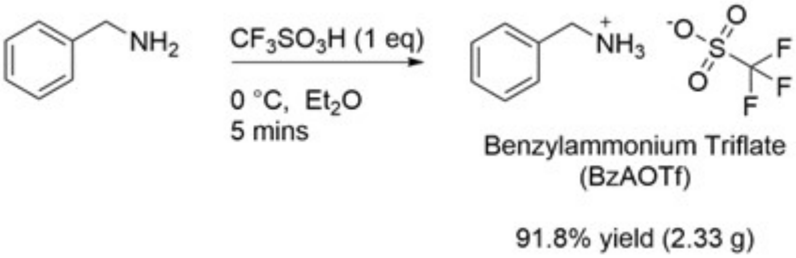

Figure C.1: Synthesis of benzylammonium triflate (BzAOTf).

the sample. The CPD is determined by the difference between the work function of the tip and the sample. Thus, electrical changes that occur in the sample to shift the work function of the sample can be understood through the CPD. All measurements were performed at room temperature, in the dark, and in a nitrogen flow cell. The SKPM measurements were made using an Asylum Research MFP-3D (Oxford Instruments) atomic force microscope mounted on an inverted Nikon Eclipse microscope and a customized piezo-stage. Cr/Pt-coated silicon tips (MikroMasch, 325 kHz, 40 N/m) were used to probe the CPD. For the work function calculations, highly ordered pyrolytic graphite (HOPG) was used to calibrate the samples' work function.

Time of flight secondary ion spectrometry (ToF-SIMS) ToF-SIMS was carried out by using a INOTOF TOF.SIMS5 spectrometer with a 25 keV Bi^{3+} cluster ion source in the pulsed mode. The spectra of positive and negative secondary ions were collected. The ion source was operated with a current of 0.05 pA with a dose of 1.0×10^{11} ions/cm^2 (per cycle) and an area of 200 µm × 200 µm. Ar 20 kV 1000 sputter beam with a current of 6.97 pA was used to sputter the sample with a dose of 5.1×10^{13} ions/cm^2 (per cycle) and an area of 500 µm × 500 µm.

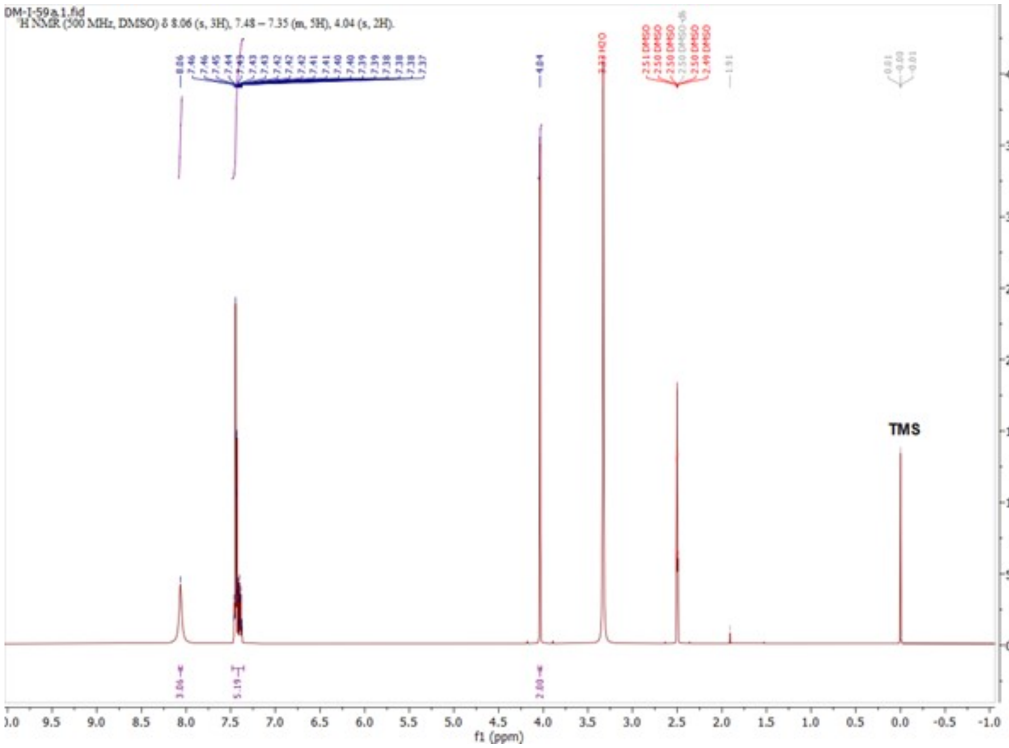

Figure C.2: ^{1}H-NMR spectrum of BzAOTf.

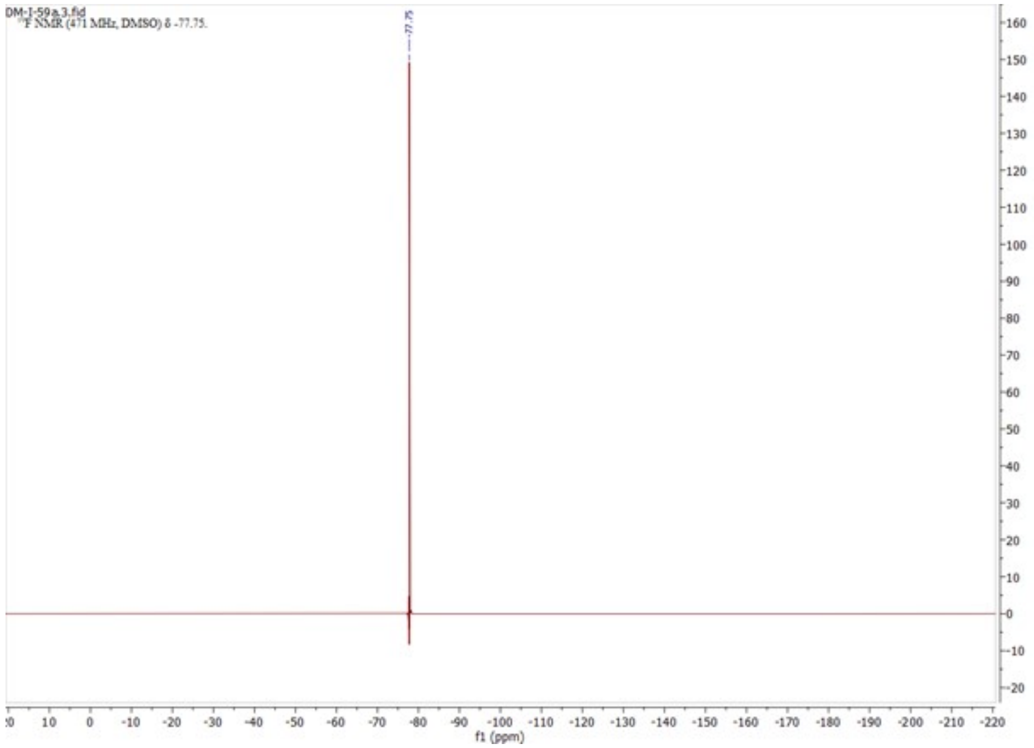

Figure C.3: ^{1}9F-NMR spectrum of BzAOTf in DMSO-d_6.

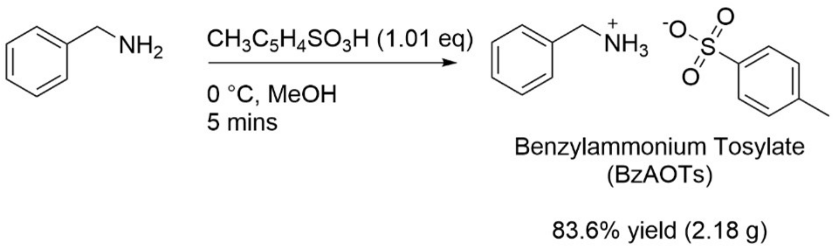

Figure C.4: Synthesis of benzylammonium tosylate (BzAOTs).

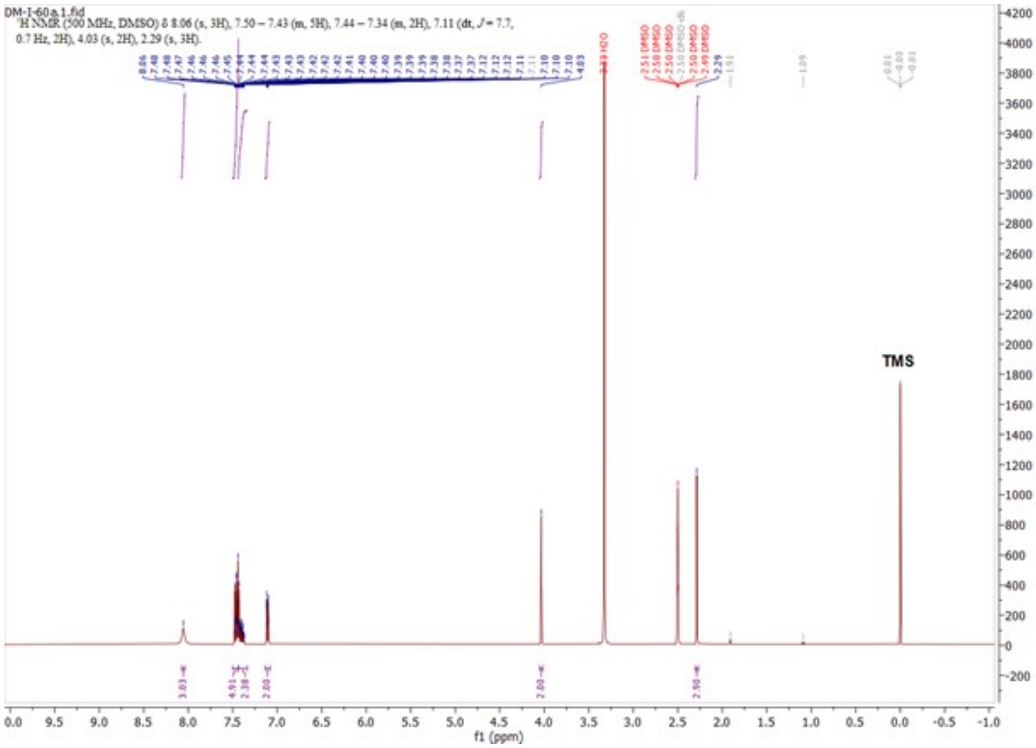

Figure C.5: ^{1}H-NMR of BzAOTs.

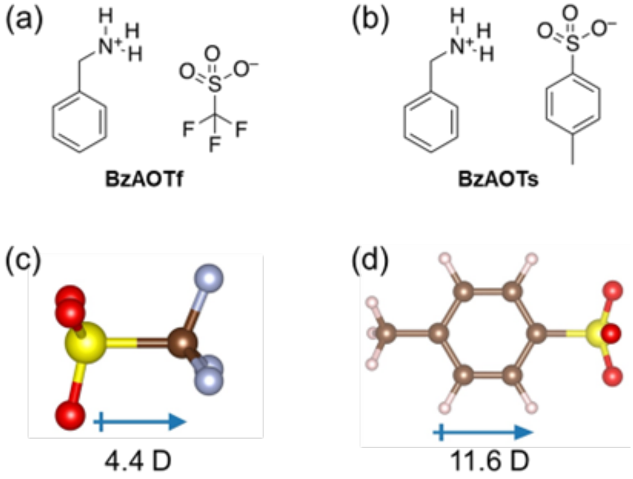

Figure C.6: (a) BzAOTf and (b) BzAOTs. Structure of (c) OTf and (d) OTs with dipole moment indicated. S is yellow. C is brown. H is light pink. O is red. blue arrow denotes dipole moment direction.

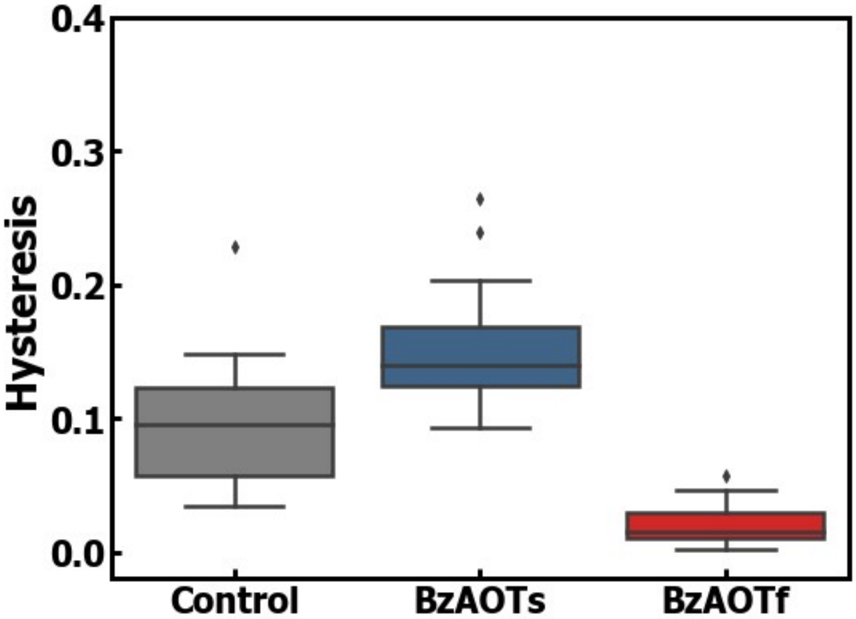

Figure C.7: Hysteresis index of the control, BzAOTs-treated and BzAOTf-treated devices.

Samples	PCE (%)	V_{OC} (V)	FF (%)	J_{SC} (mA/cm^2)	HI (%)
Control	15.78 ± 0.21	1.140 ± 0.003	70.61 ± 0.45	19.59 ± 0.20	0.098 ± 0.010
BzAOTs	17.61 ± 0.17	1.181 ± 0.002	76.34 ± 0.31	19.57 ± 0.08	0.150 ± 0.010
BzAOTf	17.59 ± 0.26	1.175 ± 0.003	76.46 ± 0.7	19.53 ± 0.13	0.0210 ± 0.004

Table C.1: Statistic distribution of device performance based on reverse scan.

Composition	E$_g$ (eV)	CB (eV)	VB (eV)	WF (eV)	Refs
$FA_{0.83}Cs_{0.17}Pb(I_{0.85}Br_{0.15})_3$	1.63	-4.01	-5.64		57
$FA_{0.8}Cs_{0.2}Pb(I_{0.6}Br_{0.4})_3$	1.78	-3.81	-5.59	-4.76	137
$FA_{0.83}Cs_{0.17}Pb(I_{0.6}Br_{0.4})_3$	1.72	-4.39	-6.11	-4.27	138
$FA_{0.83}Cs_{0.17}PbI_{2.5}Br_{0.5}$	1.65	-4.09	-5.74	-4.32	139
$FA_{0.83}Cs_{0.17}PbI_2Br$	1.74	-4.02	-5.76	-4.39	139

Table C.2: Survey of interfacial energetics of halide perovskite [57, 134, 135, 136].

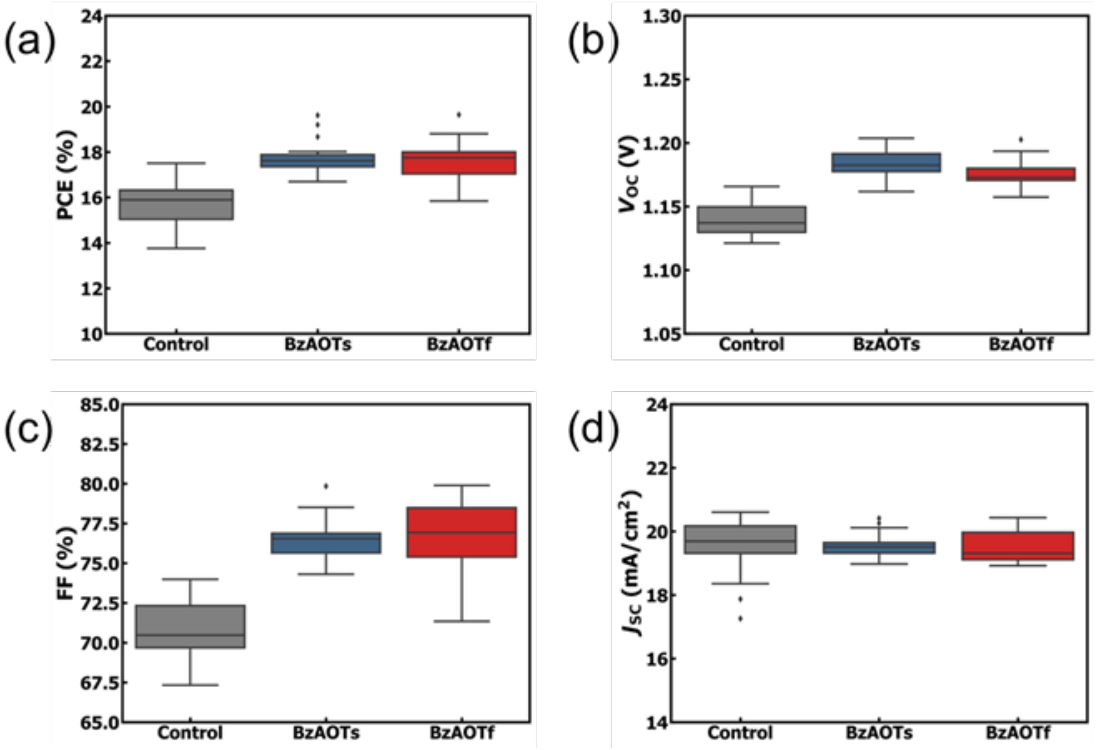

Figure C.8: Statistical distribution of (a) PCE, (b) V_{OC}, (c) FF and (d) J_{SC} of control, BzAOTs-treated and BzAOTf-treated devices based on reverse scan.

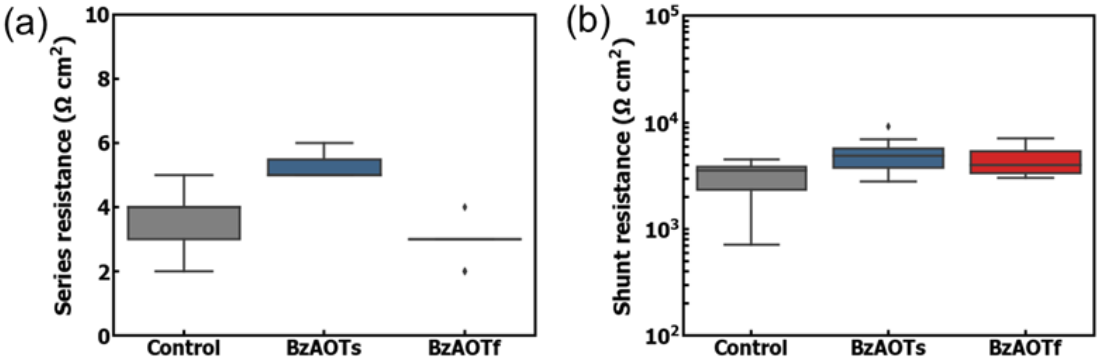

Figure C.9: (a) Series resistance and (b) shunt resistance of perovskite solar cell devices without or with BzAOTs and BZAOTf surface treatment.

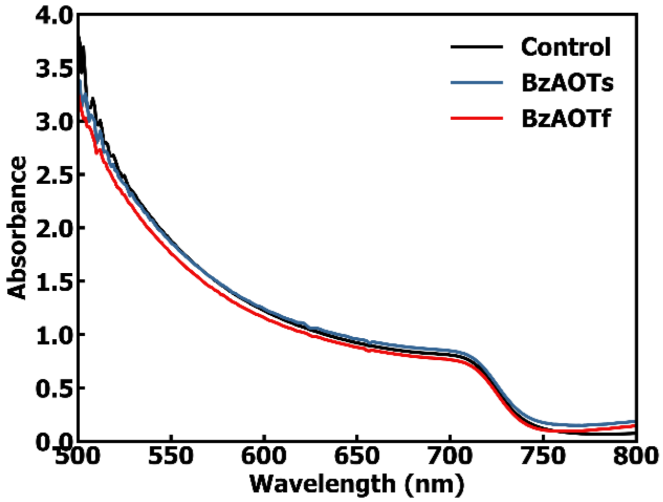

Figure C.10: UV-vis absorption spectra of perovskite films on ITO/Me-4PACz with or without surface treatment.

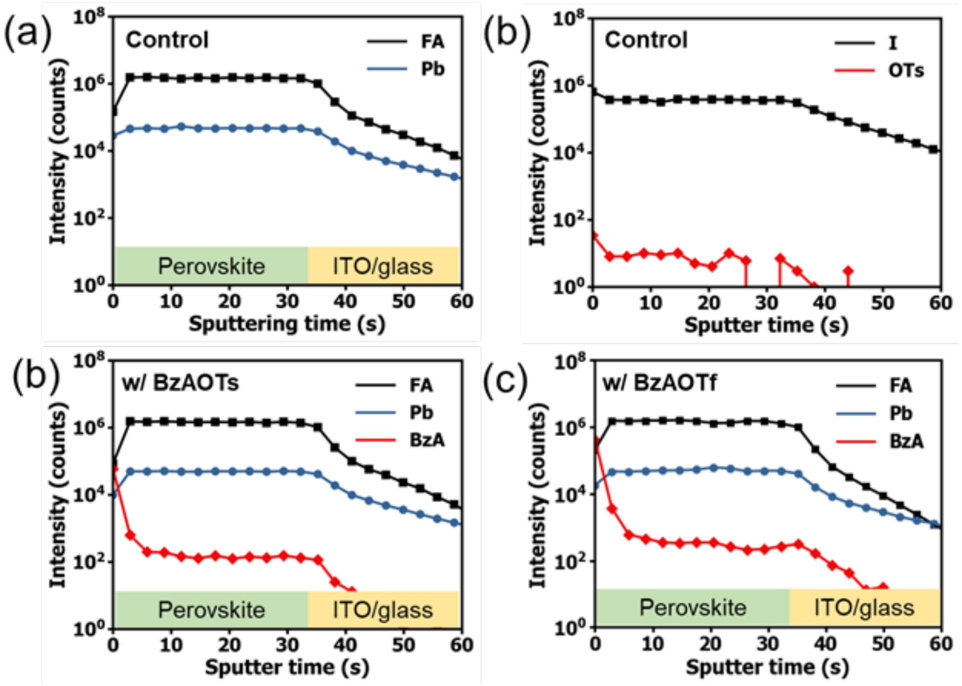

Figure C.11: Depth-dependent TOF-SIMS of cation profile of control, BzAOTs-treated and BzAOTf-treated perovskite films.

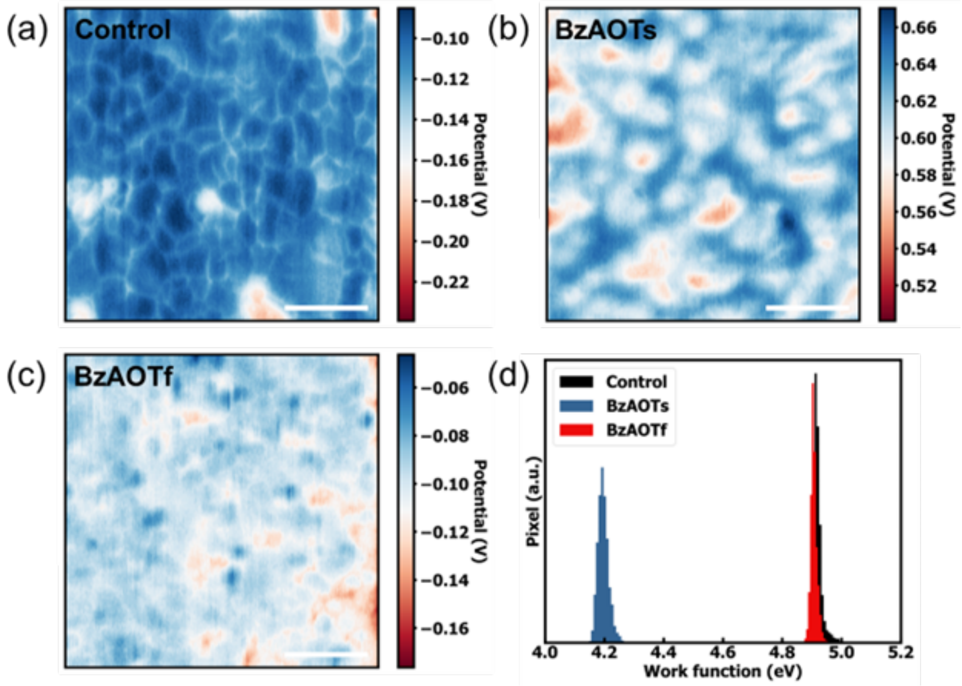

Figure C.12: Surface potential of (a) pristine perovskite film, (b) OTs-treated and (c) OTf-treated perovskite films measured with scanning Kelvin probe microscopy (SKPM) under dark and inside of nitrogen flow cell. (d) Work function of the perovskite films converted with highly ordered pyrolytic graphite (HOPG) as the reference.

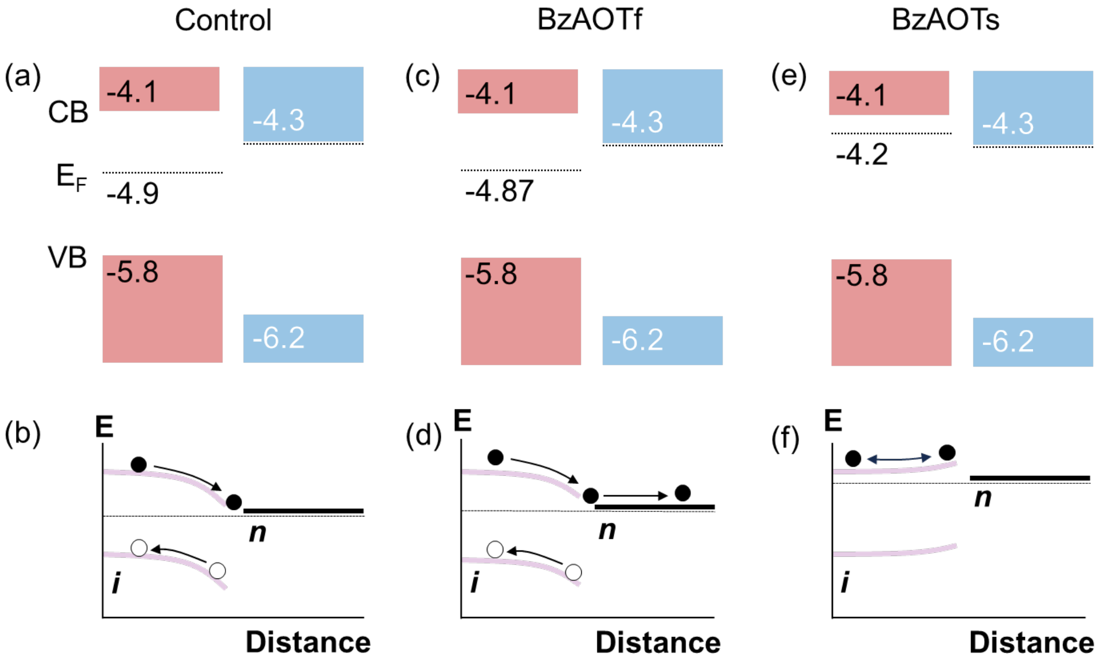

Figure C.13: Energetics in isolation for the control perovskite surface & C_{60} and (b) sketch of band structure (E) at the perovskite/C_{60} interface. (c) Energetics in isolation for BzAOTf-treated perovskite & C_{60} and (d) sketch of band structure (E) at the BzAOTf-treated perovskite/C_{60} interface. (e) Energetics in isolation for BzAOTs-treated perovskite & C_{60} and (f) sketch of band structure (E) at the perovskite/C_{60} interface. Here we assume the C_{60} is strongly n-doped.

VITA

EDUCATION

University of Washington, Seattle, USA *Sep. 2019 - Jun. 2024*

Ph.D. in Molecular Engineering: Data Science

Advisor: Prof. David S. Ginger

M.S. in Molecular Engineering *Sep. 2019 - Jun. 2022*

KTH Royal Institute of Technology, Stockholm, Sweden *Aug. 2015 - Jan. 2016*

Visiting student

Dalian University of Technology, Dalian, China

M.E. in Chemical Engineering *Sep. 2016 - Jun. 2019*

Advisor: Prof. Junwei Ye and Prof. Guiling Ning

B.E. in Chemical Engineering *Sep. 2012 - Jun. 2016*

PUBLICATIONS

---

1. **Shi, Y.**, McCarthy, D.P., Ho, K., Jiang, F., Yang, Z., Xiang, X., Wesbrook, R., Taddei, M., Contreras, H., Barlow, S., Dunham, S., Armstrong, N., Marder, S., and Ginger, D.S.,2024. Sulfonate anions suppress interfacial recombination in perovskite solar cells via surface field and electronic decoupling. In preparation.

2. **Shi, Y.***, McCarthy, D.P.*, Lungwitz, D., Jiang, F., Taddei, M., Contreras, H., Lin, Y., Mohapatra, A.A., Tang, K., Zhang, Y., Barlow, S., Kahn, A., Marder, S.R. and Ginger, D.S., 2024. Photo-Crosslinkable Naphthalene Diimide Polymer for Solution-Processed n–i–p Perovskite Solar Cells. *Chemistry of Materials*, 36(2), pp.795-802.

3. Huang, Y.*, **Shi, Y.***, Cohen, T.A., Ho, K. and Luscombe, C.K., 2023. Studying

Hydrogen–Halide Interactions in Lead Halide Perovskite with Isoelectronic Cations. *Chemistry of Materials*, 35(20), pp.8417-8425.

4. **Shi, Y.**, Rojas-Gatjens, E., Wang, J., Pothoof, J., Giridharagopal, R., Ho, K., Jiang, F., Taddei, M., Yang, Z., Sanehira, E.M. and Irwin, M.D., 2022. (3-Aminopropyl) trimethoxysilane surface passivation improves perovskite solar cell performance by reducing surface recombination velocity. *ACS Energy Letters*, 7(11), pp.4081-4088.

5. deQuilettes, D.W., Yoo, J.J., Brenes, R., Kosasih, F.U., Laitz, M., Dou, B.D., Graham, D.J., Ho, K., **Shi, Y.**, Shin, S.S. and Ducati, C., 2024. Reduced recombination via tunable surface fields in perovskite thin films. *Nature Energy*, pp.1-10

6. Jiang, F., **Shi, Y.**, Rana, T.R., Morales, D., Gould, I., McCarthy, D.P., Smith, J., Christoforo, G., Contreras, H., Barlow, S. and Mohite, A.D., 2023. Architecture Optimization Dramatically Improves Reverse Bias Stability in Perovskite Solar Cells: A Role of Polymer Hole Transport Layers. Submitted.

7. Rojas-Gatjens, E., Yallum, K.M., **Shi, Y.**, Zheng, Y., Bills, T., Perini, C.A., Correa-Baena, J.P., Ginger, D.S., Banerji, N. and Silva-Acuña, C., 2023. Resolving nonlinear recombination dynamics in semiconductors via ultrafast excitation correlation spectroscopy: Photoluminescence versus photocurrent detection. *The Journal of Physical Chemistry C*, 127(32), pp.15969-15977.

8. Fürer, S.O., Rietwyk, K.J., Pulvirenti, F., McMeekin, D.P., Surmiak, M.A., Raga, S.R., Mao, W., Lin, X., Hora, Y., Wang, J., **Shi, Y.**, Barlow, S., Ginger, D., Marder, S. and Bach, U., 2023. Naphthalene-imide self-assembled monolayers as a surface modification of ITO for improved thermal stability of perovskite solar cells. *ACS Applied Energy Materials*, 6(2), pp.667-677.

9. Chang, C., **Shi, Y.**, Zou, C. and Lin, L.Y., 2023. $MAPbBr_3$ First-Order Distributed Feedback Laser with High Stability. *Advanced Photonics Research*, 4(1), p.2200071.

10. Taddei, M., Smith, J.A., Gallant, B.M., Zhou, S., Westbrook, R.J., **Shi, Y.**, Wang, J., Drysdale, J.N., McCarthy, D.P., Barlow, S. and Marder, S.R., 2022. Ethylenediamine addition improves performance and suppresses phase instabilities in mixed-halide perovskites. *ACS Energy Letters*, 7(12), pp.4265-4273.

11. Jariwala, S., Kumar, R.E., Eperon, G.E., **Shi, Y.**, Fenning, D.P. and Ginger, D.S., 2021. Dimethylammonium addition to halide perovskite precursor increases vertical and lateral heterogeneity. *ACS Energy Letters*, 7(1), pp.204-210.

12. Valverde-Chávez, D.A., Rojas-Gatjens, E., Williamson, J., Jariwala, S., **Shi, Y.**, McCarthy, D.P., Barlow, S., Marder, S.R., Ginger, D.S. and Silva-Acuña, C., 2021. Nonlinear photocarrier dynamics and the role of shallow traps in mixed-halide mixed-cation hybrid perovskites. *Journal of Materials Chemistry C*, 9(26), pp.8204-8212.

BIBLIOGRAPHY

[1] Thomas R Karl and Kevin E Trenberth. “Modern global climate change”. In: *science* 302.5651 (2003), pp. 1719–1723.

[2] Wilfried Thuiller. “Climate change and the ecologist”. In: *Nature* 448.7153 (2007), pp. 550–552.

[3] Felix Creutzig et al. “The underestimated potential of solar energy to mitigate climate change”. In: *Nature Energy* 2.9 (2017), pp. 1–9.

[4] Ehsanul Kabir et al. “Solar energy: Potential and future prospects”. In: *Renewable and Sustainable Energy Reviews* 82 (2018), pp. 894–900.

[5] Estelle Gervais et al. “Raw material needs for the large-scale deployment of photovoltaics–Effects of innovation-driven roadmaps on material constraints until 2050”. In: *Renewable and Sustainable Energy Reviews* 137 (2021), p. 110589.

[6] Martin A Green, Anita Ho-Baillie, and Henry J Snaith. “The emergence of perovskite solar cells”. In: *Nature photonics* 8.7 (2014), pp. 506–514.

[7] National Renewable Energy Laboratory. *Best research-cell efficiencies.* 2024. (accessed 2024-05-26).

[8] Hyun Suk Jung and Nam-Gyu Park. “Perovskite solar cells: from materials to devices”. In: *small* 11.1 (2015), pp. 10–25.

[9] Tze-Bin Song et al. “Perovskite solar cells: film formation and properties”. In: *Journal of Materials Chemistry A* 3.17 (2015), pp. 9032–9050.

[10] Samuel D Stranks et al. “The physics of light emission in halide perovskite devices”. In: *Advanced materials* 31.47 (2019), p. 1803336.

[11] Dane W DeQuilettes et al. “Photoluminescence lifetimes exceeding 8 μs and quantum yields exceeding 30% in hybrid perovskite thin films by ligand passivation”. In: *ACS Energy Letters* 1.2 (2016), pp. 438–444.

[12] Dane W deQuilettes et al. “Reduced recombination via tunable surface fields in perovskite thin films”. In: *Nature Energy* (2024), pp. 1–10.

[13] Samuel D Stranks et al. “Electron-hole diffusion lengths exceeding 1 micrometer in an organometal trihalide perovskite absorber”. In: *Science* 342.6156 (2013), pp. 341–344.

[14] David P McMeekin et al. “A mixed-cation lead mixed-halide perovskite absorber for tandem solar cells”. In: *Science* 351.6269 (2016), pp. 151–155.

[15] Feng Hao et al. “Anomalous band gap behavior in mixed Sn and Pb perovskites enables broadening of absorption spectrum in solar cells”. In: *Journal of the American Chemical Society* 136.22 (2014), pp. 8094–8099.

[16] Giles E Eperon et al. “Formamidinium lead trihalide: a broadly tunable perovskite for efficient planar heterojunction solar cells”. In: *Energy & Environmental Science* 7.3 (2014), pp. 982–988.

[17] Marina R Filip et al. “Steric engineering of metal-halide perovskites with tunable optical band gaps”. In: *Nature communications* 5.1 (2014), p. 5757.

[18] EL Unger et al. “Roadmap and roadblocks for the band gap tunability of metal halide perovskites”. In: *Journal of Materials Chemistry A* 5.23 (2017), pp. 11401–11409.

[19] Nam-Gyu Park and Kai Zhu. “Scalable fabrication and coating methods for perovskite solar cells and solar modules”. In: *Nature Reviews Materials* 5.5 (2020), pp. 333–350.

[20] Jian Wang et al. “Reducing surface recombination velocities at the electrical contacts will improve perovskite photovoltaics”. In: *ACS Energy Letters* 4.1 (2018), pp. 222–227.

[21] National Renewable Energy Laboratory. *Best research-cell efficiencies.* 2023. (accessed 2023-7-28).

[22] Jiarong Lian et al. “Electron-transport materials in perovskite solar cells”. In: *Small Methods* 2.10 (2018), p. 1800082.

[23] Liangyou Lin et al. “Inorganic electron transport materials in perovskite solar cells”. In: *Advanced Functional Materials* 31.5 (2021), p. 2008300.

[24] Tomas Leijtens et al. “Overcoming ultraviolet light instability of sensitized TiO_2 with meso-superstructured organometal tri-halide perovskite solar cells”. In: *Nature communications* 4.1 (2013), p. 2885.

[25] Mohammed A Jameel et al. “Naphthalene diimide-based electron transport materials for perovskite solar cells”. In: *Journal of Materials Chemistry A* 9.48 (2021), pp. 27170–27192.

[26] Heetae Yoon et al. “Hysteresis-free low-temperature-processed planar perovskite solar cells with 19.1% efficiency”. In: *Energy & Environmental Science* 9.7 (2016), pp. 2262–2266.

[27] Jin Hyuck Heo et al. “Hysteresis-less inverted $CH_3NH_3PbI_3$ planar perovskite hybrid solar cells with 18.1% power conversion efficiency”. In: *Energy & Environmental Science* 8.5 (2015), pp. 1602–1608.

[28] Yangwei Shi et al. “(3-Aminopropyl) trimethoxysilane surface passivation improves perovskite solar cell performance by reducing surface recombination velocity”. In: *ACS Energy Letters* 7.11 (2022), pp. 4081–4088.

[29] Su-Kyo Jung et al. “Non-Fullerene Organic Electron-Transporting Materials for Perovskite Solar Cells”. In: *ChemSusChem* 11.22 (2018), pp. 3882–3892.

[30] Jonathan Warby et al. “Understanding performance limiting interfacial recombination in pin perovskite solar cells”. In: *Advanced Energy Materials* 12.12 (2022), p. 2103567.

[31] Kui Jiang et al. “Naphthodiperylenetetraimide-based polymer as electron-transporting material for efficient inverted perovskite solar cells”. In: *ACS applied materials & interfaces* 10.42 (2018), pp. 36549–36555.

[32] Cheng Chen et al. “Molecular engineering of ionic type perylenediimide dimer-based electron transport materials for efficient planar perovskite solar cells”. In: *Materials Today Energy* 9 (2018), pp. 264–270.

[33] Su-Kyo Jung et al. “Homochiral Asymmetric-Shaped Electron-Transporting Materials for Efficient Non-Fullerene Perovskite Solar Cells”. In: *ChemSusChem* 12.1 (2019), pp. 224–230.

[34] Su-Kyo Jung et al. “Nonfullerene electron transporting material based on naphthalene diimide small molecule for highly stable perovskite solar cells with efficiency exceeding 20%”. In: *Advanced Functional Materials* 28.20 (2018), p. 1800346.

[35] Hong Il Kim et al. “Improving the performance and stability of inverted planar flexible perovskite solar cells employing a novel NDI-based polymer as the electron transport layer”. In: *Advanced Energy Materials* 8.16 (2018), p. 1702872.

[36] Zonglong Zhu et al. “Highly efficient and stable perovskite solar cells enabled by all-crosslinked charge-transporting layers”. In: *Joule* 2.1 (2018), pp. 168–183.

[37] Dongbing Zhao et al. “Hexaazatrinaphthylene derivatives: Efficient electron-transporting materials with tunable energy levels for inverted perovskite solar cells”. In: *Angewandte Chemie* 128.31 (2016), pp. 9145–9149.

[38] Jesse TE Quinn et al. “Recent progress in the development of n-type organic semiconductors for organic field effect transistors”. In: *Journal of Materials Chemistry C* 5.34 (2017), pp. 8654–8681.

[39] Sheshanath V Bhosale, Chintan H Jani, and Steven J Langford. “Chemistry of naphthalene diimides”. In: *Chemical Society Reviews* 37.2 (2008), pp. 331–342.

[40] Agnieszka Nowak-Król et al. “Naphthalene and perylene diimides–better alternatives to fullerenes for organic electronics?” In: *Chemical communications* 54.98 (2018), pp. 13763–13772.

[41] He Yan et al. “High-performance hole-transport layers for polymer light-emitting diodes. Implementation of organosiloxane cross-linking chemistry in polymeric electroluminescent devices”. In: *Journal of the American Chemical Society* 127.9 (2005), pp. 3172–3183.

[42] Che-En Tsai et al. “Triarylamine-based crosslinked hole-transporting material with an ionic dopant for high-performance PEDOT: PSS-free polymer solar cells”. In: *Journal of Materials Chemistry C* 3.24 (2015), pp. 6158–6165.

[43] Carlos A Zuniga, Stephen Barlow, and Seth R Marder. “Approaches to solution-processed multilayer organic light-emitting diodes based on cross-linking”. In: *Chemistry of Materials* 23.3 (2011), pp. 658–681.

[44] Nobuhiro Kawatsuki et al. “Photoreaction of photo-cross-linkable methacrylate polymer films comprising 2-cinnamoyloxyethoxybiphenyl side group by linearly polarized ultraviolet light and liquid crystal alignment on the resultant films”. In: *Chemistry of materials* 12.6 (2000), pp. 1549–1555.

[45] Pankaj Gupta et al. “In situ photo-cross-linking of cinnamate functionalized poly (methyl methacrylate-co-2-hydroxyethyl acrylate) fibers during electrospinning”. In: *Macromolecules* 37.24 (2004), pp. 9211–9218.

[46] Marie-Hélène Tremblay et al. “A photo-crosslinkable bis-triarylamine side-chain polymer as a hole-transport material for stable perovskite solar cells”. In: *Sustainable Energy & Fuels* 4.1 (2020), pp. 190–198.

[47] Ya-Dong Zhang et al. “Photo-crosslinkable polymers as hole-transport materials for organic light-emitting diodes”. In: *Journal of Materials Chemistry* 12.6 (2002), pp. 1703–1708.

[48] Shi-Joon Sung et al. “Two different reaction mechanisms of cinnamate side groups attached to the various polymer backbones”. In: *Polymer* 47.7 (2006), pp. 2314–2321.

[49] Khaled Al Kurdi et al. “A naphthalene diimide side-chain polymer as an electron-extraction layer for stable perovskite solar cells”. In: *Materials Chemistry Frontiers* 5.1 (2021), pp. 450–457.

[50] Hio-Ieng Un et al. “Understanding the effects of molecular dopant on n-type organic thermoelectric properties”. In: *Advanced Energy Materials* 9.24 (2019), p. 1900817.

[51] Min Je Kim et al. “Universal three-dimensional crosslinker for all-photopatterned electronics”. In: *Nature communications* 11.1 (2020), p. 1520.

[52] Yunlong Guo et al. "n-Type doping for efficient polymeric electron-transporting layers in perovskite solar cells". In: *Journal of materials chemistry A* 4.48 (2016), pp. 18852–18856.

[53] Hao Chen et al. "Regulating surface potential maximizes voltage in all-perovskite tandems". In: *Nature* 613.7945 (2023), pp. 676–681.

[54] Sebastian O Fürer et al. "Naphthalene-imide self-assembled monolayers as a surface modification of ITO for improved thermal stability of perovskite solar cells". In: *ACS Applied Energy Materials* 6.2 (2023), pp. 667–677.

[55] Marc Burgelman et al. "Advanced electrical simulation of thin film solar cells". In: *Thin solid films* 535 (2013), pp. 296–301.

[56] Marc Burgelman, Peter Nollet, and Stefaan Degrave. "Modelling polycrystalline semiconductor solar cells". In: *Thin solid films* 361 (2000), pp. 527–532.

[57] Sarthak Jariwala et al. "Reducing surface recombination velocity of methylammonium-free mixed-cation mixed-halide perovskites via surface passivation". In: *Chemistry of Materials* 33.13 (2021), pp. 5035–5044.

[58] Margherita Taddei et al. "Ethylenediamine addition improves performance and suppresses phase instabilities in mixed-halide perovskites". In: *ACS Energy Letters* 7.12 (2022), pp. 4265–4273.

[59] Heon Jin et al. "Alumina Nanoparticle Interfacial Buffer Layer for Low-Bandgap Lead-Tin Perovskite Solar Cells". In: *Advanced Functional Materials* 33.35 (2023), p. 2303012.

[60] Hua Zhang et al. "$CuGaO_2$: A promising inorganic hole-transporting material for highly efficient and stable perovskite solar cells". In: *Advanced materials* 29.8 (2017), p. 1604984.

[61] Cong Liu et al. "Grain boundary modification via F4TCNQ to reduce defects of perovskite solar cells with excellent device performance". In: *ACS applied materials & interfaces* 10.2 (2018), pp. 1909–1916.

[62] Yang Li et al. “Benefits of the hydrophobic surface for $CH_3NH_3PbI_3$ crystalline growth towards highly efficient inverted perovskite solar cells”. In: *Molecules* 24.10 (2019), p. 2027.

[63] Jiyong Lee and Seunghyun Baik. “Enhanced crystallinity of $CH_3NH_3PbI_3$ by the pre-coordination of PbI_2–DMSO powders for highly reproducible and efficient planar heterojunction perovskite solar cells”. In: *RSC advances* 8.2 (2018), pp. 1005–1013.

[64] Michael Saliba et al. “Perovskite solar cells: from the atomic level to film quality and device performance”. In: *Angewandte Chemie International Edition* 57.10 (2018), pp. 2554–2569.

[65] Sarthak Jariwala et al. “Local crystal misorientation influences non-radiative recombination in halide perovskites”. In: *Joule* 3.12 (2019), pp. 3048–3060.

[66] Akihiro Kojima et al. “Organometal halide perovskites as visible-light sensitizers for photovoltaic cells”. In: *Journal of the american chemical society* 131.17 (2009), pp. 6050–6051.

[67] Michael M Lee et al. “Efficient hybrid solar cells based on meso-superstructured organometal halide perovskites”. In: *science* 338.6107 (2012), pp. 643–647.

[68] Mingzhen Liu, Michael B Johnston, and Henry J Snaith. “Efficient planar heterojunction perovskite solar cells by vapour deposition”. In: *Nature* 501.7467 (2013), pp. 395–398.

[69] Emma R Dohner, Eric T Hoke, and Hemamala I Karunadasa. “Self-assembly of broadband white-light emitters”. In: *Journal of the American Chemical Society* 136.5 (2014), pp. 1718–1721.

[70] Brandon R Sutherland and Edward H Sargent. “Perovskite photonic sources”. In: *Nature Photonics* 10.5 (2016), pp. 295–302.

[71] Rui Zhang et al. “Nonlinear optical response of organic–inorganic halide perovskites”. In: *ACS Photonics* 3.3 (2016), pp. 371–377.

[72] Franziska Muckel et al. “Tuning Hybrid exciton–Photon Fano Resonances in Two-Dimensional Organic–Inorganic Perovskite Thin Films”. In: *Nano Letters* 21.14 (2021), pp. 6124–6131.

[73] National Renewable Energy Laboratory. *Best research-cell efficiencies.* 2022. (accessed 2022-06-18).

[74] Christian M Wolff et al. “Nonradiative recombination in perovskite solar cells: the role of interfaces”. In: *Advanced Materials* 31.52 (2019), p. 1902762.

[75] Jing Wang et al. “Highly efficient all-inorganic perovskite solar cells with suppressed non-radiative recombination by a Lewis base”. In: *Nature communications* 11.1 (2020), p. 177.

[76] Deying Luo et al. “Minimizing non-radiative recombination losses in perovskite solar cells”. In: *Nature Reviews Materials* 5.1 (2020), pp. 44–60.

[77] Martin Stolterfoht et al. “Visualization and suppression of interfacial recombination for high-efficiency large-area pin perovskite solar cells”. In: *Nature Energy* 3.10 (2018), pp. 847–854.

[78] Ian L Braly et al. “Hybrid perovskite films approaching the radiative limit with over 90% photoluminescence quantum efficiency”. In: *Nature Photonics* 12.6 (2018), pp. 355–361.

[79] Kristofer Tvingstedt et al. “Removing leakage and surface recombination in planar perovskite solar cells”. In: *ACS Energy Letters* 2.2 (2017), pp. 424–430.

[80] Damian Głowienka et al. “Role of surface recombination in perovskite solar cells at the interface of HTL/$CH_3NH_3PbI_3$”. In: *Nano Energy* 67 (2020), p. 104186.

[81] Kevin A Bush et al. “Compositional engineering for efficient wide band gap perovskites with improved stability to photoinduced phase segregation”. In: *ACS Energy Letters* 3.2 (2018), pp. 428–435.

[82] Jin-Wook Lee et al. “Formamidinium and cesium hybridization for photo-and moisture-stable perovskite solar cell”. In: *Advanced Energy Materials* 5.20 (2015), p. 1501310.

[83] Amran Al-Ashouri et al. "Conformal monolayer contacts with lossless interfaces for perovskite single junction and monolithic tandem solar cells". In: *Energy & Environmental Science* 12.11 (2019), pp. 3356–3369.

[84] Viktor Moravetski et al. "29Si NMR chemical shifts of silicate species: Ab initio study of environment and structure effects". In: *Journal of the American Chemical Society* 118.51 (1996), pp. 13015–13020.

[85] DW de Quilettes et al. "Impact of microstructure on local carrier lifetime in perovskite solar cells". In: *Science* 348.6235 (2015), pp. 683–686.

[86] Qi Jiang et al. "Surface passivation of perovskite film for efficient solar cells". In: *Nature Photonics* 13.7 (2019), pp. 460–466.

[87] Peng Chen et al. "In situ growth of 2D perovskite capping layer for stable and efficient perovskite solar cells". In: *Advanced Functional Materials* 28.17 (2018), p. 1706923.

[88] Kyung Taek Cho et al. "Selective growth of layered perovskites for stable and efficient photovoltaics". In: *Energy & Environmental Science* 11.4 (2018), pp. 952–959.

[89] Saba Gharibzadeh et al. "Two birds with one stone: dual grain-boundary and interface passivation enables $>$ 22% efficient inverted methylammonium-free perovskite solar cells". In: *Energy & Environmental Science* 14.11 (2021), pp. 5875–5893.

[90] Ryan J Stoddard et al. "Enhancing defect tolerance and phase stability of high-bandgap perovskites via guanidinium alloying". In: *ACS Energy Letters* 3.6 (2018), pp. 1261–1268.

[91] Kyle Frohna et al. "Nanoscale chemical heterogeneity dominates the optoelectronic response of alloyed perovskite solar cells". In: *Nature Nanotechnology* 17.2 (2022), pp. 190–196.

[92] Martin Stolterfoht et al. "How to quantify the efficiency potential of neat perovskite films: Perovskite semiconductors with an implied efficiency exceeding 28%". In: *Advanced Materials* 32.17 (2020), p. 2000080.

[93] Robert DJ Oliver et al. “Understanding and suppressing non-radiative losses in methylammonium-free wide-bandgap perovskite solar cells”. In: *Energy & Environmental Science* 15.2 (2022), pp. 714–726.

[94] Ajay Ram Srimath Kandada et al. “Nonlinear carrier interactions in lead halide perovskites and the role of defects”. In: *Journal of the American Chemical Society* 138.41 (2016), pp. 13604–13611.

[95] David A Valverde-Chávez et al. “Nonlinear photocarrier dynamics and the role of shallow traps in mixed-halide mixed-cation hybrid perovskites”. In: *Journal of Materials Chemistry C* 9.26 (2021), pp. 8204–8212.

[96] Maximilian T Hörantner et al. “Shunt-blocking layers for semitransparent perovskite solar cells”. In: *Advanced materials interfaces* 3.10 (2016), p. 1500837.

[97] Kevin Ho et al. “Nanoscale subsurface morphologies in block copolymer thin films revealed by combined near-field infrared microscopy and mechanical mapping”. In: *ACS Applied Polymer Materials* 1.5 (2019), pp. 933–938.

[98] Adrian Camenzind et al. “Structure & strength of silica-PDMS nanocomposites”. In: *Polymer* 51.8 (2010), pp. 1796–1804.

[99] Yevgeny Rakita et al. “Mechanical properties of $APbX_3$ (A= Cs or CH_3NH_3; X= I or Br) perovskite single crystals”. In: *Mrs Communications* 5.4 (2015), pp. 623–629.

[100] Massimo Spina et al. “Mechanical signatures of degradation of the photovoltaic perovskite $CH_3NH_3PbI_3$ upon water vapor exposure”. In: *Applied Physics Letters* 110.12 (2017).

[101] Sudharm Rathore et al. “Elastic modulus tailoring in $CH_3NH_3PbI_3$ perovskite system by the introduction of two dimensionality using $(5\text{-AVA})_2PbI_4$”. In: *Solar Energy* 224 (2021), pp. 27–34.

[102] Giles E Eperon, David Moerman, and David S Ginger. “Anticorrelation between local photoluminescence and photocurrent suggests variability in contact to active layer in perovskite solar cells”. In: *ACS nano* 10.11 (2016), pp. 10258–10266.

[103] Andrew W Blakers et al. “22.8% efficient silicon solar cell”. In: *Applied Physics Letters* 55.13 (1989), pp. 1363–1365.

[104] Martin A Green. “The passivated emitter and rear cell (PERC): From conception to mass production”. In: *Solar Energy Materials and Solar Cells* 143 (2015), pp. 190–197.

[105] Konstantinos Chondroudis and David B Mitzi. “Electroluminescence from an organic-inorganic perovskite incorporating a quaterthiophene dye within lead halide perovskite layers”. In: *Chemistry of materials* 11.11 (1999), pp. 3028–3030.

[106] Zhi-Kuang Tan et al. “Bright light-emitting diodes based on organometal halide perovskite”. In: *Nature nanotechnology* 9.9 (2014), pp. 687–692.

[107] Cheng Chang et al. “$MAPbBr_3$ First-Order Distributed Feedback Laser with High Stability”. In: *Advanced Photonics Research* 4.1 (2023), p. 2200071.

[108] F Pelayo García de Arquer et al. “Solution-processed semiconductors for next-generation photodetectors”. In: *Nature Reviews Materials* 2.3 (2017), pp. 1–17.

[109] Sarah Deumel et al. “High-sensitivity high-resolution X-ray imaging with soft-sintered metal halide perovskites”. In: *Nature Electronics* 4.9 (2021), pp. 681–688.

[110] Christian Wehrenfennig et al. “High charge carrier mobilities and lifetimes in organolead trihalide perovskites”. In: *Advanced Materials (Deerfield Beach, Fla.)* 26.10 (2014), p. 1584.

[111] National Renewable Energy Laboratory. *Best research-cell efficiencies.* 2024. (accessed 2024-02-24).

[112] Tomas Leijtens et al. “Opportunities and challenges for tandem solar cells using metal halide perovskite semiconductors”. In: *Nature Energy* 3.10 (2018), pp. 828–838.

[113] Amran Al-Ashouri et al. “Monolithic perovskite/silicon tandem solar cell with $> 29\%$ efficiency by enhanced hole extraction”. In: *Science* 370.6522 (2020), pp. 1300–1309.

[114] Guang Yang et al. “Defect engineering in wide-bandgap perovskites for efficient perovskite–silicon tandem solar cells”. In: *Nature Photonics* 16.8 (2022), pp. 588–594.

[115] Erkan Aydin et al. “Enhanced optoelectronic coupling for perovskite/silicon tandem solar cells”. In: *Nature* 623.7988 (2023), pp. 732–738.

[116] Martin Stolterfoht et al. “The impact of energy alignment and interfacial recombination on the internal and external open-circuit voltage of perovskite solar cells”. In: *Energy & environmental science* 12.9 (2019), pp. 2778–2788.

[117] Dorothee Menzel et al. “Field effect passivation in perovskite solar cells by a LiF interlayer”. In: *Advanced Energy Materials* 12.30 (2022), p. 2201109.

[118] Zhou Liu et al. “Reducing perovskite/C_{60} interface losses via sequential interface engineering for efficient perovskite/silicon tandem solar cell”. In: *Advanced Materials* 36.8 (2024), p. 2308370.

[119] Hyeonwoo Kim et al. “Polymethyl methacrylate as an interlayer between the halide perovskite and copper phthalocyanine layers for stable and efficient perovskite solar cells”. In: *Advanced Functional Materials* 32.13 (2022), p. 2110473.

[120] Jinhui Tong et al. “Wide-bandgap metal halide perovskites for tandem solar cells”. In: *ACS Energy Letters* 6.1 (2020), pp. 232–248.

[121] Linze Du Hill et al. “Rationalizing energy level alignment by characterizing Lewis acid/base and ionic interactions at printable semiconductor/ionic liquid interfaces”. In: *Materials Horizons* 9.1 (2022), pp. 471–481.

[122] Qin Zhou et al. “High-performance perovskite solar cells with enhanced environmental stability based on a $(p\text{-}FC_6H_4C_2H_4NH_3)_2[PbI_4]$ capping layer”. In: *Advanced Energy Materials* 9.12 (2019), p. 1802595.

[123] Tuo Liu et al. “Tuning interfacial energetics with surface ligands to enhance perovskite solar cell performance”. In: *Cell Reports Physical Science* 4.11 (2023).

[124] Sarra Bouazizi et al. “Design and efficiency enhancement of FTO/PC$_{60}$BM/CsSn$_{0.5}$Ge$_{0.5}$I$_3$/Spiro-OMeTAD/Au perovskite solar cell utilizing SCAPS-1D Simulator”. In: *Materials Research Express* 9.9 (2022), p. 096402.

[125] Richard D Hreha et al. “Synthesis of photo-crosslinkable hole-transport polymers with tunable oxidation potentials and their use in organic light-emitting diodes”. In: *Synthesis* 2002.09 (2002), pp. 1201–1212.

[126] Qi Chen et al. “Controllable self-induced passivation of hybrid lead iodide perovskites toward high performance solar cells”. In: *Nano letters* 14.7 (2014), pp. 4158–4163.

[127] Fangyuan Jiang et al. “Synergistic Effect of PbI$_2$ Passivation and Chlorine Inclusion Yielding High Open-Circuit Voltage Exceeding 1.15 V in Both Mesoscopic and Inverted Planar CH$_3$NH$_3$PbI$_3$(Cl)-Based Perovskite Solar Cells”. In: *Advanced Functional Materials* 26.44 (2016), pp. 8119–8127.

[128] Harry W Gibson et al. “Complexation Equilibria Involving Salts in Non-Aqueous Solvents: Ion Pairing and Activity Considerations”. In: *Chemistry–A European Journal* 17.11 (2011), pp. 3192–3206.

[129] Georg Kresse and Jürgen Furthmüller. “Efficient iterative schemes for ab initio total-energy calculations using a plane-wave basis set”. In: *Physical review B* 54.16 (1996), p. 11169.

[130] John P Perdew and Yue Wang. “Accurate and simple analytic representation of the electron-gas correlation energy”. In: *Physical review B* 45.23 (1992), p. 13244.

[131] Georg Kresse and Daniel Joubert. “From ultrasoft pseudopotentials to the projector augmented-wave method”. In: *Physical review b* 59.3 (1999), p. 1758.

[132] Peter E Blöchl. “Projector augmented-wave method”. In: *Physical review B* 50.24 (1994), p. 17953.

[133] Peter E Blöchl, Ove Jepsen, and Ole Krogh Andersen. “Improved tetrahedron method for Brillouin-zone integrations”. In: *Physical Review B* 49.23 (1994), p. 16223.

[134] Jin Wen et al. “Heterojunction formed via 3D-to-2D perovskite conversion for photostable wide-bandgap perovskite solar cells”. In: *Nature Communications* 14.1 (2023), p. 7118.

[135] Saba Gharibzadeh et al. “Record open-circuit voltage wide-bandgap perovskite solar cells utilizing 2D/3D perovskite heterostructure”. In: *Advanced Energy Materials* 9.21 (2019), p. 1803699.

[136] Sateesh Prathapani, Parag Bhargava, and Sudhanshu Mallick. “Electronic band structure and carrier concentration of formamidinium–cesium mixed cation lead mixed halide hybrid perovskites”. In: *Applied Physics Letters* 112.9 (2018).